Science
AAAS

Supplementary Materials for

Water-hydroxide trapping in cobalt tungstate for proton exchange membrane water electrolysis

Ranit Ram *et al*.

Corresponding author: F. Pelayo García de Arquer, pelayo.garciadearquer@icfo.eu

Science **384**, 1373 (2024)
DOI: 10.1126/science.adk9849

The PDF file includes:

Other Supplementary Material for this manuscript includes the following:

1. Materials and synthesis

Chemicals for synthesis and electrolyte

The precursors for the synthesis of nanocrystals and electrolyte were purchased from Sigma-Aldrich (elsewhere, specified), and were used without any further purification. The chemicals used are: $Co(NO_3)_2.6H_2O$ (solid, ACS reagent, ≥ 98%), $Na_2WO_4.2H_2O$ (solid, ACS reagent, ≥ 99%), cetyltrimethylammonium bromide (CTAB, solid, BioXtra, ≥ 99%), LiOH (solid, reagent grade, 98%), NaOH (solid, reagent grade, ≥ 98%), KOH (solid, ACS reagent, ≥ 85%), $CsOH.H_2O$ (solid, ≥ 90%, ≥ 99.5% metal basis), Vulcan XC72 (conductive carbon black, NG10BEW0938, Nanografi), methanol (liquid, Pharmpur, Scharlab), ethanol (liquid, Pharmpur, Scharlab), iso-propanol (liquid, Pharmpur, Scharlab), acetone (liquid, Pharmpur, Scharlab), dimethyl sulfoxide (DMSO, liquid, ACS reagent, ≥ 99.9%), N-methyl-2-pyrrolidone (NMP, liquid, ACS reagent, ≥ 99%). Different concentration of MOH (M = Li, Na, K and Cs) were prepared by dissolving the solid bases in milli-Q water (18.2 MΩ). The electrolyte (typ. 0.5 M H_2SO_4) was prepared by diluting a higher concentration H_2SO_4 (liquid, ACS reagent, 95–98%) stock solution in milli-Q water. Commercial iridium oxide (IrO_2, Alfa Aesar, Premion, 99.99%) and cobaltic oxide (Co_3O_4, nano powder, <50 nm particle size, Sigma Aldrich, 99.5%) were used as reference anode materials.

Synthesis of $CoWO_4$ (CWO) nanocuboids

In a typical synthesis of CWO nanocuboids, 2 mmol of $Na_2WO_4.2H_2O$ and 4 mmol of CTAB were taken in a 100 mL beaker. 42 mL milli-Q water was added to it and stirred vigorously until a clear solution was formed (solution A). Meanwhile, in a 50 mL beaker, 3 mmol of $Co(NO_3)_2.6H_2O$ were taken and to it 20 mL of milli-Q water was poured. The solution was then stirred to acquire a bright red coloured Co (II)-aqueous solution (B). Next, solution B was added to the solution A and the mixture stirred vigorously to get a homogeneous solution. The resultant violet coloured solution mixture was then transferred to a 100 mL Teflon-lined stainless-steel autoclave and kept at 180˚C for 12 h. After 12 h, the autoclave was cooled naturally down to room temperature. A blue-coloured product was collected and washed several times using milli-Q water and acetone.

Delaminated CWO synthesis

The delaminated (CWO–del) compounds were obtained by immersing $CoWO_4$ (CWO) in 0.1 M aqueous KOH solution under magnetic stirring for different times (1 h to 48 h). Under continuous stirring, the blue coloured CWO turned to a brown to a black coloured product. The

post-processed product was then washed and centrifuged for five times with milli-Q water and acetone. Finally, the obtained CWO–del powder was obtained after centrifugation and annealing at 90˚C overnight.

Catalyst ink and electrode preparation

To prepare the catalyst ink, 10 mg of catalyst and 2.5 mg Vulcan carbon powder were dispersed in a mixture solution of 750 µL of milli-Q water, 150 µL of ethanol, 80 µL of iso-propanol and 20 µL of Nafion solution (5 wt.% in lower aliphatic alcohol). After sonication for 1 h, the catalyst-ink was drop-casted on pre-polished glassy carbon electrode (GCE, geometric surface area: 0.07 cm^2). The catalyst loading on GCE: ~0.5 $mg \cdot cm^{-2}$.

For long-term chronopotentiometry (CP), the catalyst ink was spray-coated on carbon paper (AvCarb®MGL370, Toray) at a loading of ~1.4 ± 0.2 $mg \cdot cm^{-2}$. The geometric surface area of the carbon paper was kept constant at 1 cm^2.

2. Materials characterization

X-ray diffraction

The phase purity and crystal structure of the as-synthesized CWO and CWO–del products were characterized by X-ray diffraction (XRD) using a Rigaku Smartlab system equipped with a radiation source of Cu-K_α (1.5418 Å). XRD spectra were acquired over the range of 10˚ to 70˚. To assess crystallography of the delaminated products, XRD of the all the delaminated compounds were performed. A regular change in the 2θ value corresponding to the $\bar{1}11$ peak of CWO and 0.1 M KOH delaminated samples was observed with time. The analysis and background correction of XRD patterns were implemented using X´Pert HighScore Plus software.

Electron microscopy

The morphology and microstructure of the materials were investigated by scanning electron microscopy (SEM) using a Zeiss Auriga Crossbeam equipped with Ga focused ion beam, and transmission electron microscopy (TEM) in JEOL JEM 2010F 200kV TEM with field emission tube with electron energy loss spectrometer (EELS). Further, the high annular angle dark field scanning transmission electron microscopy (HAADF-STEM), integrated differential phase contrast (iDPC-STEM) images and energy dispersive X-ray spectroscopy (EDS) elemental maps were acquired using a ThermoFisher Scientific Spectra 300 microscope operated at 60 kV. The STEM beam was monochromated using the TFS Optimono to avoid chromatic aberration when working at low voltage. TEM and STEM images have been processed with

DigitalMicrograph software from Gatan and Velox software from ThermoFisher Scientific. EDS data was processed with Velox. The iDPC-STEM images were overlapped with simulated crystal structures obtained from CaRIne Crystallography to identify the positions of the atoms within the crystal lattices. The crystal lattices in the micrographs of the regions of interest in this work have been enhanced by using a frequency filter in the reciprocal space. Firstly, a spot mask was applied to the diffraction nodes in the corresponding fast Fourier transformations (FFTs). Subsequently, an inverse FFT filter was applied, and the resulting image was overlapped with the original micrograph. All of these processes were executed using DigitalMicrograph. For electron microscopic studies (SEM, TEM and STEM), a very dilute solutions of the materials were prepared separately by dispersing them in ethanol. The dispersed ethanolic solution was then drop-casted on Si/SiO_2 wafer (for SEM) and on C-coated Au-grid (for TEM and STEM) and dried under vacuum for overnight.

Atomic force microscopy (AFM)

AFM measurements were performed using a Park Systems NX20 under ambient conditions in non-contact mode. For electrical measurements, the specimens were mounted on a steel disk and were electrically grounded using conductive silver paste (RS Components). AC160TS probes, with parameters: R = 7 nm, k = 26 N/m, f = 300 kHz, were employed for acquiring topographical and nanomechanical maps. Low scan rates ranging from 0.2 to 0.3 Hz were maintained. This allowed the feedback control to sustain a stable scanning regimen, reliably tracking larger topographic features. The deflection sensitivity was calibrated on a sapphire standard. To target atomic resolution, the system was left for one hour in isolation to stabilize from the thermal drift. To minimize drifting, high scan speeds (2-5 Hz) were utilized at a 90° angle.

Spectroscopic characterization

X-ray photoelectron spectroscopy (XPS): was carried out using SPECS PHOIBOS 150. For XPS experiments, the ethanolic solution of the materials were either drop-casted on Si/SiO_2 wafer or the catalyst ink were coated on the carbon paper, and then dried under vacuum overnight. The XPS peaks fitting and data analysis were carried out using CasaXPS software. The binding energy of all peaks were corrected with respect to C 1s peak (284.5 eV). The background correction of XPS spectra was performed in OriginLab software.

Inductively coupled plasma optical emission spectroscopy (ICP-OES) and mass spectroscopy (ICP-MS) were carried out to evaluate the elemental concentration in different reaction and

experiments, were performed using Perkin Elmer Optima 8300 and Agilent 7800 ICP-MS respectively.

UV-Vis spectroscopy was carried out to obtain the absorption spectra of the materials using a ParkinElmer Lambda 950 spectrophotometer. 0.1 M of the ethanolic solutions of the samples were prepared to study their optical properties. The indirect optical band gaps were calculated by Tauc plot method. The wavelengths (nm) were converted to energy (eV) and the absorption data were converted to $(2.303 \times \text{energy in eV})^{0.5}$.

Electro-paramagnetic resonance (EPR) measurements were obtained using a Bruker EMX Micro spectrometer with an X-band bridge of 9.1–9.9 GHz. The powder samples were poured into a one side-blocked capillary tubes with 76 mm (length) × 1.5 mm (outer diameter) × 0.84 mm (inner diameter) and pressed to minimize air-void.

Attenuated total reflectance–Fourier transform infrared (ATR–FTIR) spectra were obtained from the powder materials by using Agilent Cary 630 FTIR spectrometer. To minimize the amount of adsorbed water from the air, we heated the powder samples at 120˚C prior to FTIR measurements.

X-ray absorption spectroscopy (XAS), including X-ray absorption near edge structure (XANES) spectra and extended X-ray absorption fine structure (EXAFS) at Co K–edge and W L_3–edge were collected on beamline B18 at the Diamond Light Source under standard ring conditions. A Si (111) monochromator was used for energy selection. Two N_2 filled ion chambers were used to monitor the intensities of the incident and transmitted beams before (I_0) and after the sample (I_1). The calibration was performed using a cobalt foil. The data was collected in fluorescence mode using a 36 element Ge fluorescence detector. Standard Co and catalysts were measured under the same conditions in air. Data analysis was performed using the Demeter software in order to subtract the pre-edge background and normalize the spectrum after the edge jump.

Raman spectra were measured by a Renishaw Raman spectrometer equipped with 532 nm and 785 nm laser. *Ex situ* Raman spectra were acquired with a L20× objective and 532 nm laser. For the *ex situ* Raman spectra, the CWO and their derivatives were drop casted on silica substrates (Si/SiO_2).

In situ Raman spectroscopy was performed using a custom-made *in situ* cell and an immersion objective (L63×, Leica) with a 785 nm laser. The samples were prepared by spray coating on carbon paper (AvCarb®MGL370, Toray). The loading of the catalyst for all *in situ* Raman

experiments was 1 ± 0.2 mg·cm^{-2}. The potentials were applied by a single channel Autolab204 potentiostat using 0.5 M H_2SO_4 as electrolyte, and Pt wire as counter electrode. All data were acquired using 10% laser power with 30 accumulations.

To study changes in the interfacial water structure, 300 nm Ag sputtered PTFE (poly tetra fluoroethylene, loading was 1 ± 0.2 mg·cm^{-2}) was used as substrate for surface enhanced Raman spectra, using 532 nm laser with 0.5% power with 30 accumulations. The broad water peaks (O–H) from 3000 to 3700 cm^{-1}, were deconvoluted into three contributions by Origin software using a Gaussian fitting to minimise the random residuals, indicating three different types of H-bonded (n–HB·H_2O) water structures: 4–HB·H_2O (~3200 cm^{-1}), 3–HB·H_2O (~3400 cm^{-1}) and 0–HB·H_2O (~3600 cm^{-1}).

Thermogravimetric analysis coupled with mass spectroscopy (TGA-MS), was analysed by a NETZSCH TG-EGA system equipped with TGA/STA 449 F5 Jupiter thermobalance. The instrument is coupled with a Aeolos QMS 403 Quadro by NETZSCH able to measure up to 512 amu with high sensitivity. The samples are measured from 40°C to 800°C with the temperature increment of 10°C/min. All samples have been stabilized to 40°C during one hour prior to ramping. The samples are kept in Ar atmosphere (50 mL·min^{-1}) and the interface temperature of mass spectroscopy detector was kept at 200°C.

3. Solvent and alkali metal ions effect on delamination

The KOH treatment on CWO was performed for 48 h to obtain CWO–del–48 (Fig. S3). To understand the anion exchange process better, we carried out time and concentration dependent studies and collected the samples at different time to characterize them. We observed, for 12 h of reaction time, the morphology of the particles almost remained intact. However, during the course of reaction time, the shape of the nanocrystals changed (Fig. S6). After 24 h KOH treatment, the cuboid CWO transformed into flake-like morphology (Figs. S6 C, D). We assessed Co and W leaching from CWO during the course of reaction using ICP-OES technique (Fig. S35). The Raman spectra of the products obtained at different time suggests the kinetic limitation of W-leaching, as after 48 h of reaction time $I_{Co–O}/I_{W–O}$ ratio almost is almost saturated (Fig. S34 and Table S8).

Further, we investigated the role of the solvent in the delamination process. Instead of aqueous KOH solution, we post-treated the CWO powder (~30 mg) by DMSO (15 mL) and NMP (15 mL). After 48 h of stirring, DMSO made almost no effect on CWO nanocrystals. The colour of the solution remained similar compared to that of aqueous solution of CWO (inset of Fig.

S11A), as well as nanocrystal morphology (Fig. S11A). On the other hand, under NMP treatment, the clear blue coloured CWO solution became light brownish-blue, and the nanocrystals aggregated forming bigger sized particles (Fig. S11B). Both DMSO and NMP treatment did not delaminate CWO nanoparticles.

To assess the role of alkali metal cations, we performed the delamination experiments using different types of bases, MOH (M = Li, Na, K and Cs). After 18 h of delamination time, we observed a difference of the base-treated CWO under different MOH solutions (Fig. S8). We found that the extent of delamination is the highest for LiOH, and the least for CsOH (Figs. S9A and D). Aqueous NaOH and KOH treatment resulted in a similar degree of delamination (Figs. S9B and C). The role of cations on the delamination process is evident in these studies. The trend in ionic radii of four ions are: $r_{Li^+} < r_{Na^+} < r_{K^+} < r_{Cs^+}$. The delamination extent can be explained by the ionic radii of the cations; smaller the ionic radii, faster the rate of ion diffusion. The OER activity and the trend of the post-processed catalysts varying time, alkali metal ions and concentrations were also studied (Figs. S7, S10, S13). The trend in OER performance of the catalysts obtained from different concentration of KOH treatment helped us to select an optimum KOH concentration (Fig. S13).

4. DFT simulations

In this study, we used Vienna Ab initio Simulation Package (VASP) *(55)* within the DFT+U framework, with a particular emphasis on the Hubbard U correction for the surface calculations. We sourced the initial crystal structure of $CoWO_4$ from experimental findings and refined it using the PBEsol functional to guarantee stable atomic arrangements. Our simulations, based on Density Functional Theory (DFT), employed the projector augmented waves (PAW) approach with an energy cut off (ENCUT) set at 500 eV. Among the configurations, the antiferromagnetic one exhibited the lowest energy. We adjusted both the cell parameters and atomic positions to achieve the most optimized configurations. The effective on-site Coulomb (LDAUU) and exchange (LDAUJ) parameters were deduced using the equation $U_{eff} = U - J$, where U and J represent the screened Coulomb and exchange parameters, respectively. We chose U_{eff} values of 5.5 eV for Co and 6.5 eV for W atoms. For all simulations, a $2 \times 2 \times 2$ supercell was used, incorporating a 20 Å vacuum layer.

For isolated molecules like H_2O, OH^-, H_3O^+, WO_4^{2-}, and other solvated ions, we chose Gaussian09. Its strength lies in handling non-periodic, small molecular systems, ensuring precise characterization of subtle interactions without the need for periodic boundary

conditions. Utilizing the WB97XD functional, known for its empirical dispersion corrections, we ensured accurate molecular predictions. The chosen LANL2DZ basis set and accompanying pseudopotentials provided a reliable representation of molecular geometries and electronic properties. Each molecule underwent geometry optimization to achieve its energy minimum. Subsequently, single-point energy simulations were executed on these optimized structures.

Delamination and alternative anion

To gain a comprehensive insight into the CWO–OH–water system, various stoichiometries of H_2O and OH are incorporated into the delaminated structure through the ensuing reaction. These reactions transpire under varying pH conditions, leading to the formation of H_2WO_4 alongside either WO_4^{2-} or HWO_4^-, depending on the pH environment (Fig. S12). Consequently, the reaction under consideration is given by,

$$MM'_xO_y + m\,H_2O + n\,OH^- \rightarrow M\left(M'_xO_y\right)_{1-q}(H_2O)_m(OH)_n + q\,M'_xO_y^{z-} \quad \text{(eq. 1)}$$

Here, M: Mn, Co, Ni, or Cu, and M′: S, Mo, or W. The solvation energy of $M'_xO_y^{z-}$ is derived from Gaussian simulations, with the findings delineated in Table S12. Moreover, the free energy, $\Delta G_x(T)$, corresponding to a compound *x* at temperature *T*, is computed using the subsequent formula,

$$G_x(T) = E_x + ZPE_x - (S_x - C_x)T \quad \text{(eq. 2)}$$

Where E_x, the electronic energy of compound x, is typically derived from DFT simulation. ZPE_x, S_x, C_x represent the Zero Point Energy, entropy, and heat capacity respectively, obtained using PHONOPY *(56)*. The change in free energy for reaction equation 1 is captured by the equation 3, while the corresponding energetics can be found as,

$$\Delta G = \sum G_{prod} - \sum G_{react} \quad \text{(eq. 3)}$$

Dissolution and stability

To comprehend the stability of cobalt (Co) within a delaminated structure, we utilized the VASP-MGCM module (VASP-Multigrid Continuum Model) *(57)*, which has been optimized to accurately account for solvation effects that play a crucial role in interactions between surfaces and solvents. This approach is significant for precisely determining the energetic properties of surfaces within a solvent environment.

The enthalpy of dissolution, serving as a representation of the overall energy alteration linked to the dissolution process of Co from the CWO–del structure within the electrolyte, encompasses diverse factors. These factors encompass the disruption of interactions between CoO particles, the rupture of cobalt-oxygen (Co–O) and cobalt-tungsten (Co–W) bonds, and

the creation of fresh cobalt-water interactions within the solution. Considering the following reaction:

$$A^{solv} + nH_2O \rightarrow A^{solv}_{Co-diss} + Co(H_2O)_n(OH)_m{}^{solv} \quad \text{(eq. 4)}$$

Where A^{solv} signifies the solvated surface that has undergone solvation. On the other hand, $A^{solv}_{Co-diss}$ refers to the surface resulting from the dissolution and $Co(H_2O)_n(OH)_m$ species dissociates into cobalt ions and undergoes solvation by the water molecules.

Calculation of equilibrium constant for dissolution reaction

The equilibrium constant (K_{eq}) of a reaction can be obtained from the Gibbs free energy change (ΔG) of the reaction, where ΔG is determined through DFT including solvation effects (Table S1). The relationship between ΔG and K_{eq} is given by the equation $\Delta G = -RT \ln(K)$, where R is the gas constant and T is the temperature in Kelvin. For Co_3O_4, the K_{eq} is significantly greater than 1 ($K >> 1$), indicating a highly thermodynamically favorable elimination process of cobalt to the solution. This implies that the reaction for eliminating cobalt from Co_3O_4 is spontaneous. Conversely, for CWO–del–48, the equilibrium constant is much less than 1 ($K << 1$). This indicates that the elimination process is non-spontaneous, with minimal cobalt ions being eliminated from CWO–del–48.

Spontaneous reaction: (eq. 5)

$$Co_3O_4 + nH_2O \overset{R^{Co_3O_4}_{diss}}{\rightleftharpoons} Co_{3-y}O_4 + y[Co(H_2O)_n(OH)_m]_{aq}$$
$$\Delta G < 0 \implies K >> 1$$

Non-spontaneous reaction: (eq. 6)

$$Co(WO_4)_{1-x}(H_2O)_2(OH)_2 + nH_2O \overset{R^{CWO-del}_{diss}}{\rightleftharpoons} Co_{1-y}(WO_4)_{1-x}(H_2O)_2(OH)_2 + y[Co(H_2O)_n(OH)_m]_{aq}$$
$$\Delta G > 0 \implies K << 1$$

Equations (5) and (6) above illustrate the dissolution process of cobalt from two materials: Co_3O_4 and CWO–del–48, respectively; with arrows indicating the direction and spontaneity of the reactions.

Table S1. Comparative schematic of cobalt solvation from Co_3O_4 and CWO–del–48: thermodynamics and equilibrium constants.

Equilibrium Reactions	ΔG (eV/atom)	K_{eq} at T=300 K
eq. 5 (Co^{3+})	– 0.56	2.57×10^{9}
eq. 5 (Co^{2+})	– 0.23	7.32×10^{3}
eq. 6 (Co^{3+})	+ 2.19	1.07×10^{-37}
eq. 6 (Co^{2+})	+ 1.44	2.98×10^{-24}

The OER Mechanism

The free energies of the OER intermediates are estimated using the equation 6. Further for estimating the free energetics of the Proton coupled electron transfer steps we used the Computational Hydrogen Electrode (CHE) approximation *(58)*.

The conventional OER mechanism in acidic environments (AEM) involves four coordinated proton–electron transfers on Co surface sites, producing three intermediates: OH*, O*, and OOH*. On the other hand, the Oxide Path Mechanism (OPM) *(12)* involves only O* and HO* as intermediates, promoting direct O–O radical coupling. In the CWO-del surfaces, water and OH^- clusters drive complex reaction mechanisms, denoted confined, cAEM and cOPM. The stoichiometry of these clusters dictates the reaction pathways, resulting in a variety of mechanisms that yield different outcomes. As OH^- adsorbs on the surface, it creates a vacancy that attracts H_2O molecules for compensation, preserving the structural and stoichiometric integrity of the material. This cycle involves diffusion, adsorption, and compensation, balancing material stability and reactivity (as described in Fig. 3F and Table S14).

We used the (010) surface orientation of CWO due to its stability. We then computed the energetics of these intermediates for both CWO and CWO–del structure. The overall OER equation and the reaction pathway in each respective medium are listed in Table S14.

Surface Pourbaix Diagrams

Surface Pourbaix diagrams illustrate the surface states based on variations of pH and potential from a thermodynamic perspective. When observing CWO–del surface with its adsorption site (∗) and a pre-adsorbed molecule (O_xH_y), the adsorption process can be captured by the following equation:

$$M - O_xH_y + (2x - y)(e^- + H^+) \leftrightarrow M^* + xH_2O \quad \text{(eq. 7)}$$

Where, *x* and *y* are the number of oxygen and hydrogen atoms in the adsorbate, respectively. The free energy change was deduced using:

$$\Delta G = G_{M^*} + xH_2O - G_{M-O_xH_y^*} - (2x - y)\left(0.5G_{H_2} - U_{SHE} - 2.303k_\beta TpH\right) \quad \text{(eq. 8)}$$

Here, U_{SHE} signifies the potential in relation to the Standard Hydrogen Electrode (SHE). For each constituent of this system, the free energy, $\Delta G_x(T)$, for a compound x at temperature, T is determined using the following equation:

$$Gi\,(T) = E_i + ZPE_i - TS_i \quad \text{(eq. 9)}$$

Where E_i, the electronic energy of compound M* or M-O_xH_y*, which is derived from DFT simulation. ZPE_i, S_i, C_i represent the corresponding Zero Point Energy, entropy, and heat capacity respectively, obtained using PHONOPY *(54)*. While the theoretical overpotential is then readily defined as:

$$\eta = \max[\Delta G_1, \Delta G_2, \Delta G_3, \Delta G_4]/e - 1.23\ [V] \quad \text{(eq. 10)}$$

5. Gas chromatography and % FE calculation

The generated O_2 was detected by manual injection to Perkin Elmer gas chromatography equipped with thermal conductivity detector (TCD) and flame ionization detector (FID). Argon was used as carrier gas maintaining a constant pressure of 12 psi and the oven temperature kept at 180°C throughout the measurements. A metal Packed GC Column (General Configuration), phase none, matrix 40/60 Carboxen-1000 support, L × O.D. × I.D. 2.0 ft (0.61 m) × 1/8 in. × 2.1 mm was used for the O_2 detection.

The Faradic efficiency (FE) of evolved O_2 was quantified for CWO–del–48 using gas chromatography during chronoamperometry. A two-compartment (30 mL volume) gas tight H-cell separated by a pre-activated Nafion 117 membrane was used with a constant input argon flow of 50 sccm, adjusted using a Sierra mass-flow-controller and after every injection output gas flow was measured by a manual flowmeter and used for % FE calculation. For O_2 % FE, a chronoamperometry experiment was performed at 10 mA·cm^{-2} current density for 160 min and ten samples were manually taken and injected with a regular time interval (Fig. S55). To minimise the errors due to manual injection, O_2 due to background was subtracted by only injecting argon from the H-cell headspace without electrolysis. The O_2 is calibrated by known amount of O_2 gas (in ppm, Fig. S56) diluted in an argon matrix (99.9999%). Gas-chromatographs for electrochemical experiments and calibration are shown in Figs. S57-S59 for completeness. O_2 FE quantification was also performed at 20 and 50 mA·cm^{-2} current

densities (Fig. S60). The FE of the formed O_2 during CP test at 10 mA·cm^{-2} was determined by the following equation (*10, 11*),

$$FE_{O_2} = \frac{Q}{Q_0} \times 100\ \%\quad \text{(eq. 11)}$$

where, Q is the charge of produced O_2 during CP test and Q_0 represents the total charge used for the OER electrocatalysis. The Q and Q_0 were calculated by following equation (*23*),

$$FE_{O_2} = \frac{P \times V(\%) \times n \times F \times V}{R \times T \times I_0} \times 100\ \%\quad \text{(eq. 12)}$$

V_o (%) represents the volumetric concentration of the gas, which is determined by the peak area of the oxygen peak and the calibration curve and V is volume of the sample loop. T represents the temperature of the test (T = 298 K), P is the pressure during the test (P = 1 atm), R represents the ideal gas constant (R = 0.08206 atm·L·mol^{-1}·K^{-1}), N is the Avogadro´s constant (N = 6.022 × 10^{23} mol^{-1}), F is Faraday constant (F = 96485 C·mol^{-1}), I_0 is the average current during the gas injection and n is the total number of electrons associated in the OER process (n = 4).

6. Electrochemical studies

The electrochemical performance of all the catalysts were studied and analysed in AutolabM204 equipped with electrochemical impedance spectroscopy (EIS) and current booster; and with a Biologic SP50 electrochemical workstation.

For all OER studies, we typ. used 0.5 M H_2SO_4 as the electrolyte. Graphite rod (CorrTest Instruments, CS915, 4 mm of diameter and 15 cm of length) and saturated Hg/Hg_2SO_4 (MSE) electrodes (E^0_{MSE} = 0.65 V *vs.* RHE) were used as counter and reference electrodes, respectively and the catalyst on glassy carbon electrode (GCE) and/or carbon paper used as the working electrode. Linear sweep voltammetry (LSV) studies were carried out at 5 mV·s^{-1} scan rate. The chronopotentiometry (CP) tests were performed in H-cell (CS932S, sealed H-cell, CorrTest Instruments) at 10 mA·cm^{-2} current density, using Nafion 117 as a proton exchange membrane. The volume of the H-cell is 50 mL for both cathode and anode chambers. The volume of the electrolyte ~40 mL. After conditioning the electrodes at 10 mA·cm^{-2} for 1 h, LSVs were recorded from 0.65 to 1.8 V *vs.* RHE at 5 mV·s^{-1} of scan rate. All electrochemical studies were performed under 600 rpm. of stirring in 0.5 M H_2SO_4 electrolyte at room temperature unless otherwise specified.

The applied electrode potentials were converted into RHE scale by using following equation *(35)*,

$$E_{RHE} = E_{Hg/Hg_2SO_4} + E^0{}_{MSE} + (0.0591 \times pH) \quad \text{(eq. 13)}$$

$E_{Hg_2SO_4}$ is the electrode potential, $E^0{}_{MSE}$ = 0.65 V *vs.* RHE, the pH of 0.5 M H_2SO_4 = 0.2 (Table S3) thus the electrode potential can be converted as,

$$E_{RHE} = E_{Hg/Hg_2SO_4} + 0.662\ V \quad \text{(eq. 14)}$$

To ensure accurate electrochemical measurements, we initially calibrated the pH meter with five commercially available pH buffer solutions (pH 1.68 to 12.8). We then used a Hg/Hg_2SO_4 reference electrode calibrated with a commercial RHE (Gaskatel hydroflex hydrogen reference electrode, more details in Table S2). We compared the measured potential gap alongside the potential gaps calculated using both measured and theoretical pH values (Table S2). These results reveal a potential variation within 1–8 mV, indicating a high level of accuracy and reliability in the calibration of electrode potential.

Table S2. pH calibration by commercial buffers and the potential gaps between Hg/Hg_2SO_4 and commercial RHE, calculated by measured or theoretical pH values.

pH buffer	Measured pH	Measured potential gap (mV)	Calculated potential gap using measured pH (mV)	Calculated potential gap with theoretical pH (mV)
7.00	6.99	1060	1063	1064
4.01	4.02	886	888	887
1.68	1.62	753	746	749

Table S3. Measured pH, R_s and corresponding potential difference of different concentration of H_2SO_4 solutions.

Conc. of H_2SO_4 (M)	Measured pH	Theoretically calculated pH	R_s (Ω)	Measured potential gap (mV)	Calculated potential gap using measured pH (mV)	Calculated potential gap using theoretical pH (mV)
0.5	0.2	0	6.1	660	662	650
0.25	0.70	0.60	8.5	688	691	685
0.1	1.07	1.00	13.1	711	713	709
0.075	1.19	1.12	25.3	715	716	716
0.05	1.24	1.30	46.2	718	721	726

Electrochemical impedance spectroscopy (EIS) was performed in a three-electrode set-up without any magnetic stirring. EIS spectra were recorded at 1.462 V *vs.* RHE for each electrode, in a frequency range of 100 kHz to 0.01 Hz using a sinusoidal wave of amplitude 10 mV. The Nyquist plot was fitted with an equivalent circuit to obtain solution (R_s) and charge transfer resistances (R_{CT}).

CCM fabrication

Catalyst coated membrane (CCM) samples were prepared using a decal method with Nafion 117 as the polymer electrolyte. CWO–del–48 was utilized as the anode catalyst, while the cathode catalyst consisted of 60 wt.% Pt on Vulcan carbon XC 72R obtained from Fuel Cell Store. As a benchmark, iridium oxide (Alfa Aesar, Premion, 99.99%) was employed for the anode catalyst comparison.

To fabricate the CCM samples, the catalyst powder and ionomer solution (20 wt.% Nafion for the anode and 25 wt.% Nafion for the cathode) were mixed in a solution of water and ethanol to create the ink. The ink was then subjected to ultrasonic homogenization for 30 minutes and later sprayed onto inert decal substrates using a hand-spray gun.

The membrane was positioned between one anode and one cathode decal, and the entire assembly was hot-pressed at a temperature of 130˚C for three minutes to ensure proper adhesion and integration of the catalyst layers. The final loading of catalyst layers was 0.8 $mg \cdot cm^{-2}$ for Pt/C at the cathode, 1.0 $mg \cdot cm^{-2}$ for IrO_2 and 4.0 $mg \cdot cm^{-2}$ for CWO–del–48 at the anode, respectively.

Cell assembly and PEMWE measurements

The MEAs were placed between a porous transport layer (PTL) made of platinum-plated titanium received from Mainz Hydrogen Energy and a gas diffusion layer (GDL, AvCarb®MGL370, Toray). The PEMWE cell features a platinum-coated titanium as the anode current collector and a graphite plate as the cathode counterpart. Both sides of the cell incorporate serpentine flow channels, each covering an area of 4 cm^2. The cells were compressed using a torque of 7 N·m on each of the four bolts.

The pre-heated milli-Q water at 80˚C was continuously pumped into the anode side of the fuel cell at a flow rate of 25 $mL \cdot min^{-1}$. The membrane electrode assemblies (MEAs) were conditioned by maintaining the cell at a constant potential of 1.7 V for 12 h, with the operating temperature being controlled at 80°C using two heating rods. Following the conditioning process, a polarization test was conducted using linear sweep voltammetry at a scan rate of 5

$mV \cdot s^{-1}$. For the durability test of the catalyst, the current density was set at specific values of either 0.2 or 1.0 $A \cdot cm^{-2}$, while the cell voltage was continuously monitored over time.

pH-dependent studies

The electrochemical pH dependency of the CWO and CWO–del–48 catalyst in OER was investigated in a single-compartment cell using the catalyst ink and the three-electrode setup aforementioned. The LSVs were performed at 0.25 M, 0.1 M, 0.075 M and 0.05 M of H_2SO_4 electrolytes, prepared from a 0.5 M of stock H_2SO_4 solution. The corresponding pH of each solution was measured using a Fisher Scientific accumet® AE150 pH-meter. The recorded electrode potentials were converted into the RHE-scale by using equation 13. EIS tests were carried out to determine the solution resistance (R_s) at different pH solution. The *iR*-correction of the potential (E_{RHE}), only made for these studies, was made using the following expression, the corrected potential *(35)*,

$$E_{corr} = E_{RHE} - iR \quad \text{(eq. 15)}$$

Methanol oxidation reaction (MOR)

We performed MOR to trace the OER pathways of the catalysts. The higher reaction order in MOR of a catalyst explains the formation of electrophile during the course of reaction, which attack methanol *(35)*. In acidic OER reaction, except the first water dissociation step, rest of the steps consist of electrophiles. Thus, MOR could be a crucial electrochemical reaction to investigate whether water dissociation or the formation of electrophile is the rate-determining step (RDS) in acidic OER for a particular catalyst. We prepared 0.1, 0.5 and 1 M MeOH solutions using 0.5 M H_2SO_4 as the matrix. Polarisation curves for MOR were recorded using the afore-mentioned three-electrode set up. The electrode potential in MSE scale were then converted to RHE scale using equation (14) as the pH of 0.5 M H_2SO_4 = 0.2.

Catalyst life-time estimation

The stability number (S_n), life-time of the catalyst and the activity-stability factor were calculated. The stability number of the catalyst can be expressed as the ratio of total mole number of O_2 evolved (n_{O_2}) in OER reaction to the mole number of Co leached during OER (n_{Co}) *(25)*,

$$S_n = \frac{n_{O_2}}{n_{Co}} \quad \text{(eq. 16)}$$

n_{Co} is obtained from ICP-MS experiments. n_{O_2} is calculated from total charge (Q_t) of OER chronopotentiometry test time at 10 $mA \cdot cm^{-2}$ of current density.

$$Q_t = J \times t = n \times F \times n_{O_2} \quad \text{(eq. 17)}$$

J is the current density in $A \cdot cm^{-2}$ and t is the CP test time in s, n is the number of electrons involved in OER process = 4, F is Faraday constant = 96,485 $C \cdot mol^{-1}$; The measured FE in our study is 96.6 ± 5.2% at 10 $mA \cdot cm^{-2}$ current density. Thus, we consider the measured FE and the corresponding percentage of error (%) to calculate our S-number and the associated error for each measurement.

Estimation of S-number in PEMWE operation: To assess the lifetime of the catalyst in PEMWE operating condition at 1 $A \cdot cm^{-2}$, we collected an aliquot after 608 h of stability test at 1 $A \cdot cm^2$ (Fig. 4F). Using ICP-OES, we determined a concentration of leached Co ions of 8.89 ppm (volume of the reservoir is 800 mL). The calculated S-number is ~4547 $\pm$ 236 (using equations 16 and 17, see section 6) in PEMWE (80˚C) which is ~31% of the S-number achieved at 10 $mA \cdot cm^{-2}$ in H-cell (Fig. S72). This indicates that high current density and temperature operation has a crucial impact on the catalyst's stability by thermal degradation and accelerated corrosion.

Dunk experiment: To assess the chemical stability of CWO, CWO–del–48, and commercial Co_3O_4, we immersed 20 mg of each material into 10 mL of 0.5 M H_2SO_4 solution. After 10, 25 and, 50 h of immersion, we collected 1 mL of the supernatant solution to check the Co ions leaching by ICP-OES.

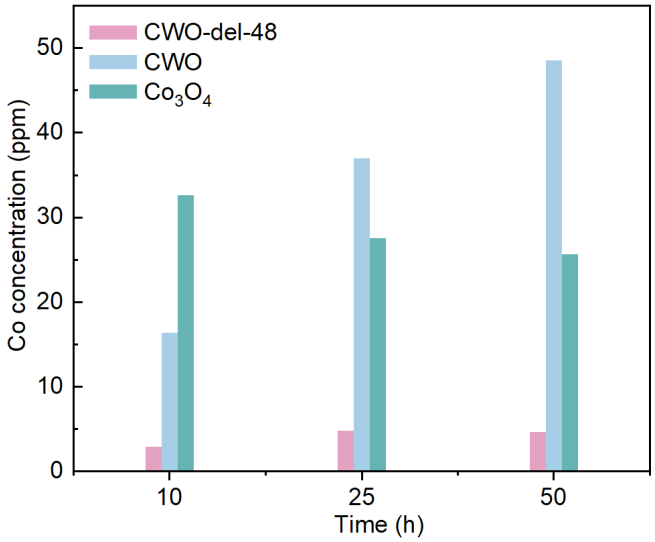

Fig. S1. Chemical stability test by dunk experiment. Elemental leaching was assessed by ICP-OES after immersion of 20 mg of CWO–del–48, CWO, and commercial Co_3O_4 powder, separately, in 0.5 M H_2SO_4 after 10, 25 and 50 h.

The leached Co ions concentration from commercial Co_3O_4 was 32.64, 27.51, and 25.65 ppm after 10, 25, and 50 h of immersion, respectively. Similarly, for CWO, the concentrations were 16.35, 36.98, and 48.57 ppm after 10, 25 and 50 h, respectively. In contrast, CWO–del–48 exhibited significantly lower leached Co ions concentration of 2.85, 4.82 and 4.58 ppm after 10, 25 and 50 h, respectively. The total Co ions leaching from 20 mg of CWO–del–48 after 50 h of immersion in 0.5 M H_2SO_4 is ~0.122 mg (0.142 wt.%), which is ~8.2 and ~7.2 times lower than that from CWO and commercial Co_3O_4, respectively. The weight loss of Co after dunk experiments is 0.142 wt.% which is 10 times lower than that of at OCP condition (Fig. S68).

These results also showcase that, in all cases, a large fraction of Co weight loss might happen before electrochemical operation at OCP, potentially affecting local dissolution dynamics.

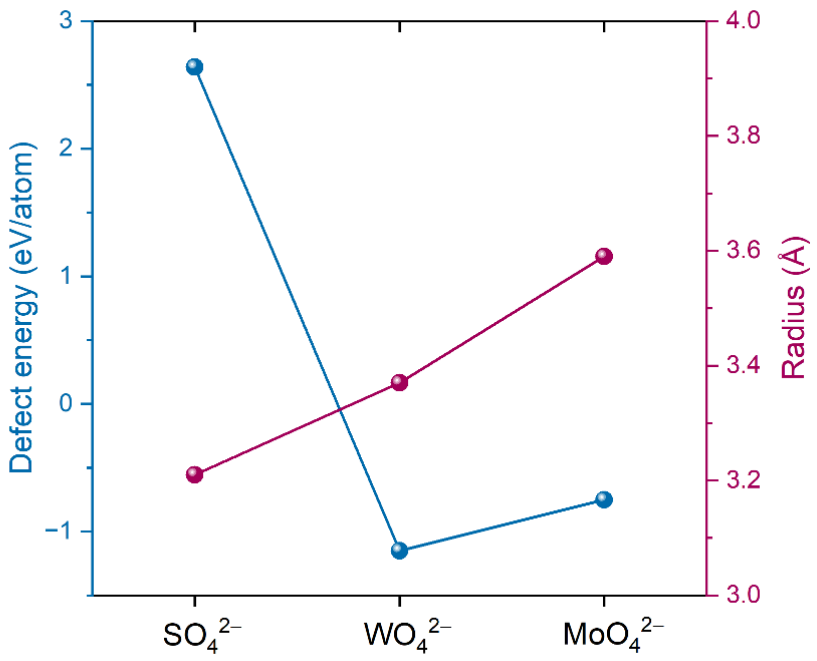

Fig. S2. Defect energy calculations. Energy of $M'O_4^{2-}$ defect formation (M' = S, W and Mo) in the $CoM'O_4$ lattice as function of ionic radii of $M'O_4^{2-}$ ions.

Table S4. Co–Co Bond Distances (Å) and implications for delamination. The table presents a comparison of Co–Co distances across different systems. Consistent distances of 4.7 to 4.9 Å in the $CoWO_4$ system indicate a stable lattice structure and potential for uniform delamination. In contrast, systems with variations up to 1 Å in Co–Co bond lengths may exhibit anisotropic properties, leading to varied delamination patterns, localized stress, or differential interactions.

	$Co–Co_1$	$Co–Co_2$	Co–O	Co–X
$CoWO_4$	4.77	4.90	2.01	3.37
$CoSO_4$	3.20	5.17	2.15	3.21
$CoMoO_4$	3.01	4.95	2.05	3.59

To clarify the role of radius of the oxyacid ion, the crystal information was summarized in Table S5. The M'–O distance remains relatively constant; however, due to variations in cation radius, the radius for the unit $M'O_4^{2-}$ differs in each instance. Specifically, the radius for WO_4^{2-} measures 2.49 Å, whereas for MoO_4^{2-}, it extends to 2.69 Å (refer to Fig. S37).

Table S5. The M'–O distance in WO_4 and MoO_4 groups affected by the cation radius

	Space group	a (Å)	b (Å)	c (Å)	r (Co^{2+}) (Å)	r ($M'O_4^{2-}$) (Å)
$CoWO_4$	P2/c (13)	4.59	4.68	4.98	0.75	2.49
$CoMoO_4$	C2/m (12)	6.84	6.93	7.65	0.75	2.69

Table S6. Delamination energy (in eV) of WO_4^{2-} in MWO_4 where M is Cu, Ni or Mn at alkaline pH using GGA and HSE functional methods.

	$CuWO_4$		$NiWO_4$		$MnWO_4$	
	GGA	HSE	GGA	HSE	GGA	HSE
E_{del} (eV)	1.33	1.25	0.81	1.27	2.71	1.25

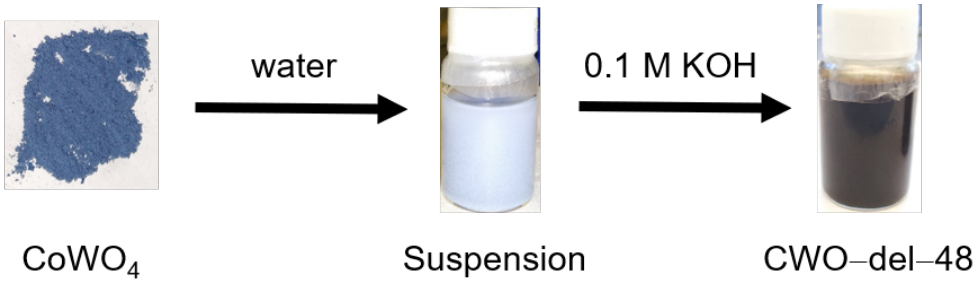

Fig. S3. KOH treatment on CWO. Under 0.1 M KOH treatment, after 48 h, the blue coloured CWO was converted to a dark black coloured solution.

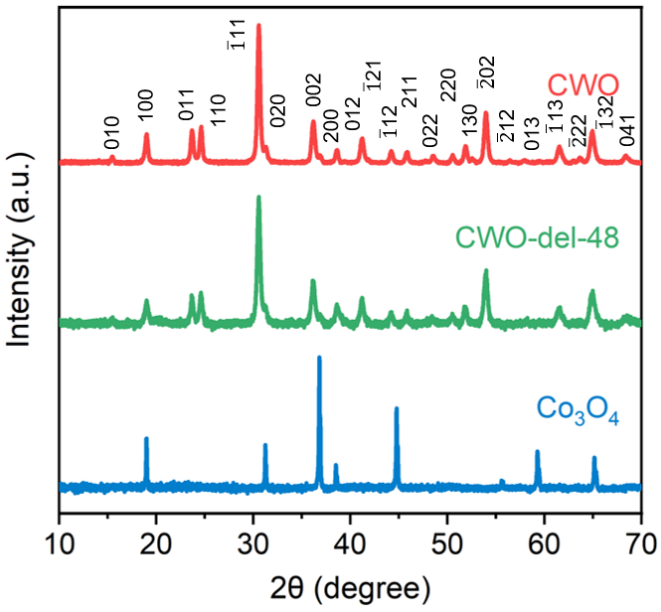

Fig. S4. X-ray diffraction. A comparison of XRD pattern of as-synthesized CWO, CWO–del–48 and commercial Co_3O_4. The sharp peaks in XRD indicate a highly crystalline nature of the materials. The XRD pattern of CWO matched with the monoclinic $CoWO_4$ phase (JCPDS card number 00-015-0867), having P2/a space group with lattice parameters, a = 4.9478 Å, b = 5.6827 Å, and c = 4.6694 Å. No extra peak corresponds to starting materials, WO_3, Co oxides or any kind impurity phase are noticeable in the powder XRD pattern of the material. The bulk phase of CWO–del–48 remain intact with compared to CWO.

Table S7. The obtained 2θ values of $\bar{1}11$ plane of the materials from XRD.

Materials	**2θ-value of $\bar{1}11$ plane**
CWO	30.546°
CWO–del–6	30.548°
CWO–del–12	30.548°
CWO–del–24	30.551°
CWO–del–48	30.563°

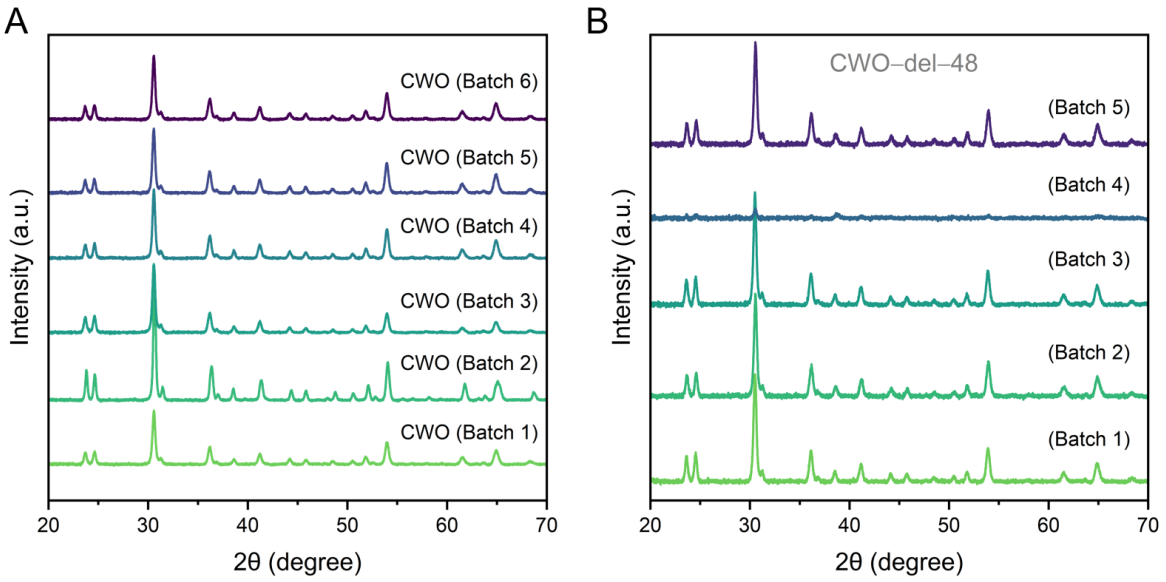

Fig. S5. Repeatability of CWO and CWO-del-48. XRD patterns of batches of (A) CWO samples and (B) CWO–del–48 samples synthesized at similar conditions. To assess CWO–del catalyst repeatability, we looked into the (1) synthesis and (2) delamination steps, characterizing the crystal structure of the materials. Six distinct batches of CWO catalysts were individually synthesized and subsequently subjected to the delamination process.

The diffraction peak positions of the six CWO batches remain consistent (Fig. S5A), indicating reproducible crystal structures. This observation suggests a high level of repeatability in the synthesis process of CWO. In the XRD patterns of delaminated samples (Fig. S5B), one batch exhibited a reduction in crystallinity, suggesting this step as the most sensitive one during the catalyst preparation.

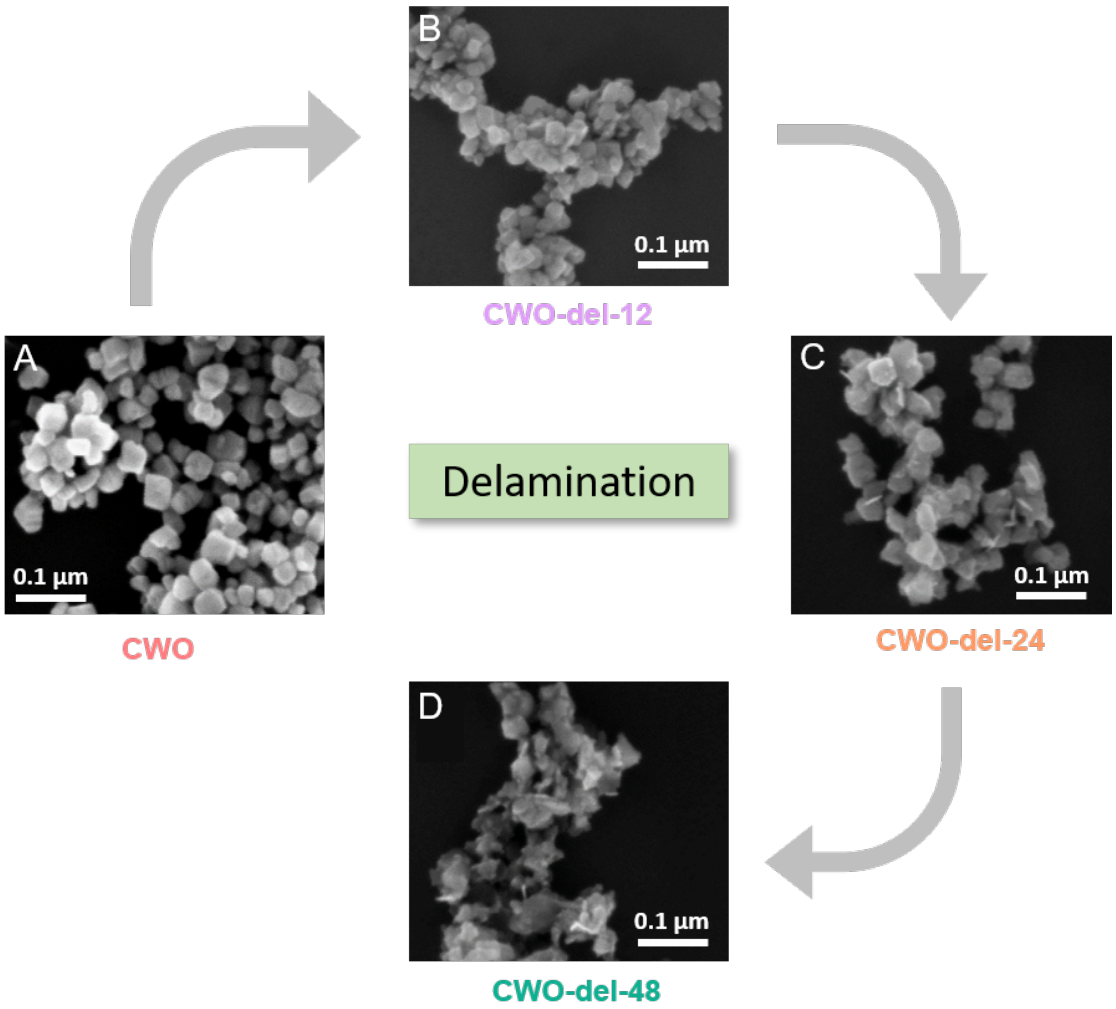

Fig. S6. Clockwise delamination. The change in morphology of CWO under 0.1 M KOH treatment was analysed by SEM. (A) as-synthesized CWO, (B), (C) and (D) are 12 h, 24 h and 48 h 0.1 M KOH treated products, respectively. The clockwise SEM study revealed the change in morphology of the nanocrystals and the extent of delamination with varying time. The SEM images reveal uniformity in the morphologies of the respective materials.

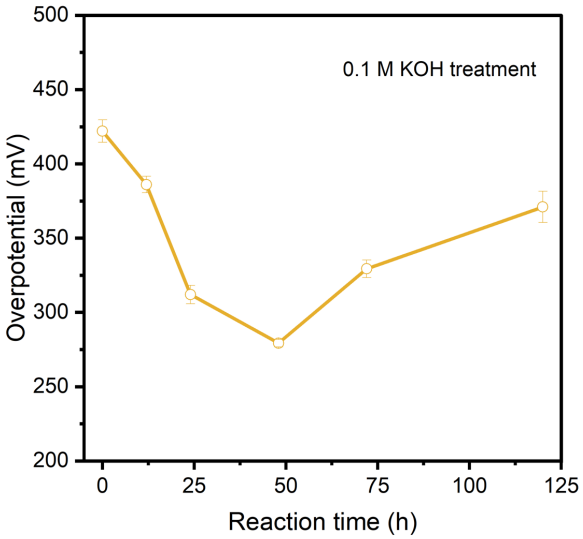

Fig. S7. OER activity *vs.* delamination time. The overpotential of the catalysts was obtained for different 0.1 M KOH delamination times. The catalysts obtained after 48 h of delamination show the highest OER activity. Beyond 48 h treatment, catalysts exhibited lower OER performance. The error bars represent the standard deviation of the overpotentials obtained in three independent LSV measurements.

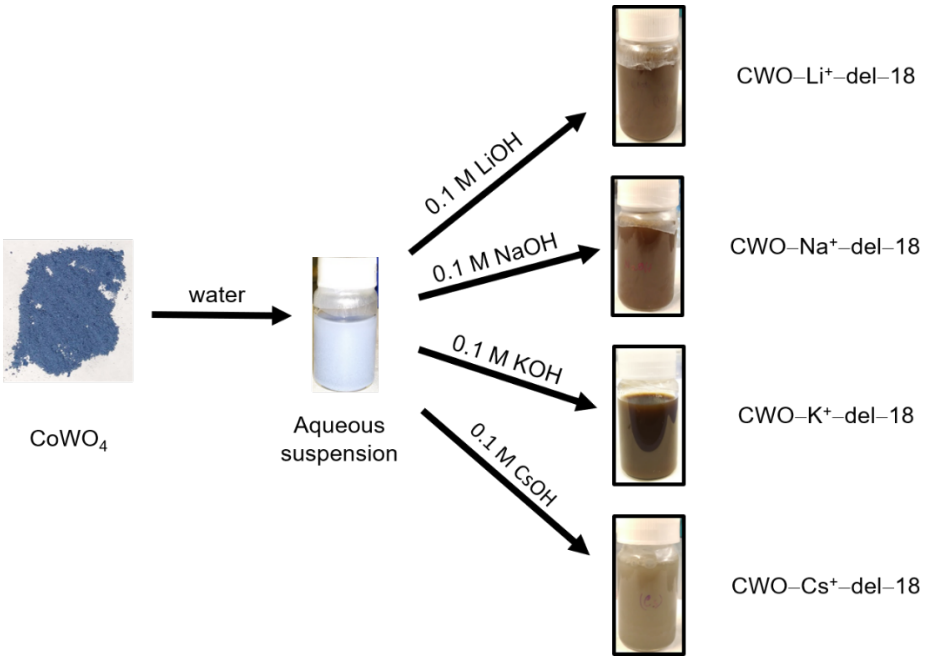

Fig. S8. Effect of different bases on CWO delamination. 0.1 M of different bases was used to study the role of metal cation on the delamination process. After 18 h of delamination, a significant extent of change in the colour of the post-processed solutions is observed.

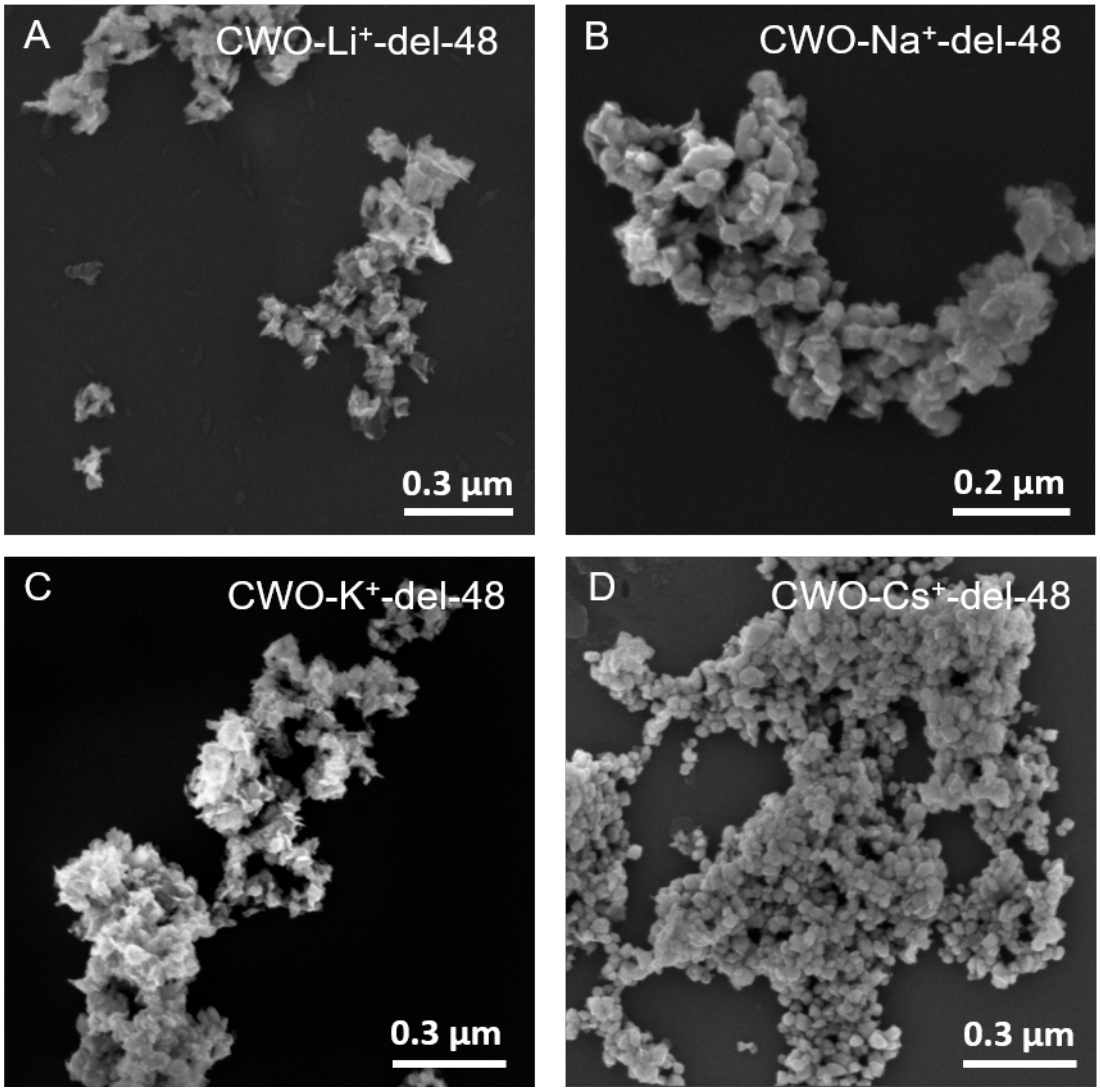

Fig. S9. Cation effect on delamination. SEM micrographs of 0.1 M base-treated CWO for 48 h in (A) LiOH, (B) NaOH, (C) KOH and (D) CsOH aqueous solution. LiOH displayed the highest extent of delamination, whereas CsOH showed the least. NaOH and KOH demonstrated a similar extent of delamination of CWO nanocuboids.

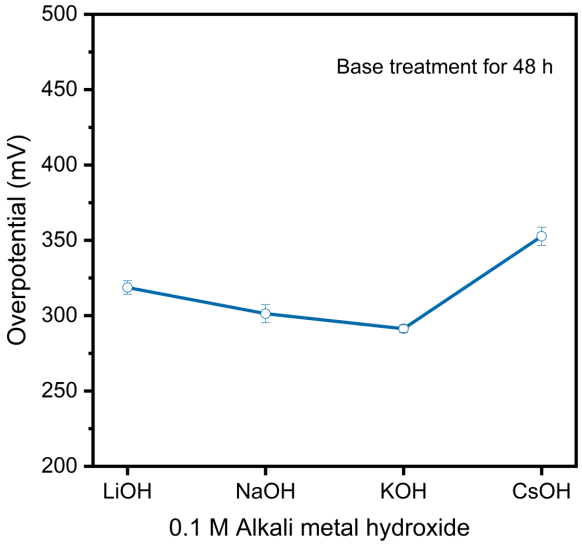

Fig. S10. Impact of delamination cations on OER overpotential. CWO-del-48 catalysts produced using 0.1 M MOH (M = Li, Na, K and Cs) were studied. In all cases, the base treatment results in lower overpotential compared to CWO. CsOH shows the lowest effect in increasing the OER activity. LiOH treatment lowers the overpotential to 311 mV. KOH treatment results the highest OER activity. The effect NaOH treatment on OER was slightly lower than that of KOH.

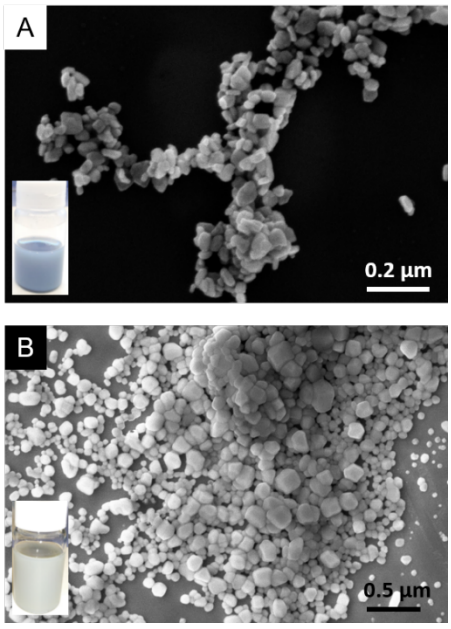

Fig. S11. Non-aqueous solvent effect. SEM assessing the change in morphology of CWO after 48 h of stirring using two non-aqueous solvents **(A)** DMSO and **(B)** NMP. The insets in **(A)** and **(B)** display the digital images of DMSO and NMP treated CWO solutions respectively.

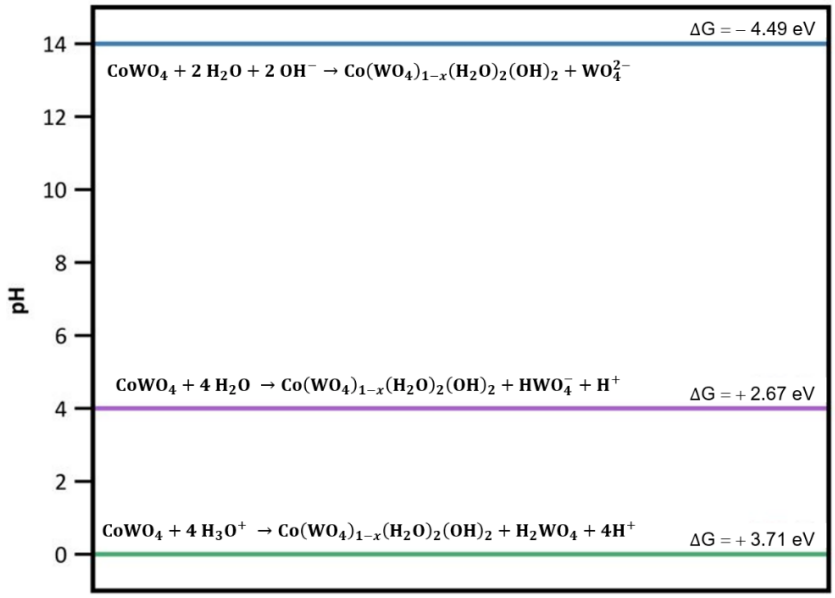

Fig. S12. Free energy change. The effect of pH on the solvation environment of $CoWO_4$ and the subsequent reaction pathways have been demonstrated. The calculations were conducted using the VASP–MGCM module within the Vienna Ab initio Simulation Package (VASP) software *(57)*. $CoWO_4$ in alkaline medium is thermodynamically very unstable and spontaneously converted to $Co(WO_4)_{1-x}(H_2O)_2(OH)_2$ (here pH is 14). However, the conversion $CoWO_4$ to $Co(WO_4)_{1-x}(H_2O)_2(OH)_2$ is not thermodynamically favourable at pH 0, indicating its stability in harsh acidic medium.

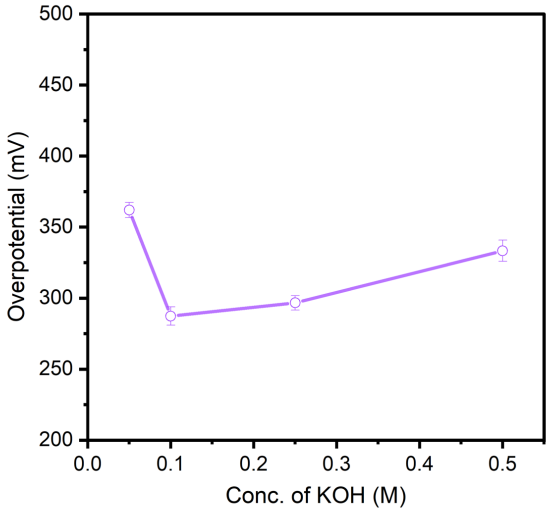

Fig. S13. OER activity *vs.* conc. of KOH. The OER performance of the catalysts obtained by different conc. (0.05 M, 0.1 M, 0.25 M and 0.5 M) of KOH treatment were studied. The base treatments were performed for 48 h in all cases.

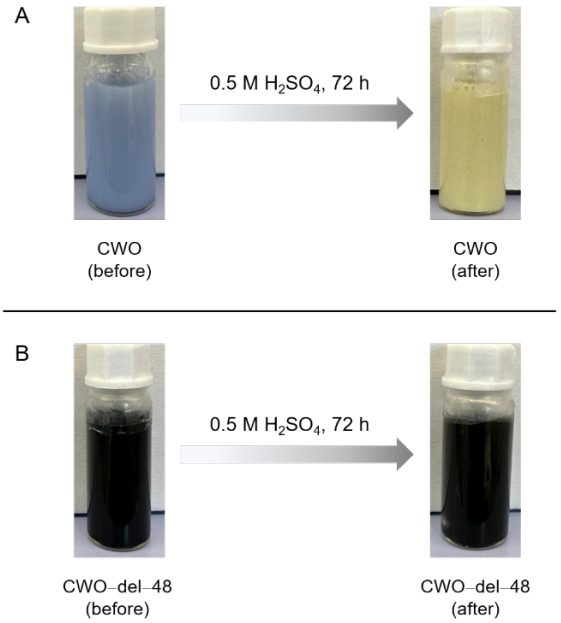

Fig. S14. Durability test in acid. CWO (A) and CWO–del–48 (B) powders were immersed in 0.5 M H_2SO_4 to check the acid-stability of the catalysts. After 72 h, blue coloured CWO solution completely transformed to yellow-coloured solution, indicating the instability of CWO in H_2SO_4. On the other hand, CWO–del–48 shows no visual change after 72 h immersion into H_2SO_4 solution, suggesting a high acid-tolerance.

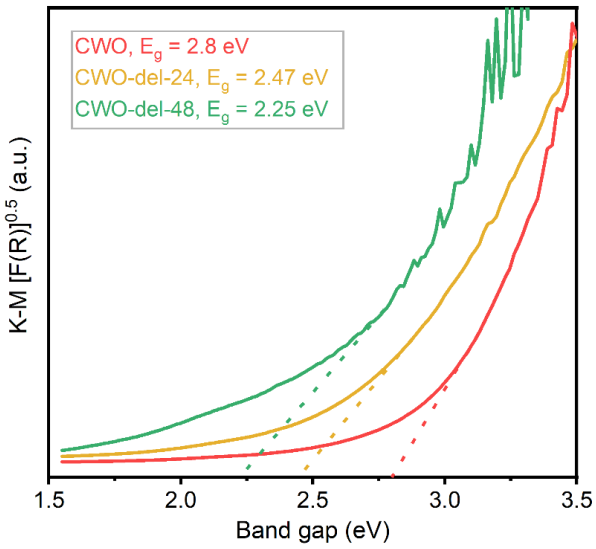

Fig. S15. Optical bandgap. The optical bandgap of as-synthesized CWO is 2.8 eV. After 24 and 48 h of 0.1 M KOH treatment, the bandgap of CWO–del–24 and CWO–del–48 is reduced to 2.47 eV and 2.25 eV, respectively.

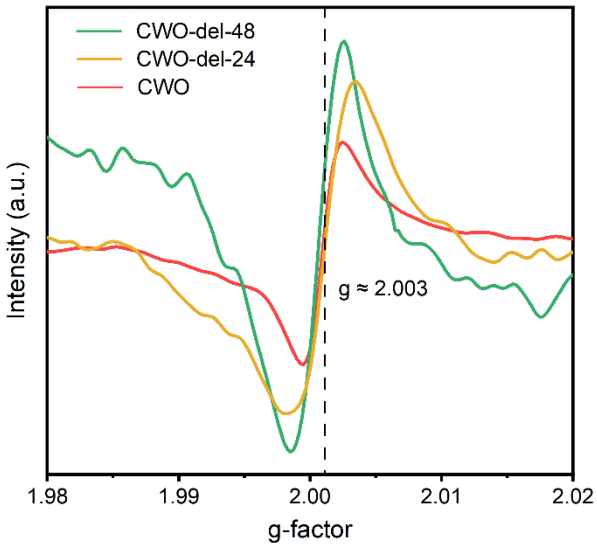

Fig. S16. Electron paramagnetic resonance (EPR) study. The EPR spectra of the materials display an increase in peak intensity at $g \sim 2.003$, from CWO to the delaminated compounds. This suggests the presence of a higher free electron charge density in the delaminated compounds compared to pristine. This trend is compatible with an increase in atomic-vacancies in delaminated compounds as a result of WO_4^{2-} leaching.

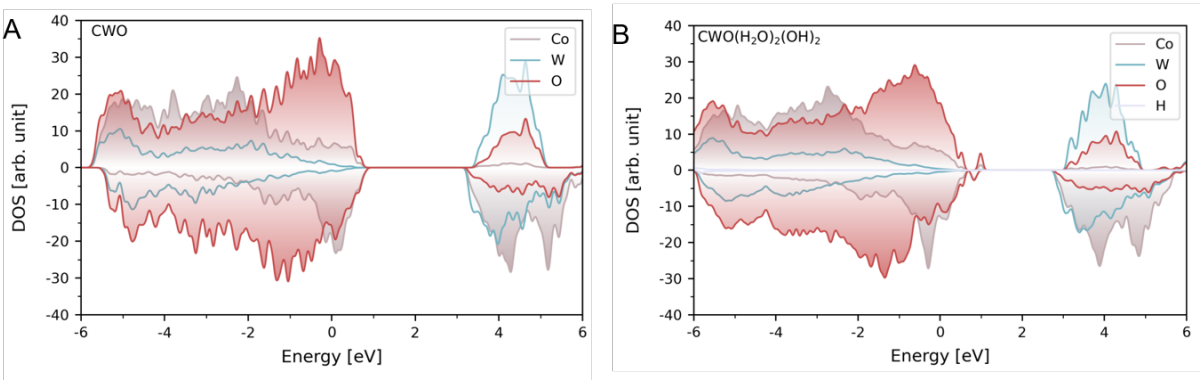

Fig. S17. Study of electronic properties. DFT-calculated density of states of CWO and CWO–del–48. $Co(WO_4)_{1-x}(H_2O)_2(OH)_2$ structure was taken to calculate the projected density of states (PDOS) of CWO–del–48. The broader the peak in the PDOS plot, the higher the number of available quantum states at that energy level. This corresponds to a higher entropy since there are more possible configurations of the particles at that energy level. The calculated bandgap of CWO is 2.77 eV, which is close to the experimental value. Calculations reveal that H_2O and OH^- trapping in CWO, in place of WO_4^{2-}, produces an activated lattice-O energy state which reduces the bandgap to 2.1 eV.

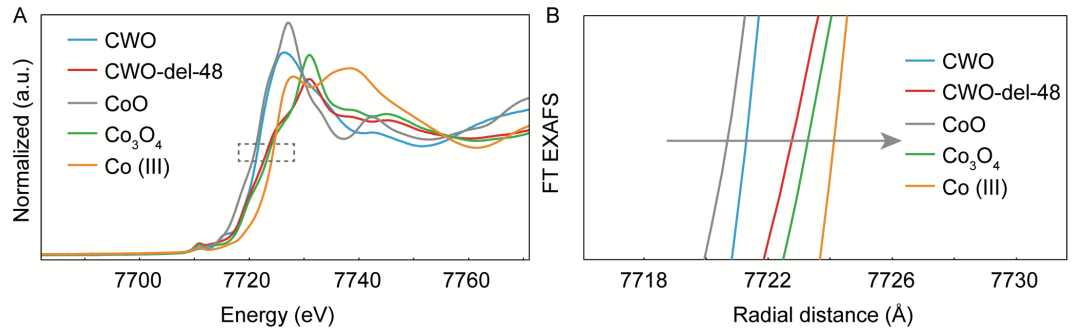

Fig. S18. XANES spectra of different Co based samples. (A) Co K edges of XANES for CWO, CWO–del–48, CoO and Co (III), and (B) corresponding zoomed region at 50% intensity height.

To study the impact of delamination on chemical states and electronic structure of CWO catalysts, we employed *ex situ* Co K edges of XANES, EXAFS and W L_3 edges of EXAFS.

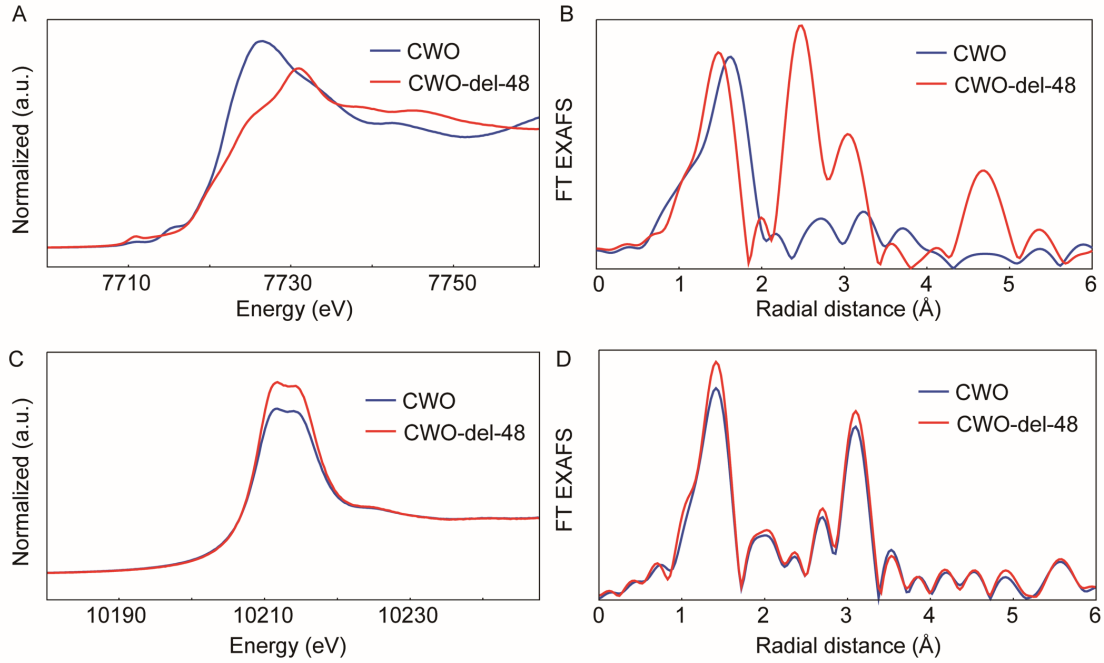

Fig. S19. XANES and EXAFS. Co K edges and W L_3 edges of XANES for CWO before and after delamination and corresponding R-zone coordination in EXAFS.

The right shift in absorption edge at 50% height in XANES, and the peak shift and emerging peaks in EXAFS of Co K-edge suggest potentially higher oxidation state of Co in CWO–del–48 than CWO, indicating that delamination treatment slightly oxidizes Co and changes the coordination environment of Co.

Meanwhile, the XANES and EXAFS of W L_3-edge show a slight change, which can be caused by elemental leaching by the high energy X-ray beam. The Fourier transformed EXAFS (FT-EXAFS, Fig. S19, B) indicates that Co–O bond distance becomes shorter after delamination. Additionally, the new features after 2 Å radial distance in CWO–del–48 indicates that Co bonding environment has changed significantly after delamination. The incorporation of water and hydroxide may lead to this substantial change in Co bonding by increasing its coordination number.

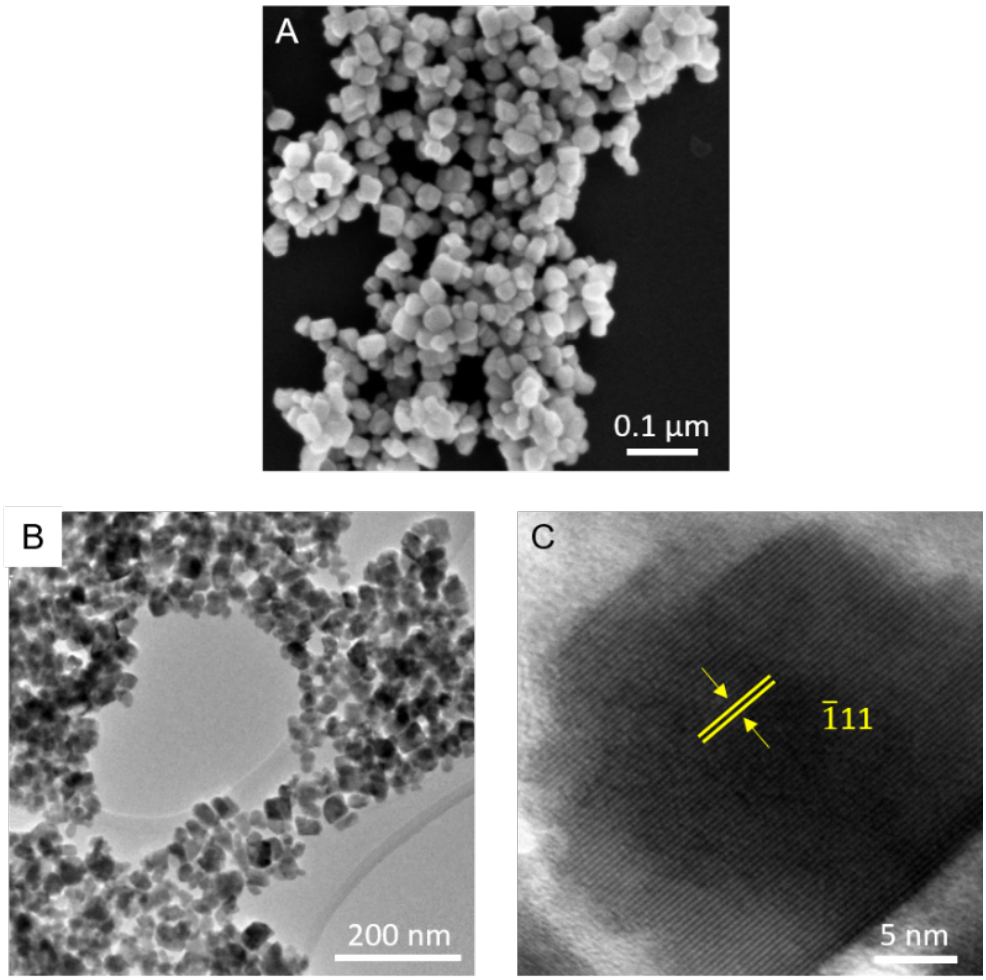

Fig. S20. Microstructure of CWO. (A) and (B) Scanning electron micrograph and low-magnification bright-field transmission electron micrograph (TEM) of as-synthesized CWO, respectively, depict a uniform cube-like morphology of the nanocrystals. (C) High-resolution TEM shows the regular crystal planes of the CWO nanocube. The lattice spacing of 2.91 Å, matches with the $(\bar{1}11)$ crystal plane of monoclinic $CoWO_4$.

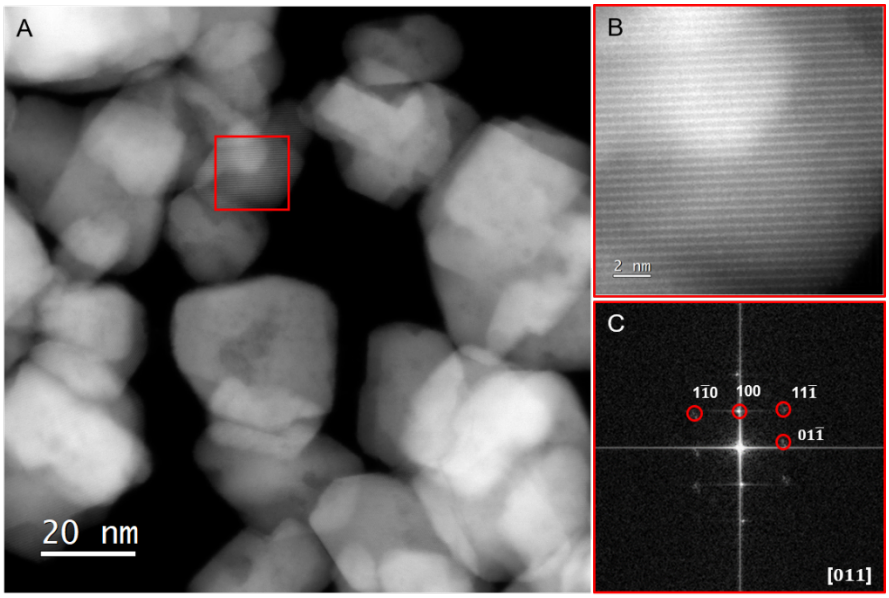

Fig. S21. STEM analysis of CWO. (A) High angle annular dark field STEM (HAADF-STEM) image shows a cube-like structure of CWO, coinciding with SEM and TEM micrographs. (B) The lattice-resolved HAADF-STEM of the red-boxed nanocrystal shows the resolved crystal planes of CWO and (C) the corresponding fast Fourier transformed (FFT) image displays ($\bar{1}\bar{1}0$), (100), ($11\bar{1}$) and ($01\bar{1}$) crystal planes along [011] zone axis.

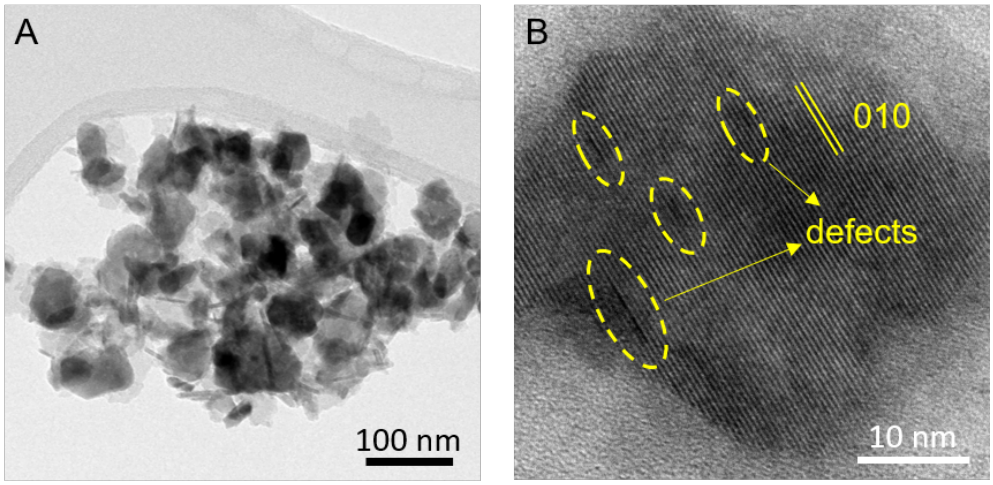

Fig. S22. TEM study of CWO–del–48. (A) The bright-field TEM image of CWO–del–48 reveals a flake-like shape. The KOH treatment driven delamination is evident, coinciding with SEM studies. (B) The high-resolution TEM image displays the (010) crystal plane of monoclinic $CoWO_4$ phase. The base treatment results in stacking fault defects; the missing lattice planes are shown in yellow-marked rings. These defects can arise from leaching of WO_4^{2-}, resulting from anion-vacancies.

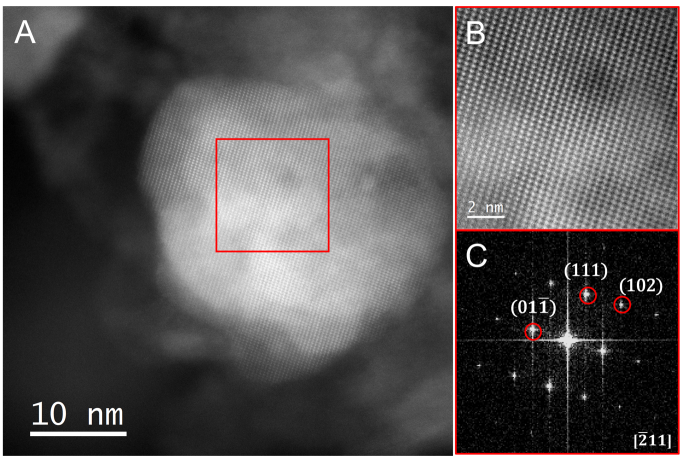

Fig S23. STEM analysis of CWO–del–48. (A) The HAADF-STEM image shows the delaminated flake-like morphology of CWO–del–48, consistent with the SEM and TEM micrographs. (B) The lattice-resolved HAADF-STEM from the red-boxed part of the nanocrystal shows the resolved crystal planes of CWO–del–48 and (C) the corresponding fast Fourier transformed (FFT) image displays (01$\bar{1}$), (111) and (102) crystal planes, along [$\bar{2}$11] zone axis.

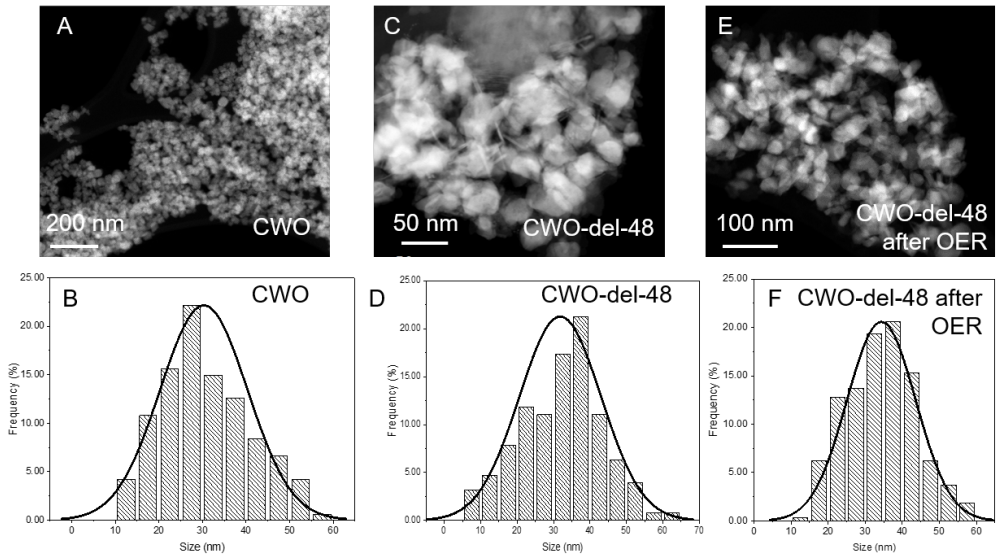

Fig S24. Estimation of Particle size distribution. (A, C, E) Low magnification HAADF-STEM images of the CWO, CWO–del–48 before and after OER (12 h), respectively, and corresponding (B, D, F) histogram depicting the particle size distribution. The average size of CWO–del–48 after OER is 34.3 ± 9.3 nm (a total of 321 nanocrystals were measured). This aligns with similar findings in the size measurements of both the pristine sample (30.3 ± 10.0 nm) and the delaminated samples (31.8 ± 11.2 nm), indicating that the particle size remains similar after the delamination of CWO and also after the OER of CWO–del–48.

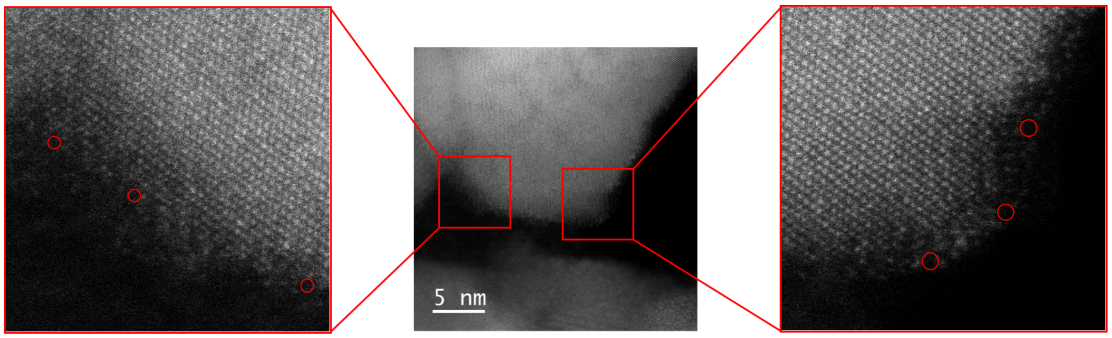

Fig. S25. Atomic-resolved HAADF-STEM image of the CWO–del–48. The surface presents irregular termination with vacancies and monoatomic steps (vacancies were highlighted in red on the surface), confirming the results from other techniques (EDS, EELS, EPR spectra) regarding the formation of vacancies. The presence of surface vacancies and defects increases the number of uncoordinated surface atoms, allowing a higher reactivity.

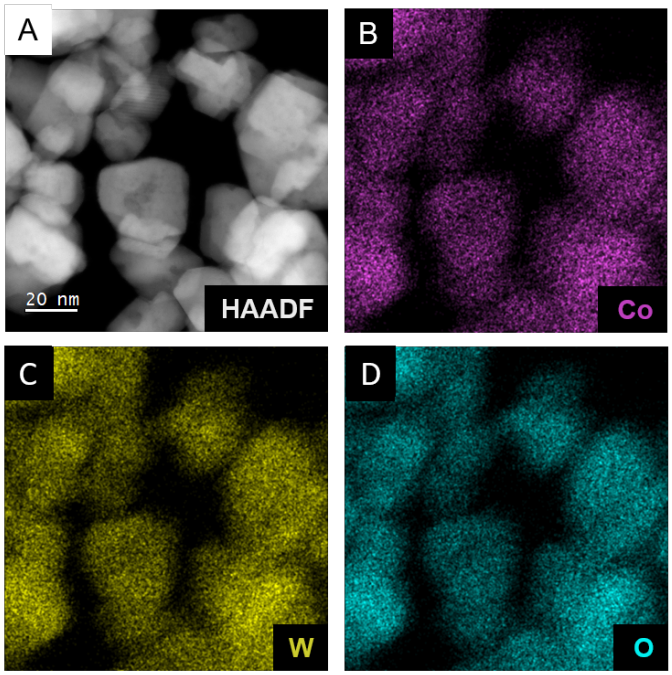

Fig. S26. Elemental analysis of CWO. (A) HAADF-STEM image of CWO, (B), (C) and (D) show the energy dispersive X-ray spectra (EDS) elemental mapping of Co, W and O respectively. The STEM-EDS mapping indicate the uniform elemental distribution of Co, W and O across the CWO nanocuboids.

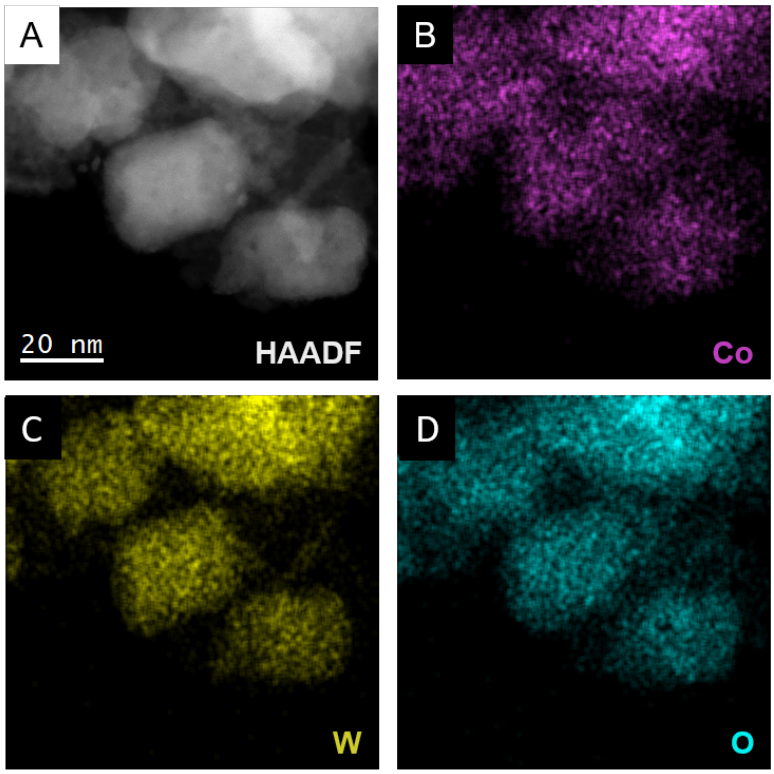

Fig. S27. Elemental analysis of CWO–del–48. (A) HAADF-STEM image of CWO–del–48, (B), (C) and (D) show the energy dispersive X-ray spectra (EDS) elemental mapping of Co, W and O respectively. The quantified STEM-EDS mapping demonstrate the uniform elemental distribution of Co, W and O across the CWO–del–48 nanocrystals, which is like CWO.

To assess the leaching of W after delamination, we performed EELS spectra of both CWO and CWO–del–48. As compared with the CWO, a decrease on the W content in CWO–del–48 can be confirmed. Moreover, as opposed to the pristine catalyst, minor signal of Fe was detected (see the blue circle). This Fe could be incorporated during the delamination process from KOH, which usually contains Fe impurities. However, it is important to note that despite the detection of Fe, the EELS quantification suggests an atomic composition of 0 ± 0.03 for this element. As a result, it was not included in the final composition due to the uncertainty associated with its presence.

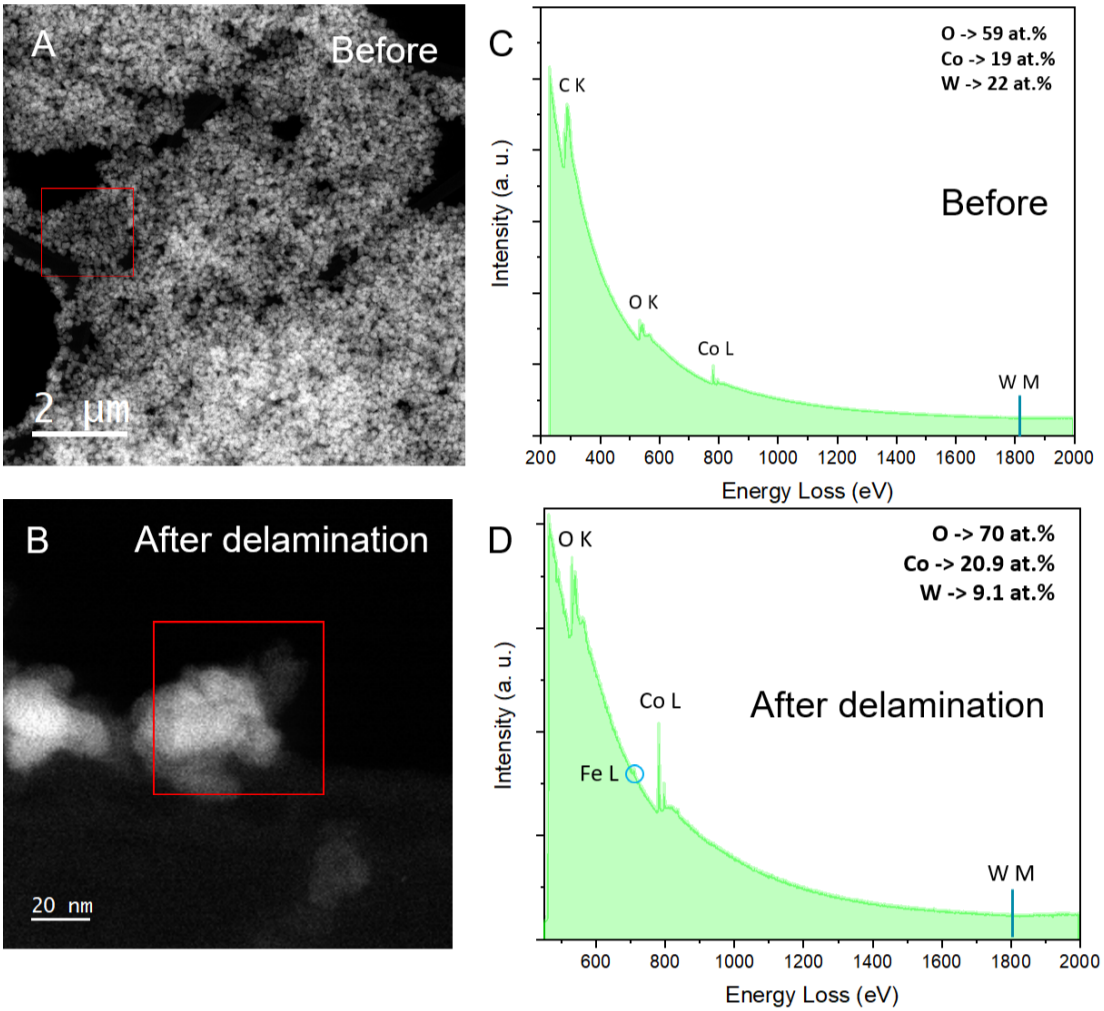

Fig. S28. EELS spectra. CWO (A, C) and CWO–del–48 (B, D), with the K-, L- and M-edges of O, Co and W, respectively.

Topography and phase

To acquire the topographic characteristics, CWO–del–48 was drop-casted on an atomically flat surface (SiO_2/Si) and areas with a wide distribution of particle sizes were investigated. The majority of the particles were agglomerated, as seen previously from electron microscopies, but also thinner specimens could be identified. Fig. S29 shows the topography and phase of CWO–del–48 showcasing the multifaceted nature of the material. In Fig. S29, D we can distinguish the variation of properties arising from alternate areas of the same particle. Terrace edges and different facets exhibit significant fluctuation and ideally, they can be exploited for different surface reactions. This disparity in properties led us to investigate in more detail the nanoscale features of our particles, which prompted the nanomechanical and nanoelectrical characterization that follows.

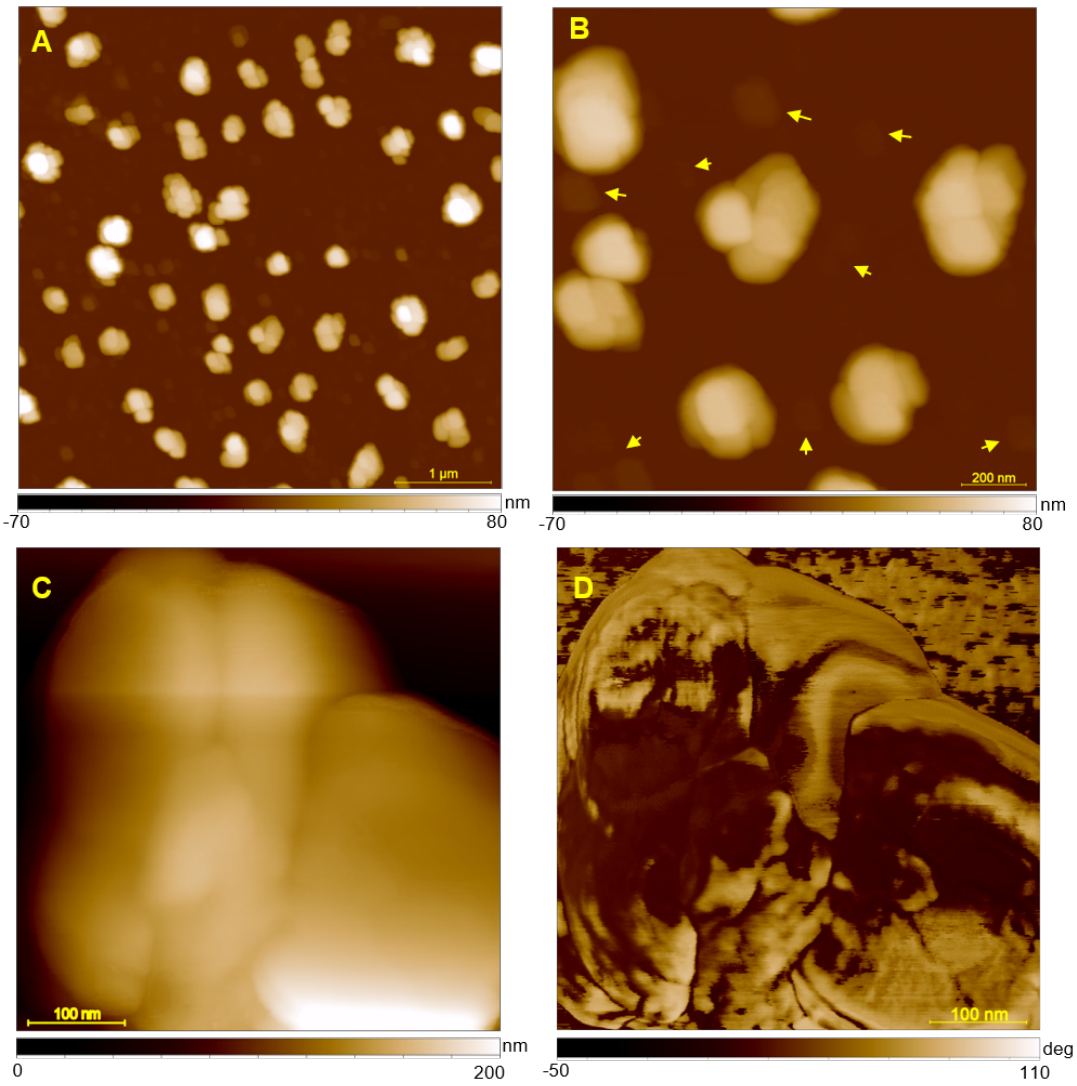

Fig. S29. Representative topographic images of CWO–del–48 sample. (A, B) Topography of agglomerated and delaminated specimens on a SiO_2 substrate. Yellow arrows in (B) denote ultra-thin particles. (C) High-magnification topography of a CWO–del–48 surface with its respective (D) phase. The topography depicts various facets with different properties as seen from the phase mapping.

Mechanical properties

To acquire nanomechanical data, PinPoint^{TM} was employed in contact mode. As the tip is scanned across the surface, a nanoindentation at a set force is performed and a force-distance curve is extracted at each pixel. From these curves we can obtain properties such as adhesion, dissipation, Young's modulus and deformation and create the respective nanomechanical mappings. Since we are operating in contact mode, we can also get friction characteristics of our samples. Nanomechanical mappings of CWO–del–48 particles highlight the variability of

properties occurring from different facets and agglomeration, with easily discernible boundaries for ultrathin particles. The variation of mechanical properties makes it easier to visualize smaller particles due to the difference between them and the SiO_2 substrate. We can observe higher adhesion at the boundaries of the terraces as well as on specific facets of the agglomerated particle. These sites can act as areas of increased activity and result in more efficient adsorption of water molecules. The rest of the mappings denote a wide range of properties we can tune by exposing various surfaces and stacking of the same material. The engineering of nanomechanical properties can provide us with robust electrodes of increased wear resistance, augmenting the increased observed stability and negligible leaching of the catalyst.

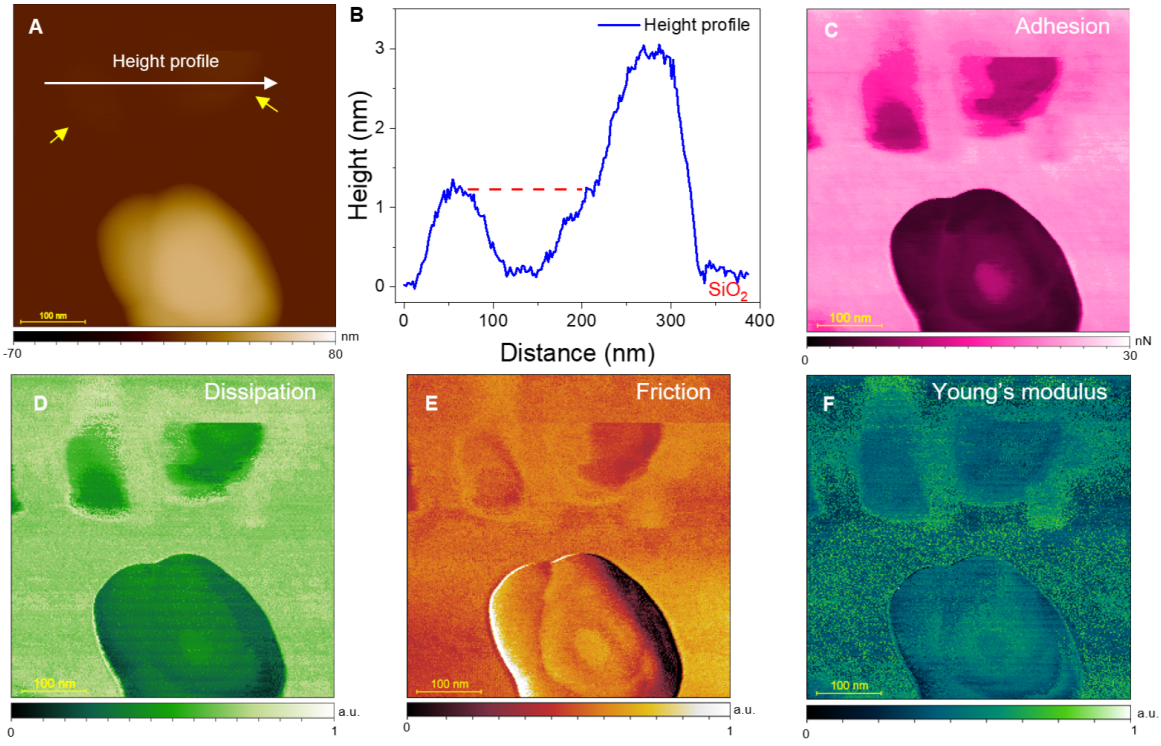

Fig. S30. Topography and nanomechanical mappings of thin and agglomerated particles. (A) Representative topography of CWO–del–48 particles. Yellow arrows denote thinner particles. (B) Height profile of the ultra-thin particles of (A). The red dashed line highlights an agglomerated particle of smaller thickness at the outer domain of the agglomeration. (C-F) Nanomechanical maps of (C) adhesion, (D) dissipation, (E) friction and (F) Young's Modulus show the variation of properties at the terrace edges and as the thickness diminishes. The smaller particles are much more visible due to property variation as a function of thickness.

Atomic resolution

Atomic resolution imaging requires the reduction of thermal vibrations and a flat surface, and ideally single crystal samples – not the case of the CWO-del samples studied herein. Atomic resolution images were acquired on various facets of CWO–del–48 samples. Bigger areas can help us visualize better any inconsistencies within the lattice.

The topography of a multifaceted particle (Fig. S31, A) displays a periodic lattice, disrupted by vacancies scattered throughout the facets. Correlating the topography with the phase image on the same facet, we can observe subtle changes at the points of interest denoting a discontinuity in the lattice. By decreasing the scan window, we can clearly see the lattice pattern and we can correlate the atomic distances closely matched with TEM. Various defects are also visible (dashed circles). The slight misalignment of the lattice is attributed to the thermal vibrations occurring during the experiment under ambient conditions. Additionally, the resolution is limited by the radius of the tip.

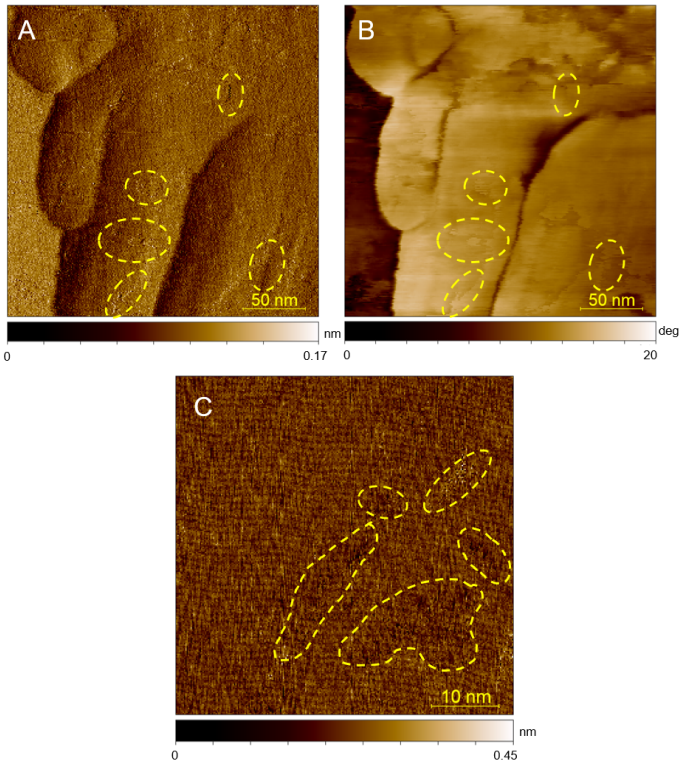

Fig. S31. Atomic resolution image of CWO–del–48 sample. (A) Topography and (B) phase images of a representative sample surface. (C) Lattice resolution of CWO–del–48. Slight misalignment of the lattice is due to the thermal drift from ambient conditions. Dashed circles denote areas with defects.

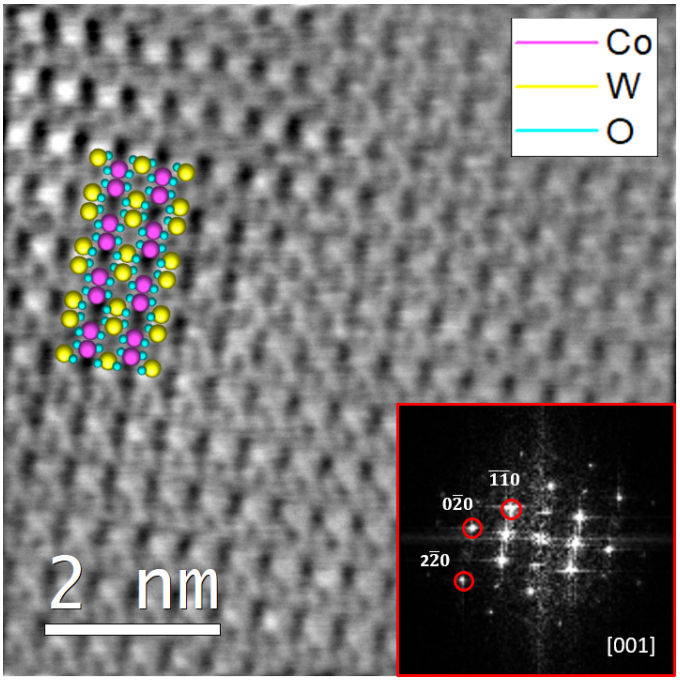

Fig. S32. iDPC-STEM of as-synthesized CWO. Spherical aberration corrected atomic resolution image of CWO nanocuboid. The resolved Co, W and O atoms are shown. Depending on the atomic number of the atoms, Co and W scatter accordingly. The O-atoms are shared by Co and W atoms. The inset displays the corresponding FFT image. $(2\bar{2}0)$, $(0\bar{2}0)$ and $(\bar{1}\bar{1}0)$ are the indexed crystal planes along [001] zone-axis.

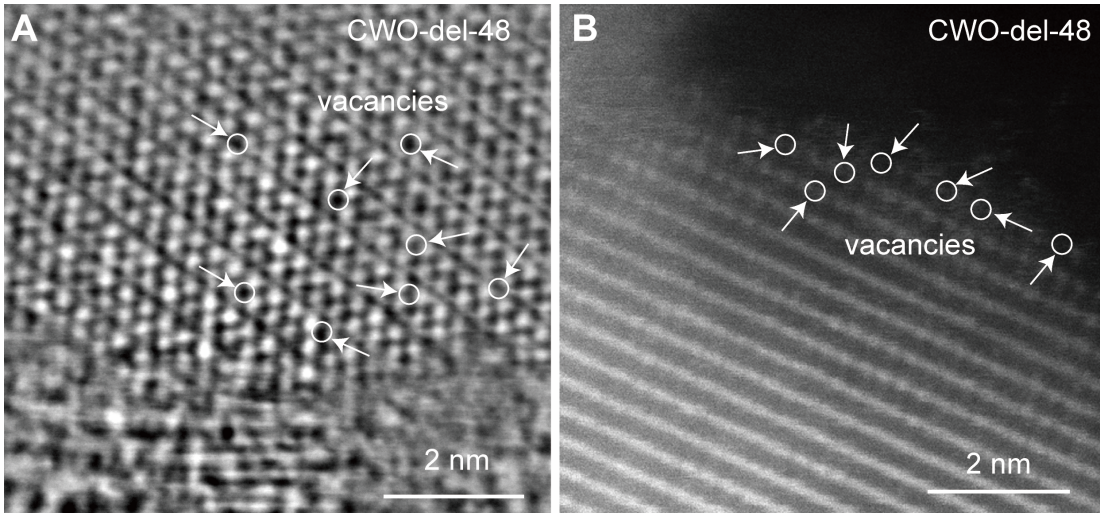

Fig. S33. iDPC and HAADF-STEM imaging of CWO-del-48. (A) iDPC-STEM image shows the missing O-atoms (white circled), and (B) HAADF-STEM micrographs of CWO–del–48 exhibits W-vacancies, generated from WO_4^{2-} leaching due to the base treatment of CWO.

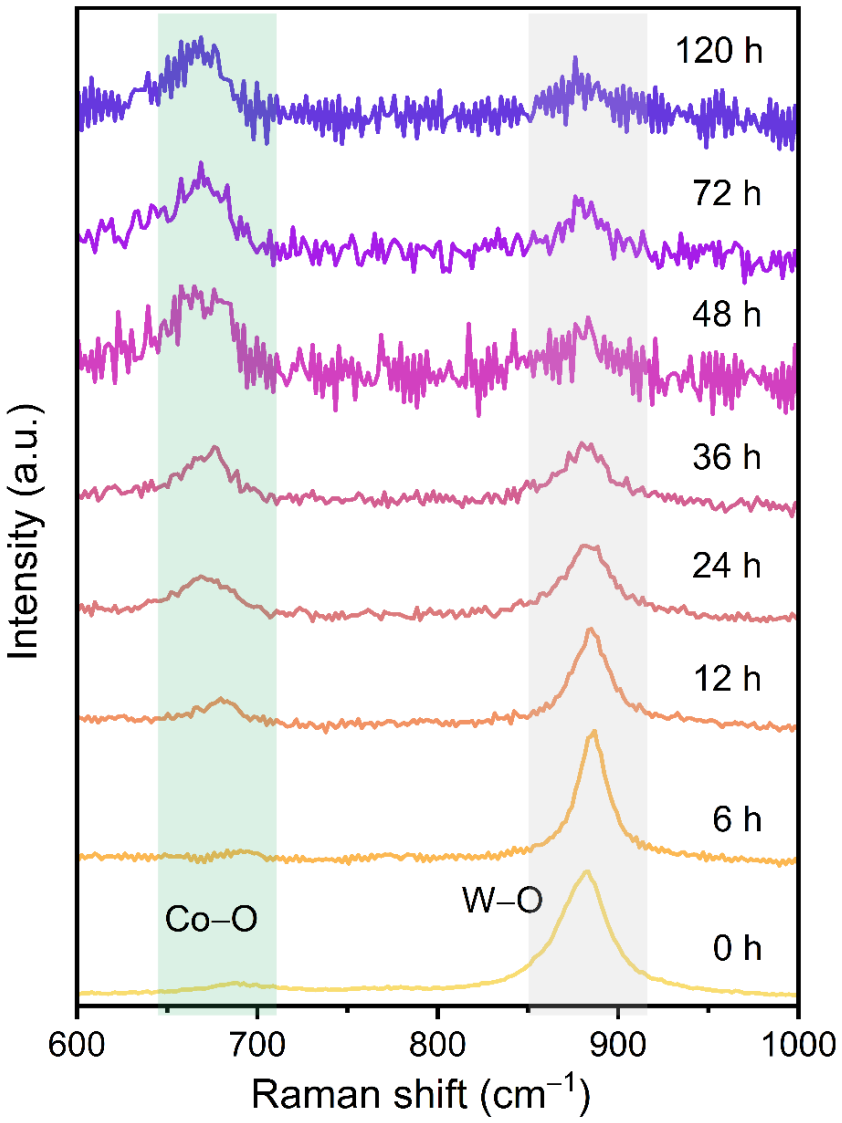

Fig. S34. Time dependant *ex situ* Raman spectra analysis. We obtained Raman spectra of CWO and KOH-treated samples with different delamination time (0 h to 120 h) to study the kinetic limit of W-leaching. The intensity ratio ($I_{Co–O}/I_{W–O}$) of Co–O (~690 cm^{-1}) to W–O (~886 cm^{-1}) Raman peaks of the compounds, obtained at different delamination time, increases rapidly until 24 h, and starts saturating after 48 h. This suggests that the anion exchange reaction from CWO has a kinetic limitation.

Table S8. I_{Co-O} / I_{W-O} ratio calculation from ex-situ Raman spectra of CWO and CWO–del–products at different reaction time (0 h to 120 h), from Fig. S34.

Material	I_{Co-O} value	I_{W-O} value	I_{Co-O} / I_{W-O} ratio
CWO (0 h)	634.2	3718.6	0.17
CWO–del–6	566.2	1798.1	0.31
CWO–del–12	379.6	814.4	0.46
CWO–del–24	356.3	542.2	0.66
CWO–del–36	254.0	273.2	0.93
CWO–del–48	147.2	122.0	1.20
CWO–del–72	163.1	126.3	1.29
CWO–del–120	195.1	145.9	1.34

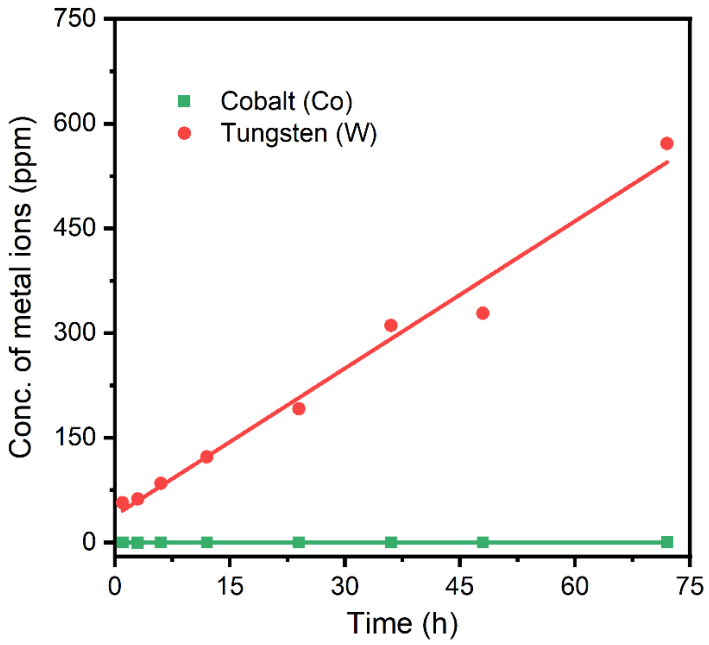

Fig. S35. ICP-OES. The concentration of Co and W leaching from CWO under 0.1 M KOH treatment varying reaction time. The conc. of ejected W increased linearly with reaction time. The amount of Co leaching from CWO crystal, on the other hand, almost negligible with compared to W. The ICP-OES study suggested the possibility of W elimination in the form of WO_4^{2-} from the crystal lattices of $CoWO_4$. Thus, the base treatment could lead to anion-vacancies in the crystal.

Table S9. ICP-OES: Co and W leaching from CWO under aq. KOH treatment at different reaction time.

Reaction time (h)	Conc. of Co (ppm)	Conc. of W (ppm)
1	0.02	57.05
3	0.00	62.37
6	0.01	84.74
12	0.03	122.51
24	0.05	191.74
36	0.08	328.38
48	0.06	311.04
72	0.28	571.65

To understand the delamination energy as a function of the crystal orientation, we have taken seven different surfaces (<010>, <100>, <001>, <110>, <011>, <101>, <111>). For each, we have computed the surface energies and the WO_4^{2-} elimination energies, see Table S9. The obtained data demonstrates that even in the least favorable case, the delamination process is exothermic by more than 2 eV.

Table S10. Surface energies, g (eV/Å^2), of the seven lowest surface energy planes.

	<010>	<100>	<001>	<110>	<011>	<101>	<111>
g (eV/Å^2)	0.043	1.387	0.081	0.066	0.067	0.064	0.075

Table S11. Surface energies, g (eV/Å^2), of the seven lowest surface energy planes.

Layers	ΔE_{del} (eV)	$\Delta E_{del}/n(WO_4^{2-})$ (eV)	ΔE (1→2) (eV)
1	–4.49	–4.49	–
1+2	–2.49	–1.23	1.62

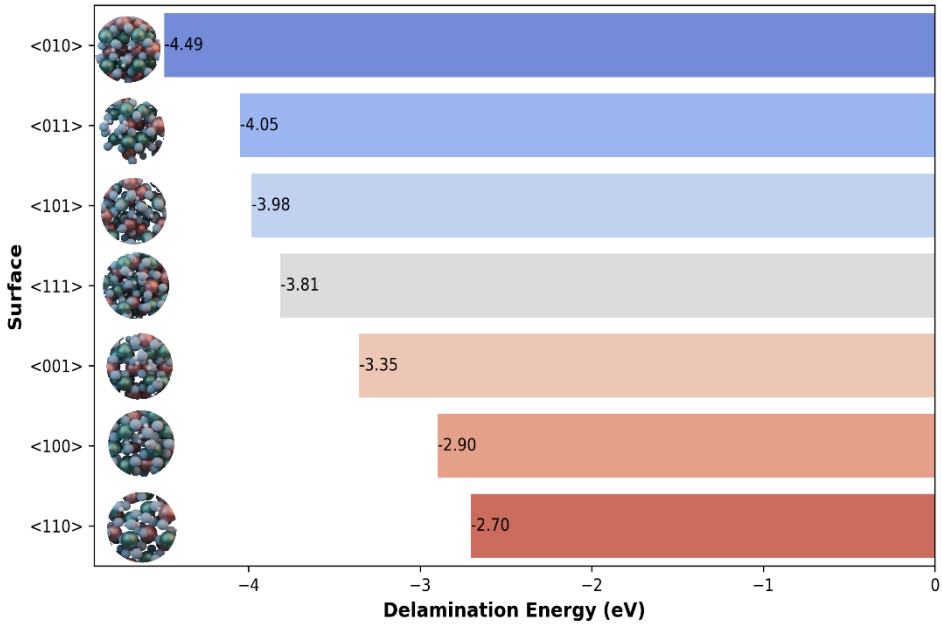

Fig. S36. Delamination energy. E_{del} in eV, from the lattice as a function of the surface orientations of <010>, <011>, <101>, <111>, <001>, <100>, <110>. This observation underscores the directional preference of delamination processes, highlighting its sensitivity to specific orientations.

In addition, we have computed the intermediates of a potential reaction path for the elimination of the cation, Fig. S37.

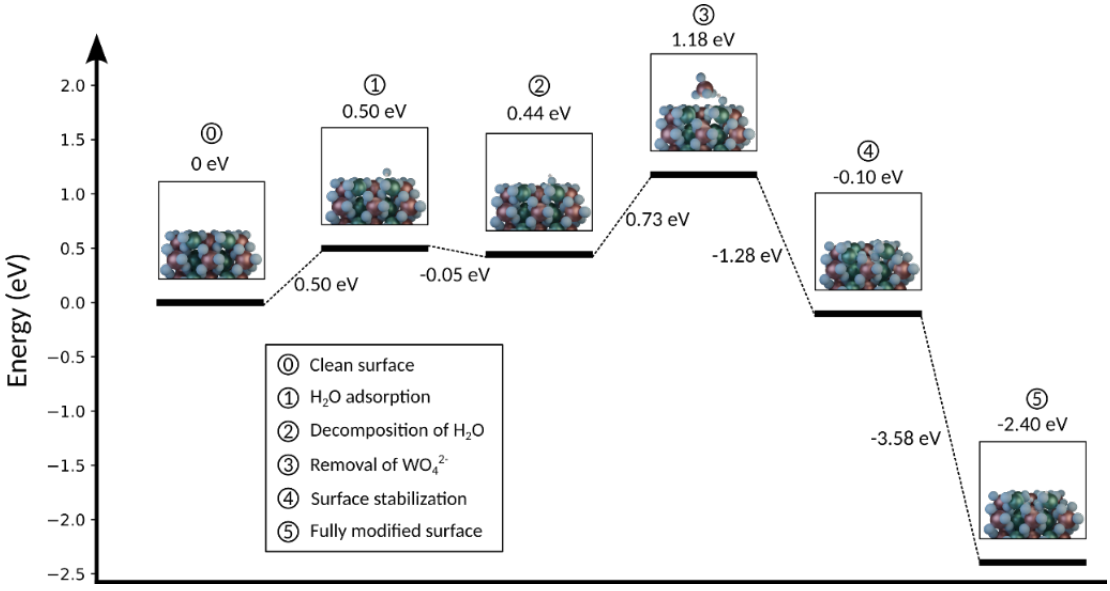

Fig. S37. Suggested energy reaction intermediates for the first step in the delamination of CWO <010> surface.

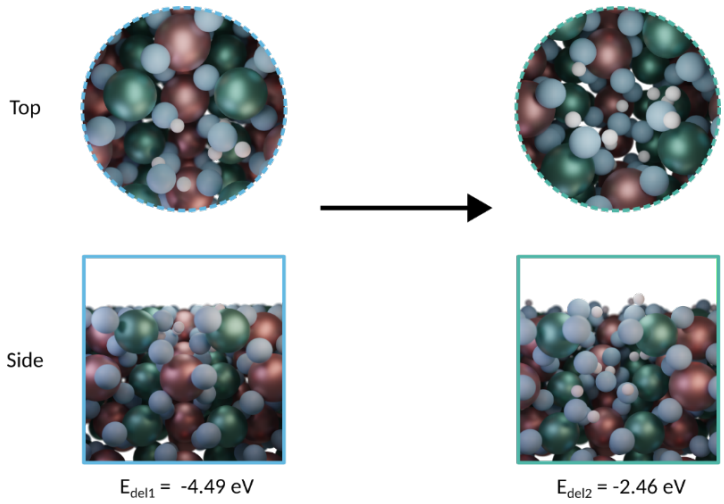

Fig. S38. Potential second layer reconstruction in CWO <010> surface, DFT simulation analysis.

To assess the potential trapping of water species, we performed thermogravimetric analysis coupled with mass spectrometer (TGA-MS) for CWO–del–48, CWO and Co_3O_4 from 40°C to 800°C with the temperature increment of 10°C/min. All samples have been stabilized to 40°C during one hour prior to ramping. Thermogravimetric analysis coupled with mass spectroscopy revealed ~16 % weight loss for CWO–del–48 over 166.7°-395.5°C due to water/hydroxyl ions which is negligible for CWO and Co_3O_4. Four distinct peaks at 140°C, 222°C, 254°C and 333°C reveals four different types of water present in CWO–del–48 (Fig. S39).

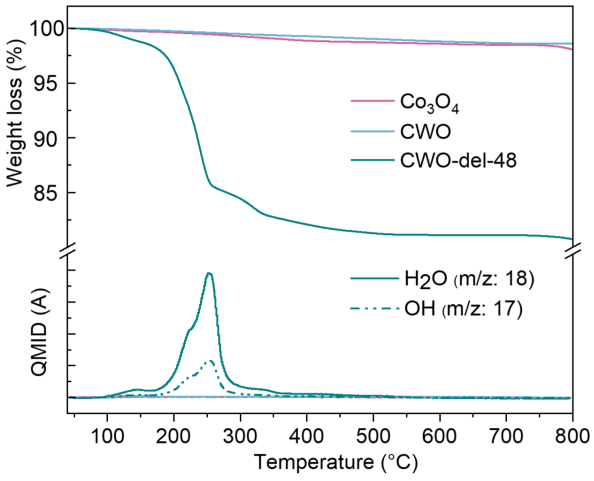

Fig. S39. TGA-MS analysis. Thermogravimetric analysis coupled with mass spectrometry (TGA-MS) reveals the presence of trapped water and OH in CWO–del–48 *vs.* CWO and Co_3O_4.

Mass spectrometry linked the weight loss of CWO–del–48 to water (m/z = 18) and hydroxyl ions (m/z = 17) species. This provides strong evidence of the existence of water/hydroxyl ions in CWO–del–48, which is negligible for CWO and Co_3O_4.

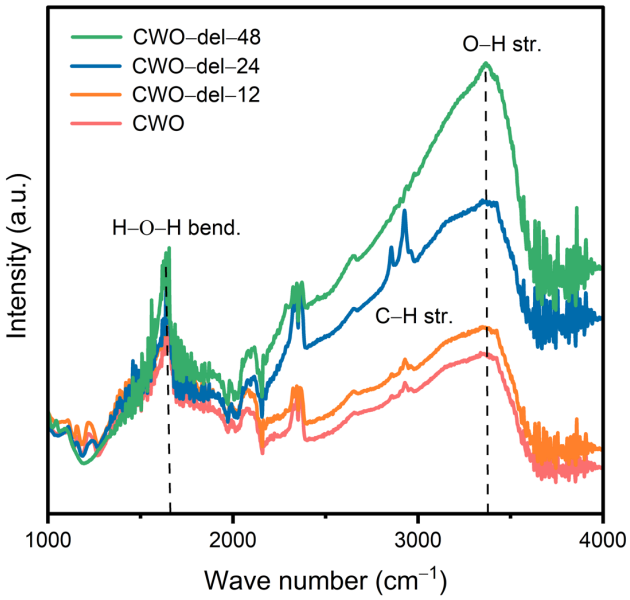

Fig. S40. ATR-FTIR spectra study. The infrared spectra of CWO and CWO–del–products display the presence characteristic broad O–H stretching and H–O–H bending vibrational modes. The as-synthesized CWO has some extent of water coverage. The higher intensity of O–H stretching and H–O–H bending features in CWO–del–48 than that of CWO suggests the presence of water and/or OH^- in CWO–del–48. The increase in intensity of the O–H stretching peak in CWO–del–48 (higher than the increase in H–O–H bending), further suggests the presence of hydroxide (OH^-) ions within CWO-del resulting from anion exchange (replacement of WO_4^{2-} ions by OH^- and H_2O).

We extensively investigated the presence of water and hydroxide in CWO and CWO–del–48 using isotope-exchange experiments and Raman spectroscopy. Three types of water can exist within the samples: solid-like water (4 hydrogen bonded water, 4–HB·H_2O, ~3200 cm^{-1}), liquid like water (3 hydrogen bonded water, 3–HB·H_2O, ~3400 cm^{-1}) and free water (0 hydrogen bonded water, 0–HB·H_2O, ~3600 cm^{-1}). It is expected that the water inside the layer or pores of a material is most likely remains in solid like water with more strongly hydrogen bonded with neighboring atoms *(43)*. To assess this trapped water, *ex situ* Raman spectroscopy measurements of both CWO and CWO–del–48 were performed using a diode laser (532 nm) and a 20x objective with a 0.75 numerical aperture. Water H–OH stretching modes are detected

for both CWO and CWO–del–48 (Fig. S41). The water stretching peak in CWO–del–48 is much narrower (~3248 cm^{-1}), compared to CWO. The broad H–OH stretching mode present in CWO confirms the presence of adsorbed bulk water on the CWO surfaces. On the other hand, the narrow single peak of H–OH stretching mode confirms the strongly hydrogen bonded water with neighboring atoms present in the CWO–del–48.

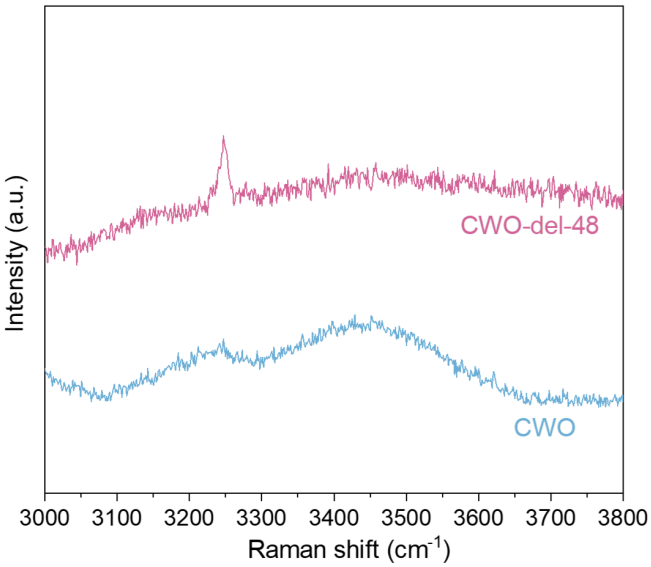

Fig. S41. *Ex situ* Raman spectra of CWO and CWO–del–48. The spectra show the water stretching modes for both CWO and CWO–del–48 in between 3100 to 3650 cm^{-1} of Raman shift. The presence of a broad peak for H–OH stretching mode in CWO is compatible with the presence of adsorbed bulk water on CWO surfaces. On the other hand, the narrow single peak (~3248 cm^{-1}) of H–OH stretching mode suggests the presence of trapped solid-like water in CWO–del–48. All traces were taken using a 532 nm excitation with a grating of 1800 I/mm, and 20x objective with a 0.75 numerical aperture.

To further challenge the presence of trapped water, we performed *ex situ* Raman spectroscopy measurements for CWO–del–48 after performing delamination of CWO in 0.1 M KOH in D_2O for 48 h. After comparing with the Raman spectra of CWO–del–48 with, we found that the peak for H–OH stretching mode shifted from ~3248 cm^{-1} to a broad peak (2300 – 2900 cm^{-1}) and a narrow peak (~2443 cm^{-1}) of D_2O after 48 h (CWO–del–D_2O–48) and 72 h of delamination (CWO–del–D_2O–72, Fig. S42, A), respectively (*44*).

To assess the potential of adsorbed *vs.* trapped D_2O, we heated both CWO–del–D_2O–48 and CWO–del–D_2O–72 for 18 h at 100°C. After heating, we found a single narrow peak of D_2O stretching mode (~2443 cm^{-1}) for both samples, confirming the presence of trapped D_2O in the

delaminated CWO in 0.1 M KOH in D_2O. The Raman spectra are subtracted from the baseline of a second order polynomial.

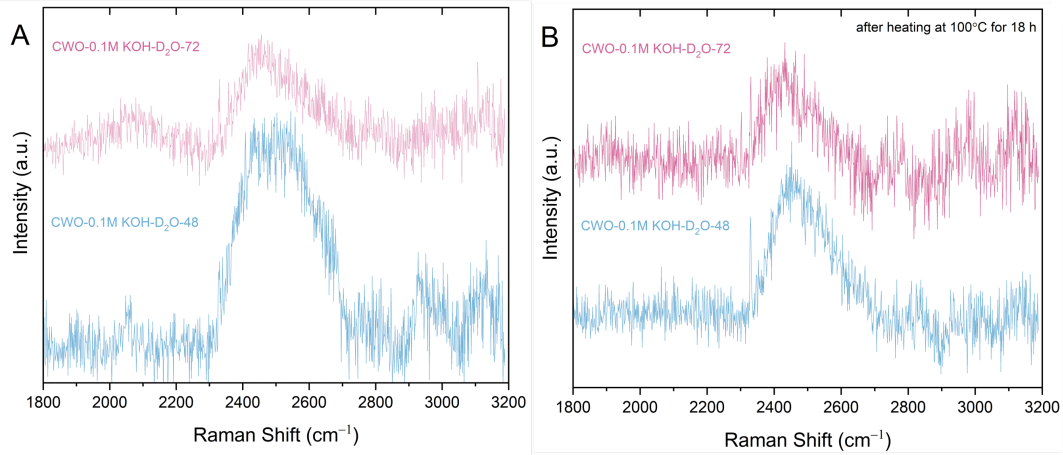

Fig. S42. *Ex situ* Raman spectroscopy studies of deuterated CWO–del–48. To detect the trapped water (via D_2O exchange) we performed *ex situ* Raman spectroscopy for deuterated CWO–del–48 and CWO–del–72, after delaminating CWO in 0.1 M KOH in D_2O for 48 h and 72 h, respectively. (A) We found a broad peak of D_2O for CWO–del–D_2O–48 compared to the single narrow peak of water present in the CWO–del–72. The narrow single peak of H_2O stretching mode shifted from ~3248 cm^{-1} to ~2443 cm^{-1} of D_2O stretching peak confirming the presence of trapped water for CWO–del–72. (B) Further, we heated CWO–del–D_2O–48 and CWO–del–D_2O–72 at 100°C for 18 h to remove any adsorbed D_2O on the surfaces. After performing the *ex situ* Raman spectroscopy, we found a single narrow peak of D_2O for both, supporting the presence of solid-like D_2O inside CWO–del–D_2O–48 and CWO–del–D_2O–72.

Table S12. DFT analysis of solvation energy for H_2O, H_2WO_4, H_3O^+ and other anions: a comparative study utilizing Gaussian with WB97XD functional and LANL2DZ basis set in vacuum and solvated Systems (water, DMSO).

E_{solv}	Water (eV)	DMSO (eV)
OH^-	–4.67	–3.19
H_2O	–0.52	– 0.27
H_3O^+	–4.10	–3.24
HWO_4^-	–5.08	–2.80
H_2WO_4	–3.43	–0.99
WO_4^{2-}	–10.10	–7.12
MoO_4^{2-}	–10.85	–8.49

Table S13. Thermal-Related Parameters of CWO–del at T=300K Calculated Using Phonopy: Vibrational Energy (E_{vib}, eV), Entropy (S, eV), Heat Capacity (C, eV/K), and Zero Point Energy (ZPE, eV/K) Derived from Supercell and Finite Displacement Methods.

	E_{vib} (eV)	S (eV/K)	C (eV/K)	ZPE (eV)
$CWO(H_2O)_4$	0.00068	0.00064	0.00071	0.75869
$CWO(H_2O)_2(OH)_2$	0.00018	0.00116	0.00108	0.52660
$CWO(H_2O)_3(OH)$	0.00071	0.00050	0.00059	0.77203
$CWO(H_2O)_2(OH)$	0.00042	0.00111	0.00106	0.57504
$CWO(H_2O)(OH)_2$	0.00036	0.00116	0.00108	0.52660
$CWO(H_2O)(OH)_3$	0.00057	0.00047	0.00058	0.63216

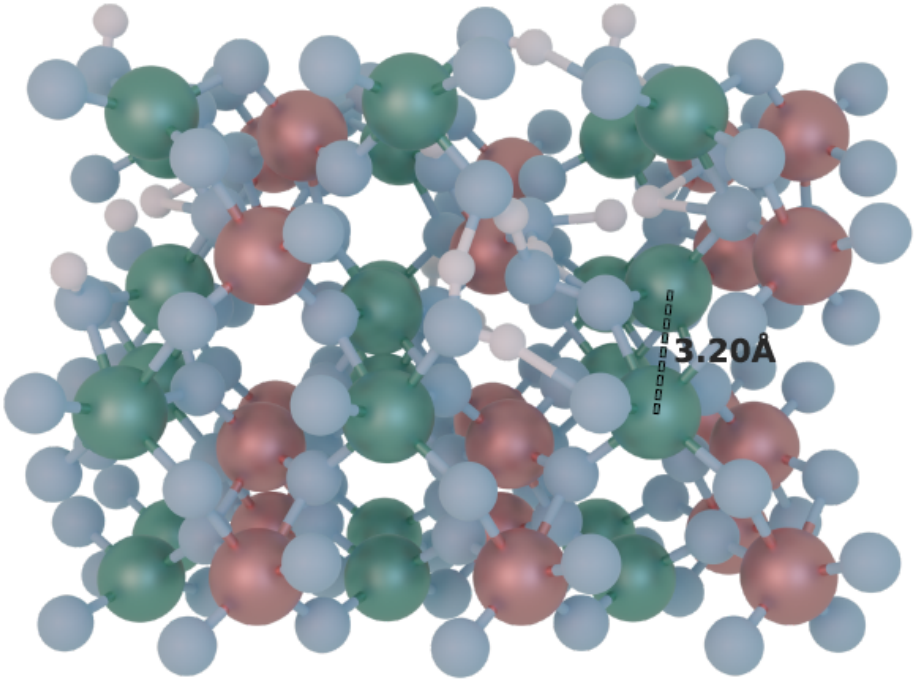

Fig. S43. The structure of CWO–del–48. $Co(WO_4)_{1-x}(H_2O)_2(OH)_2$ crystal structure is oriented along b-axis. In the atomistic model, Co, W, O and H atoms are designated in green, pink, blue and white colour. The trapped water and hydroxide bonded to Co-atoms. The hydroxide bonding results the formation of CoOOH moiety at the surface, which can enhance the OER activity of the catalyst. CWO–del–48 surface has higher abundance of Co^{3+} than that in CWO. Along with bonding with Co-atoms, trapped H_2O and OH^- get further stability through H-bonding (shown as dashed lines). The electron withdrawing of Co^{3+} could result the polarity of O–H bonds of the trapped water, increase the overall acidity of the material.

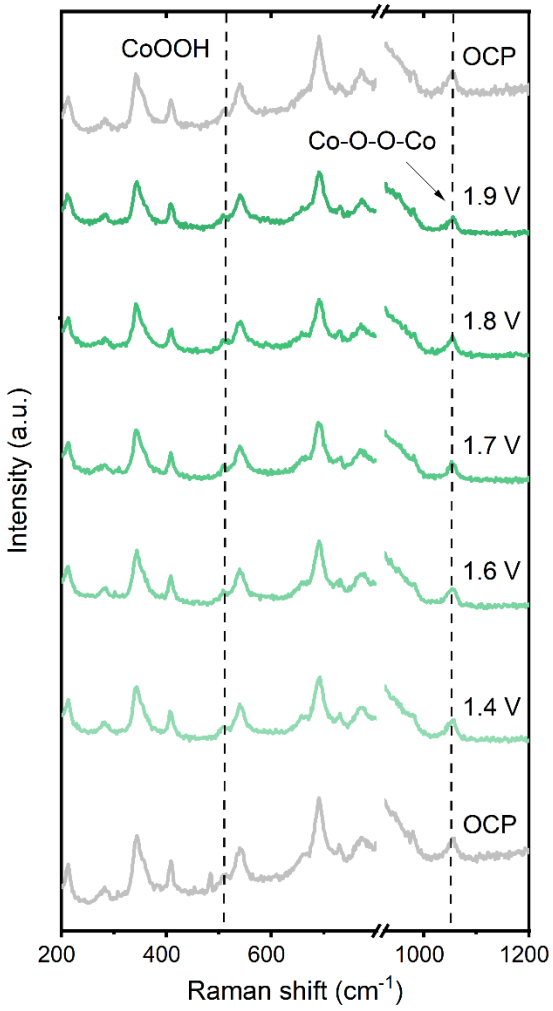

Fig. S44. *In situ* Raman spectroscopy study of CWO. Experiments were carried out in a 0.5 M H_2SO_4 electrolyte from OCP to different applied potential (1.4 to 1.9 V *vs.* RHE). At OCP, features of active metal-oxide species i.e. CoOOH (~517 cm^{-1}) and Co–O–O–Co (~1057 cm^{-1}) are observed *(46,47)*. Similar phenomena were observed in the case of CWO–del–48, which is supported by MOR results. Unlike CWO–del–48 catalyst, the intensity of CoOOH and Co–O–O–Co Raman active peaks of CWO does not increase with increased applied potential. This is compatible with the higher onset potential of CWO catalysts.

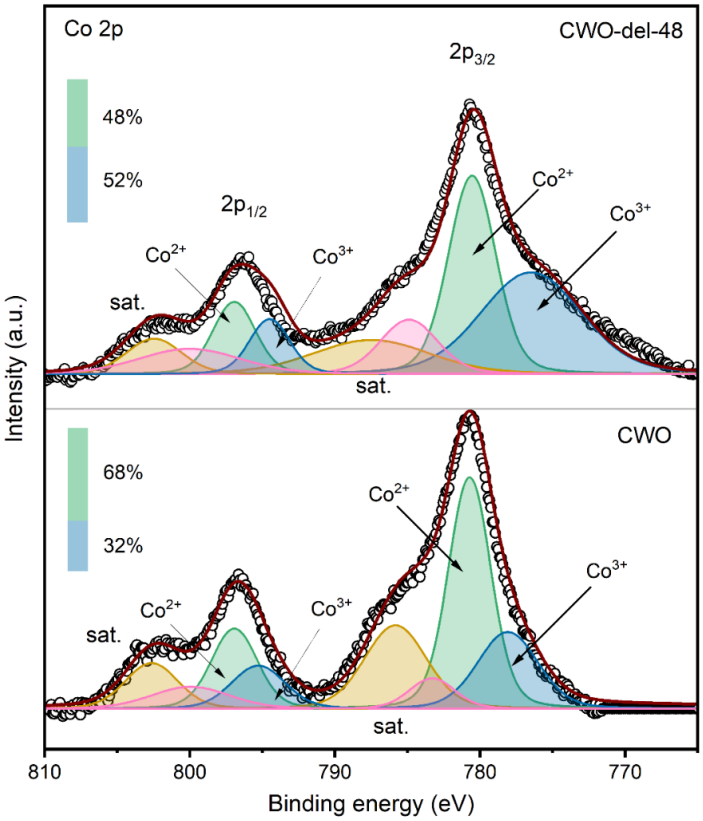

Fig. S45. XPS characterization. The high-resolution Co 2p core level XPS spectra of CWO and CWO–del–48 was deconvoluted into lower binding energy Co $2p_{3/2}$, higher binding energy (BE) $2p_{1/2}$ and Co satellite (sat.) peaks. The percentage of Co^{2+} and Co^{3+} in both materials was obtained by peak fitting. Co^{2+} and Co^{3+} in CWO have the BE of 780.5 eV and 778.3 eV respectively *(59)*. The higher percentage of Co^{3+} in CWO–del–48, signifies the higher presence of Co^{3+} at the surface of the material. Co^{2+} and Co^{3+} in CWO–del–48 slightly red shifted than that in CWO, indicate the increase in chemical stability in Co-bonding environment in CWO–del–48.

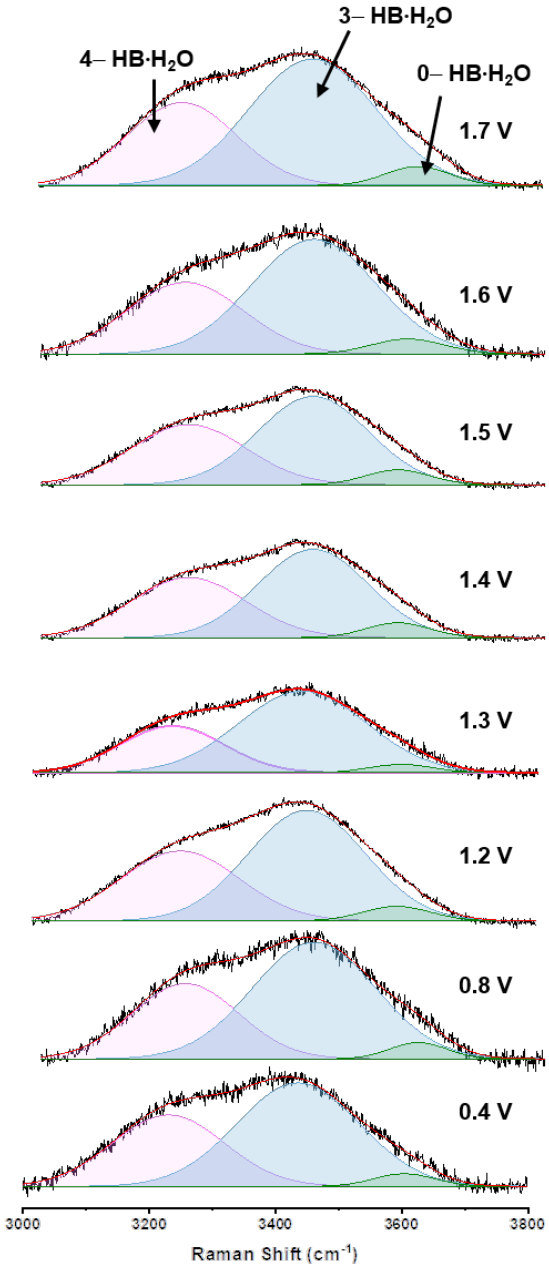

Fig. S46. Interfacial water study for CWO catalyst. The *in situ* Raman spectra of interfacial water on CWO catalysts over Ag/PTFE substrates fits in three different types of H-bonded water structures: 4–HB·H_2O (pink), 3–HB·H_2O (blue) and 0–HB·H_2O (green). The change in the percentage of different x–HB·H_2O is negligible for CWO catalyst at different applied potentials (0.4 V to 1.7 V *vs.* RHE).

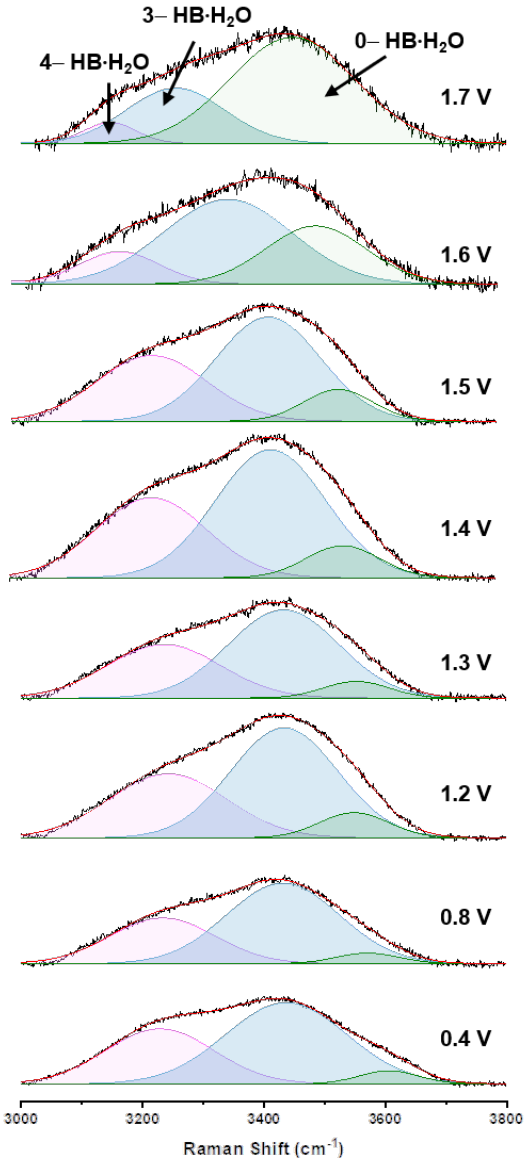

Fig. S47. Interfacial water study for CWO–del–48 catalyst. The *in situ* Raman spectra of interfacial water on CWO–del–48 catalysts on Ag/PTFE substrates fits in three different types of H-bonded water structures: 4–HB·H_2O (pink), 3–HB·H_2O (blue) and 0–HB·H_2O (green). With increase of applied potential from 0.4 V to 1.7 V *vs.* RHE, a progressive increase in the percentage of 0–HB·H_2O is observed. Concurrently, the percentage of 3–HB·H_2O and 4–HB·H_2O decrease with applying of higher anodic potential.

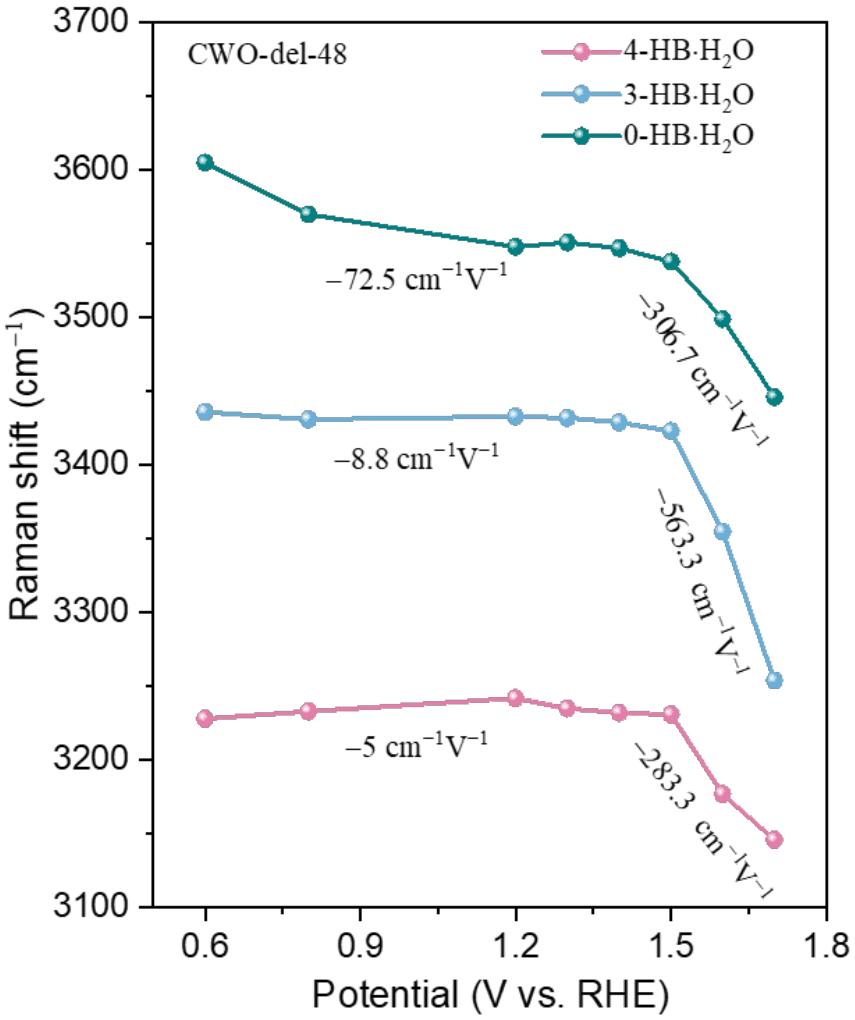

Fig. S48. Stark slope assessment from *in situ* Raman study of CWO−del−48. The potential-dependent Raman shift of the O–H stretching mode of different types of interfacial water (n–HB·H_2O) explains the nature of Stark effect. Until the OER onset potential (~1.5 V *vs.* RHE), the Stark slope changes slowly for different n–HB·H_2O. After 1.5 V, an abrupt change in Stark slope occurs with potential. This suggests that the water structure becomes more sensitive to the local electric field, indicating the active involvement of interfacial water in the OER pathway.

Table S14. Comparative analysis of the confined Reaction Pathways: Understanding the differences between normal cAEM and cOPM mechanisms with specific focus on the variances noted in the presence of H_2O/OH^- trapped in the system.

Mechanism	Material	Reaction pathway
cAEM	M: CWO $(H_2O)_2(OH)_2$	$M + H^+ + e^- \rightarrow M_1OH$
	M_1: $CWO(H_2O)_3$	$M_1OH \rightarrow M_1O + H^+ + e^-$
		$M_1O + H_2O \rightarrow M_1OOH + H^+ + e^-$
		$M_1O_2 + H_2O \rightarrow M + O_2 + 3H^+ + 3e^-$
cOPM	M: CWO $(H_2O)_2(OH)_2$	$M + H^+ + e^- \rightarrow M_1OH$
	M_1: $CWO(H_2O)_3$	$M_1OH + H_2O \rightarrow M_1OHO + 2H^+ + 2e^-$
		$M_1OHO \rightarrow M_1OO + H^+ + e^-$
		$M_1OO \rightarrow M + O_2 + 2H^+ + 2e^-$

Table S15. Thermodynamic Corrections for OER Intermediates: detailed values of Zero-Point Energy (ZPE, eV), Entropy (S, eV/K), and TS (eV) Utilized in Gibbs Free Energy Calculations.

	ZPE	S	T*S
***O**	0.0223	0.0002	0.0632
***OOH**	0.4191	0.0001	0.0463
OO	0.1270	0.0002	0.0863
***O*OH**	0.4173	0.0001	0.0499
***OH**	0.3494	0.0003	0.0969

Table S16. DFT Analysis of H_2O and H_2 Energies and Enthalpies at 300K for OER Pathway: Insights from Phonopy of Total Energy (E_{tot}, eV), Zero Point Energy (ZPE, eV), Gibbs Free Energy (G, eV), Entropy (S, eV/K), and Heat Capacity (C, eV/K), at T=300.

	E_{tot}	E_{vib}	S	C	ZPE	G
H_2O	–13.508	0.000027	0.002078	0.000261	0.573056	–13.48
H_2	–6.26	–0.00037	0.0025	0.00015	0.33827	–6.638

Table S17. Comprehensive Analysis of OER Intermediates on the Surface: Computed structural properties of the CWO–del–48 structure, relevant distances in Å.

	Co–Co	Co–Co	Co–O	Co–H_2O
***O**	4.93	4.80	1.71	2.07
***OH**	5.19	4.92	1.76	2.07
***O*OH**	4.96	4.97	1.73	2.02
OO	4.96	4.81	2.02	2.19
***OOH**	5.09	4.82	1.78	2.08

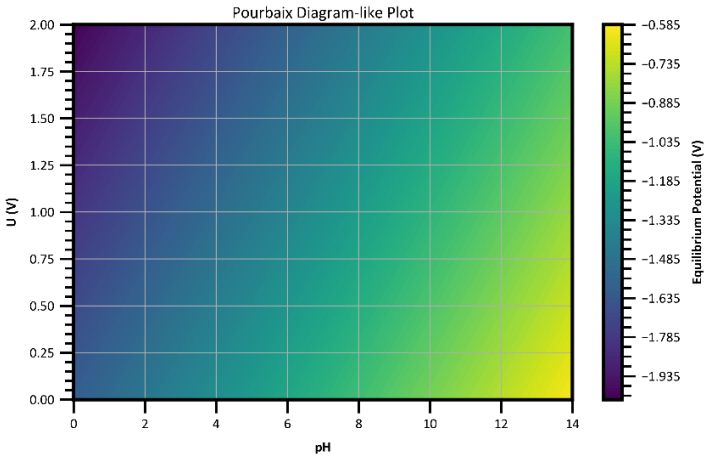

Fig. S49. Gibbs free energy landscape as a function of voltage and pH and potential for the intermediates. The diagram, based on theoretical data, showcases a region of low energy in the acidic domain (pH 0 to 2) within a potential window of 1 to 2 V. This region highlights the optimal conditions for observing good catalytic performance and stability, particularly for intermediate Oxygen Evolution Reaction (OER) species such as *O, *OH, *OOH, *OH*O, and *OO*.

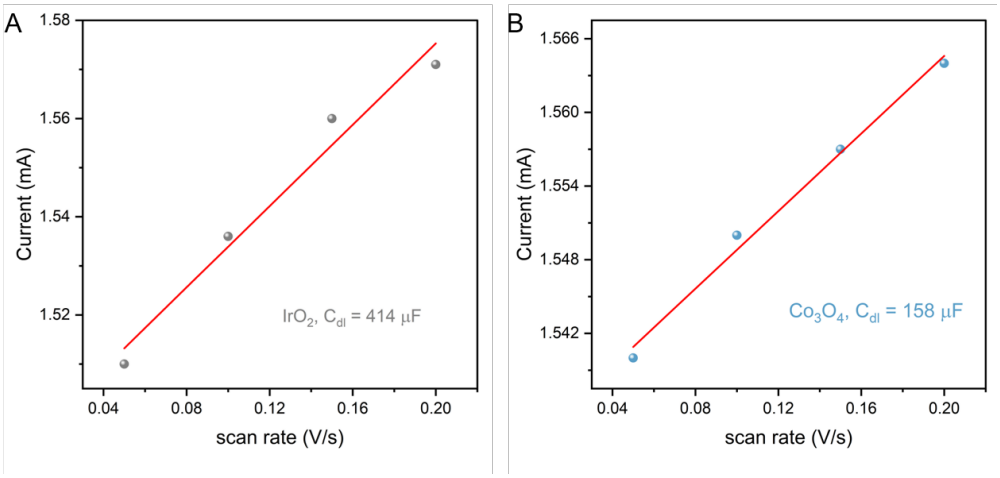

Fig. S50. Double layer capacitance (C_{dl}) of commercial (A) IrO_2 and (B) Co_3O_4.

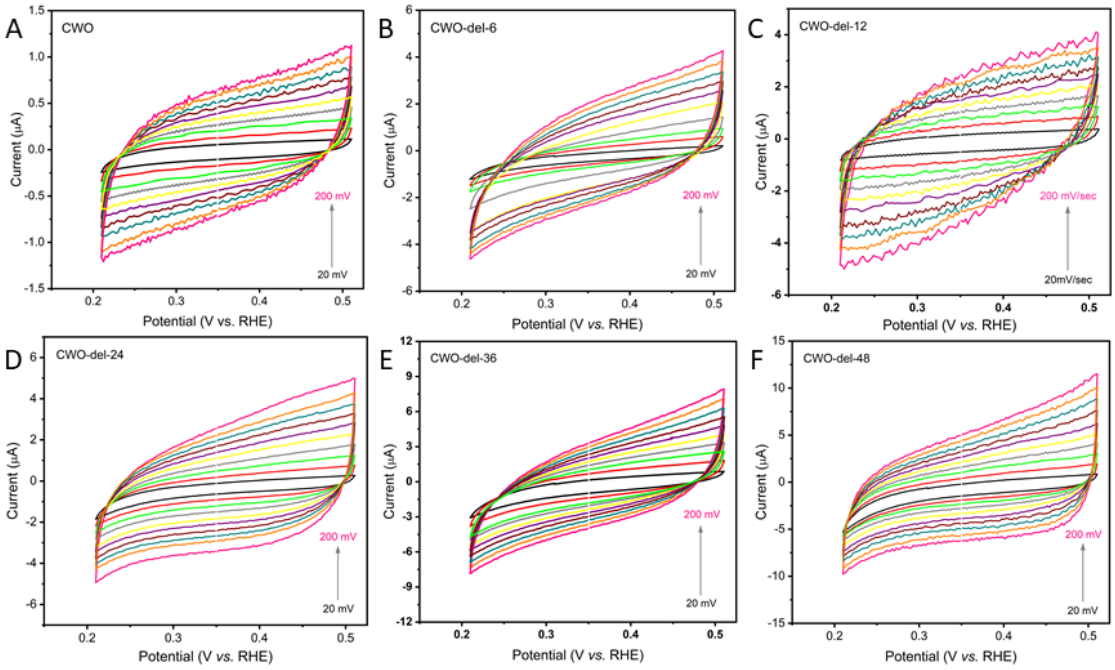

Fig. S51. Double-layer capacitance measurements. CV curves of (A) CWO, (B) CWO–del–6, (C) CWO–del–12, (D) CWO–del–24, (E) CWO–del–36 and (F) CWO–del–48 catalysts in the non-Faradic regions at 20 to 200 $mV \cdot s^{-1}$ scan rate in 0.5 M H_2SO_4, respectively. The current at 0.35 V *vs.* RHE was taken to calculate double-layer capacitance and subsequent electrochemical active surface area of the catalysts.

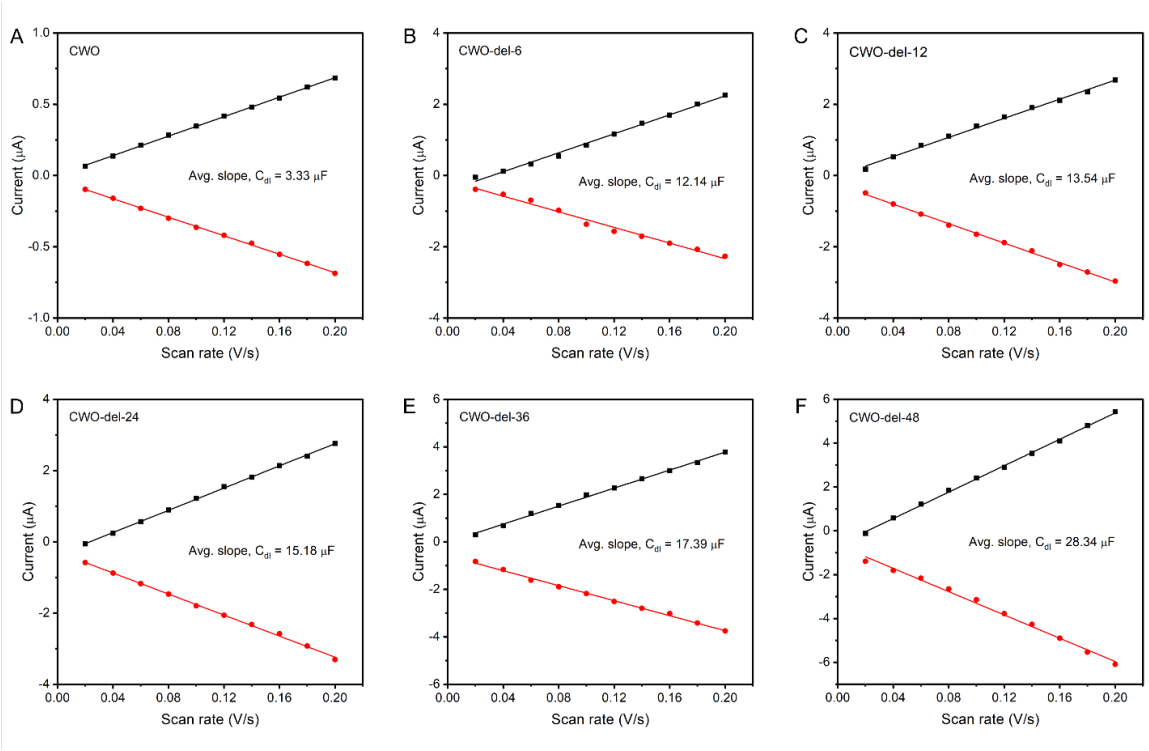

Fig. S52. Double-layer capacitance (C_{dl}) of the catalysts. Current *vs.* scan rate in both anodic and cathodic parts of (A) CWO, (B) CWO–del–6, (C) CWO–del–12, (D) CWO–del–24, (E) CWO–del–36 and (F) CWO–del–48 catalysts were plotted, respectively. C_{dl} is the average of anodic and cathodic slope of the catalysts, respectively. The double-layer capacitance increases almost 8.5 times in CWO–del–48 catalyst when compared to CWO.

Table S18. Double-layer capacitance (C_{dl}) and ECSA calculation of the catalysts. The specific capacitance (C_s) = 35 µF·cm^{-2} is considered (*61*).

Material	Anodic slope	Cathodic slope	C_{dl} (µF·cm^{-2})	ECSA (cm^2)
CWO	3.42	3.245	3.33	0.095
CWO–del–6	13.31	10.97	12.14	0.347
CWO–del–12	13.41	13.67	13.54	0.386
CWO–del–24	15.6	14.76	15.18	0.434
CWO–del–36	18.96	15.81	17.39	0.497
CWO–del–48	30.127	26.55	28.34	0.81

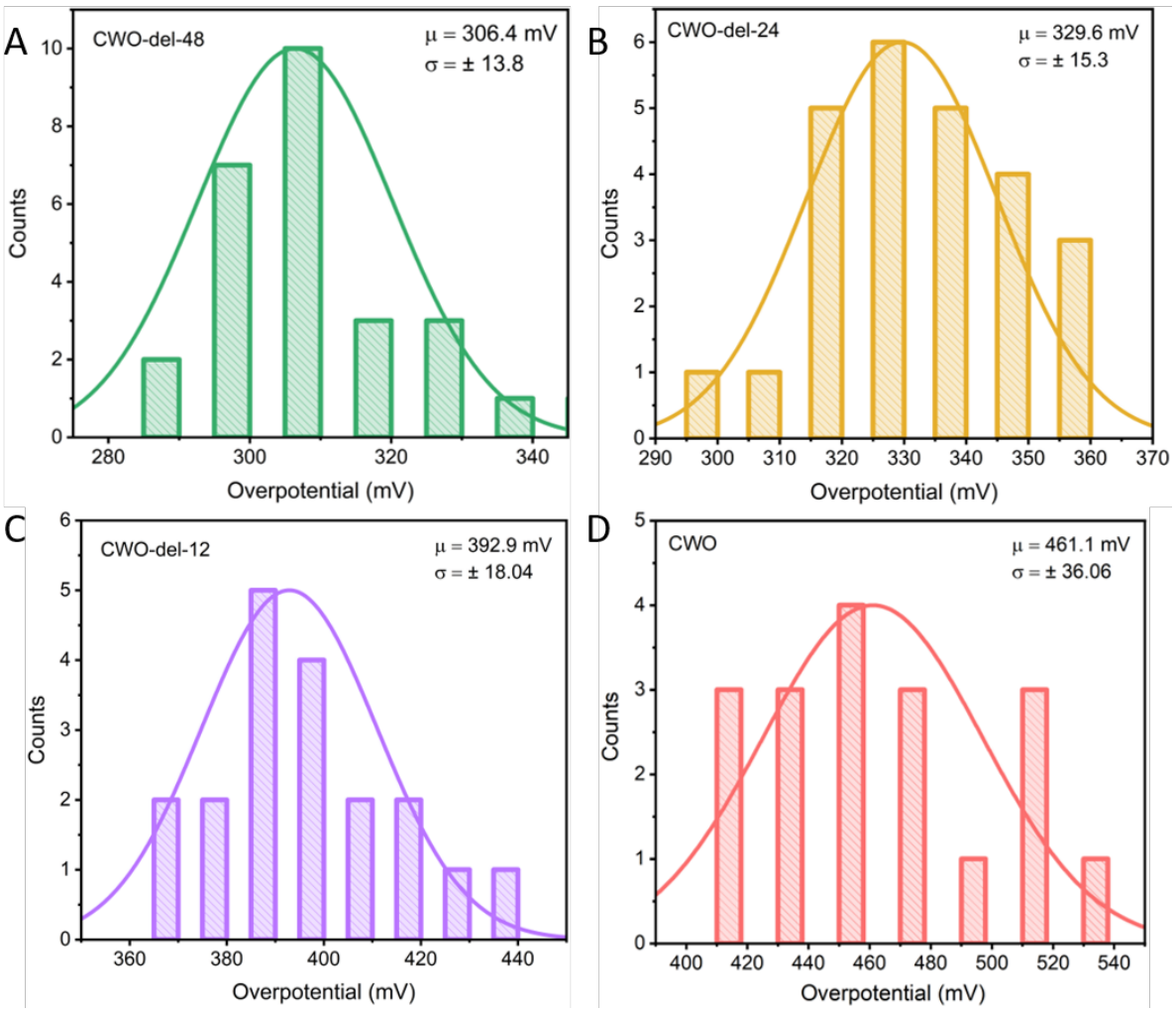

Fig. S53. Reproducibility of OER performance. The histograms (A), (B), (C) and (D) exhibit the repeatability and the distribution of OER overpotential at 10 $mA \cdot cm^{-2}$ current density of CWO–del–48, CWO–del–24, CWO–del–12 and CWO, respectively. The overpotential average and standard deviation are also shown. CWO–del–48 has an average of 306.4 mV of overpotential, with a ±13.8 mV deviation. The number of tests performed to obtain the histograms (A), (B), (C) and (D) are 31, 25, 20 and 18 different samples, respectively.

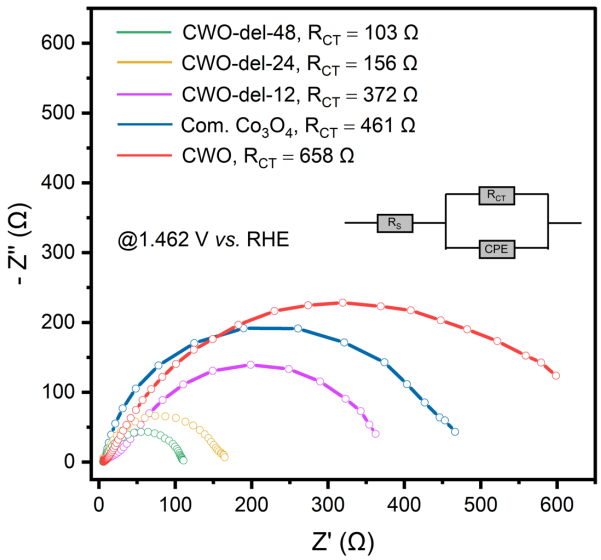

Fig. S54. EIS analysis of the catalysts. The solution resistance of the electrolyte and charge transfer resistance (R_{CT}) of the catalysts were studied by performing EIS at 1.462 V *vs.* RHE. CWO shows a slightly higher R_{CT}-value than commercial Co_3O_4. The R_{CT}-value decrease from CWO–del–12 to CWO–del–48 reflects the superiority of CWO–del–48 as an OER catalyst. The representative EIS circuit is shown in the inset (R_s, R_{CT} and CPE are solution resistance, charge transfer resistance and constant phase element resistance respectively).

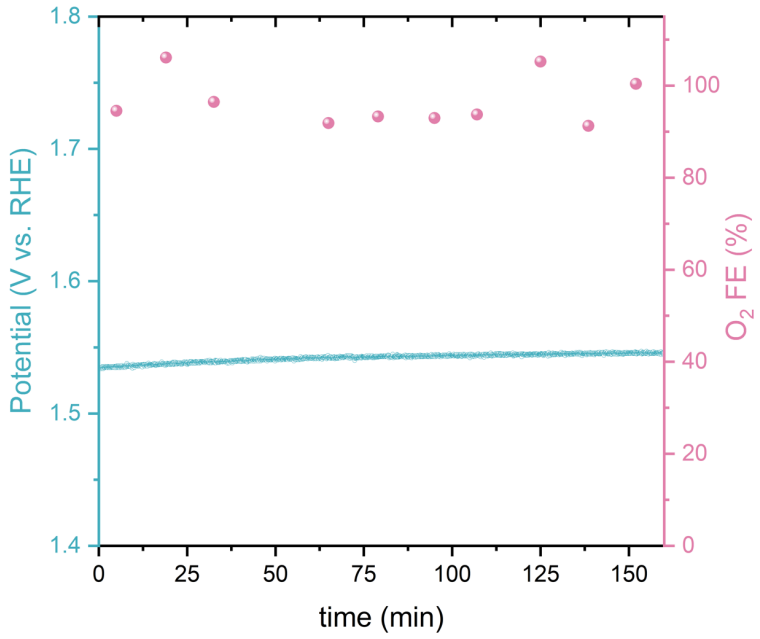

Fig. S55. O_2 Faradic efficiency measurements of CWO–del–48. The O_2 evolved was quantified using gas-chromatography in an H-cell fed with Ar, 0.5 M H_2SO_4 electrolyte, and fixed 10 mA·cm^{-2} current density over 160 min, resulting in a FE of 96.6 ± 5.2%.

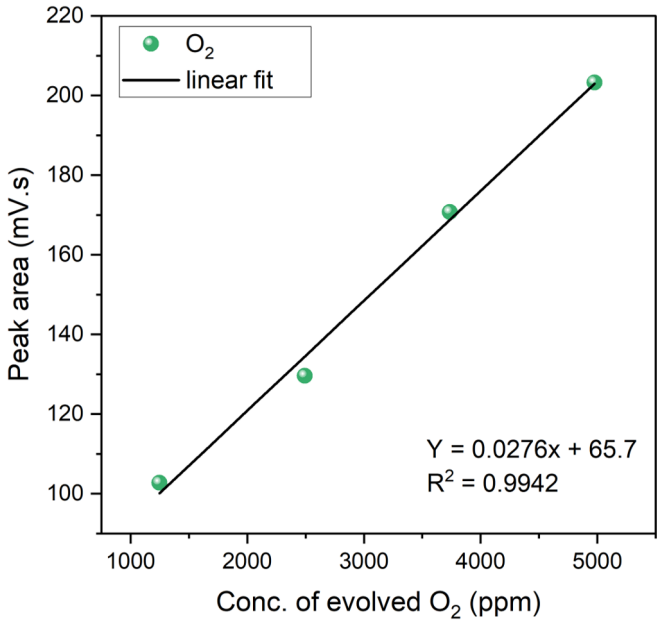

Fig. S56. Calibration curve for O_2 %FE measurements. The points in the curve correspond to different dilutions of O_2 in an Ar matrix.

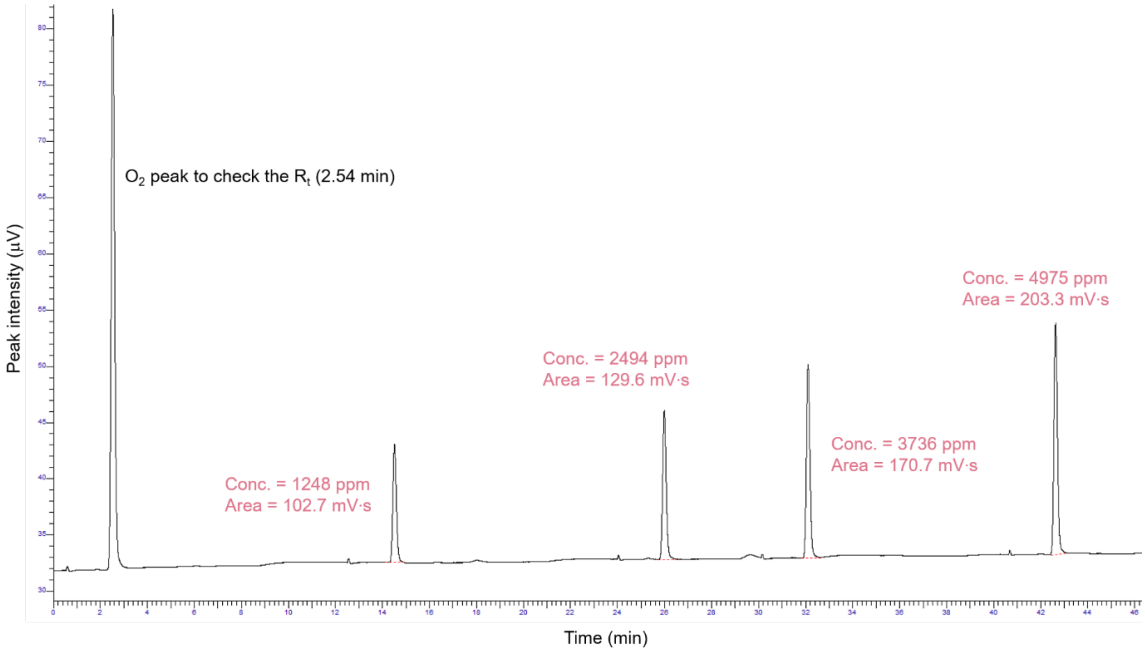

Fig. S57. Gas chromatogram for O_2 calibration corresponding to Fig S56.

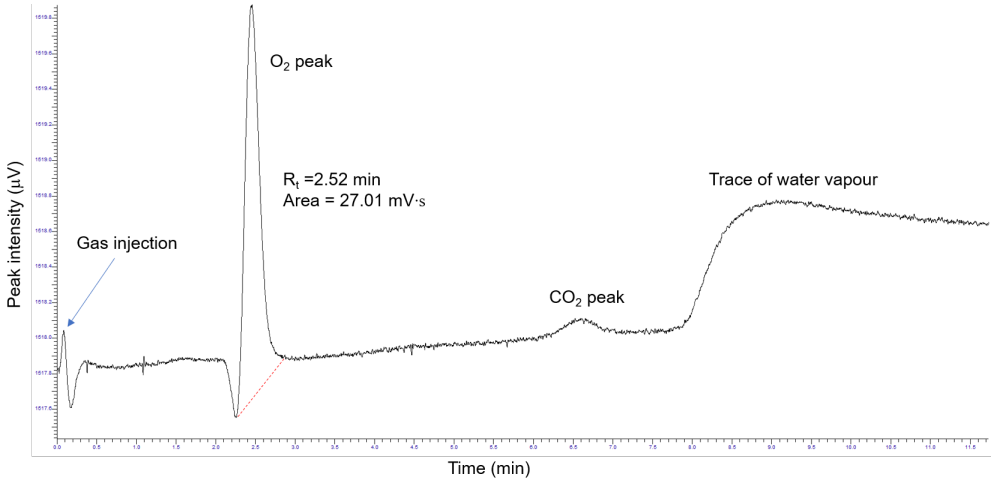

Fig. S58. Gas chromatogram corresponding O_2 from the background (manual injection from H-cell head-space fed with Ar).

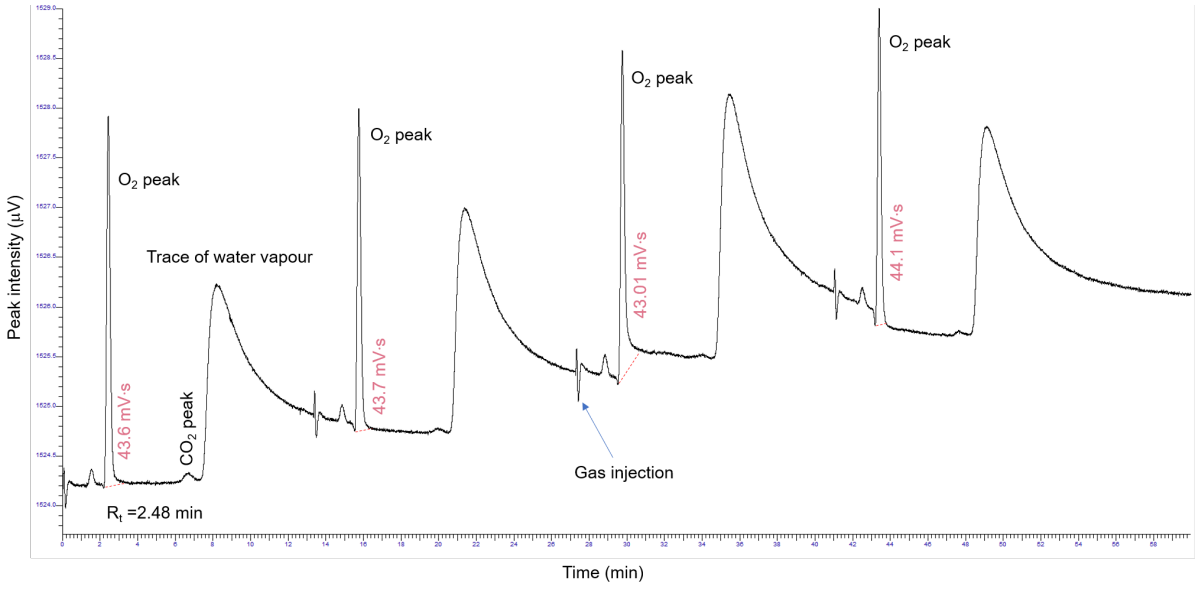

Fig. S59. Gas chromatogram for O_2 from CWO–del–48 during chronopotentiometry study at 10 mA·cm^{-2} of current density.

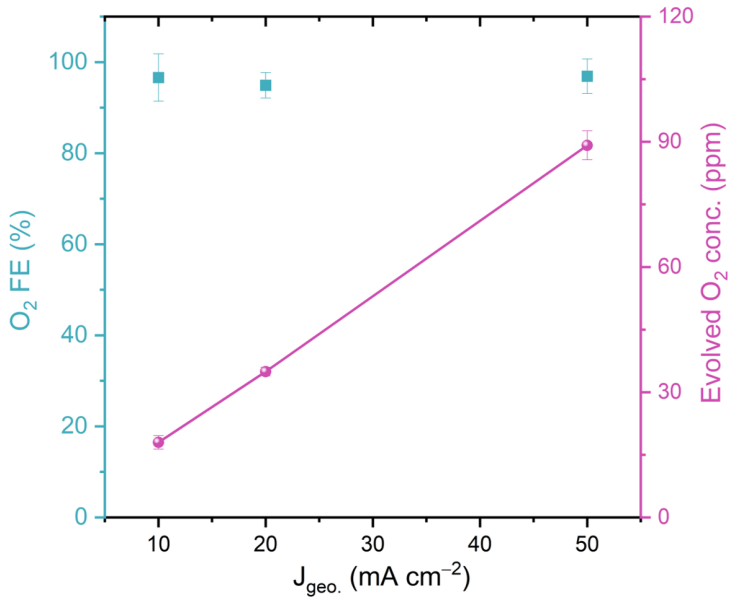

Fig. S60. Correlation of %FE of O_2 and evolved O_2 concentration with different current densities for CWO-del-48. The % FE of O_2 remains similar, 96.6 ± 5.2%, 94.9 ± 2.8% and, 96.9 ± 3.8%, at 10, 20 and 50 mA·cm^{-2} current density, respectively. The evolved O_2 concentration increases linearly with current density.

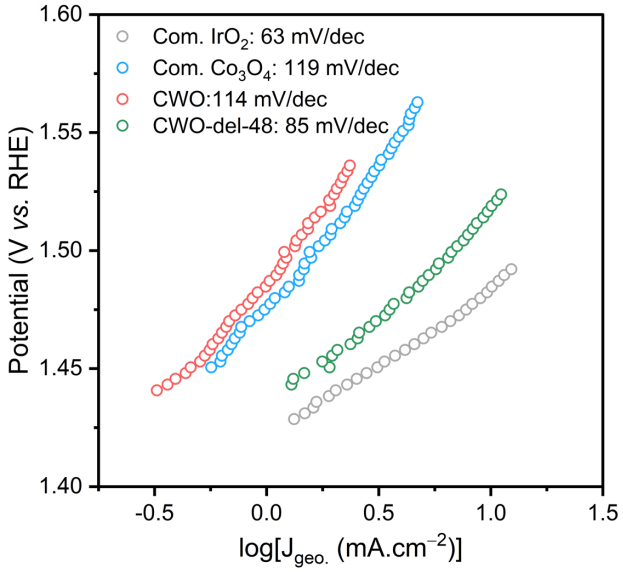

Fig. S61. Tafel slopes study of the catalysts. CWO–del–48 has 85 mV·dec^{-1} of Tafel slope, which is smaller than commercial Co_3O_4 (119 mV·dec^{-1}) and pristine CWO (114 mV·dec^{-1}). Tafel slope analysis suggest the faster OER kinetics of CWO–del–48 than CWO and commercial Co_3O_4. The Tafel slope of commercial IrO_2 (63 mV·dec^{-1}) was analysed as the reference OER catalyst.

To verify the structure of the membrane and the change in crystal structure of the catalyst, we conducted XRD experiments before and after 12 h of OER. We studied the XRD of the pre- and post-mortem Nafion 117 membrane (Fig. S62, A). After OER, the crystallinity of the membrane remains similar, with no new XRD peaks emerging. This supports the durability of the membrane and the lack of ion/catalyst deposition within the membrane during the OER.

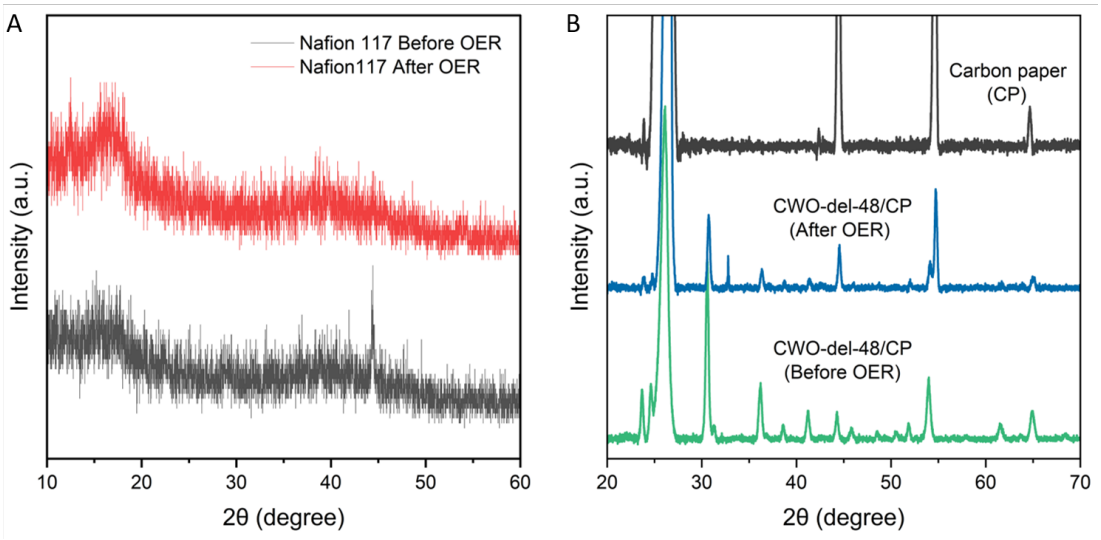

Fig. S62. XRD pre- and post-mortem of membrane and catalyst. XRD patterns of the (A) Nafion 117 membrane and (B) CWO–del–48 catalyst coated on carbon paper (CP) before and after 12 h of OER at 10 $mA \cdot cm^{-2}$.

The crystal structure of CWO–del–48 remained similar, with emerging peaks attributed to carbon paper and CoO_x after oxidation (Fig. S61B). The XRD peaks of CWO–del–48/CP after OER, shifts at slightly higher 2θ values. The two new peaks emerged in XRD after OER correspond to carbon paper at 49° and 65°, along with carbon´s most intense peak at 26°. These peaks are observed in CWO–del–48/CP before OER, but in relatively lower intensity. Before and after OER, CWO–del–48 show high degree of crystallinity.

HAADF-STEM images before and after OER suggest that the morphology of the catalyst remains broadly similar (Fig. S23–24, S63).

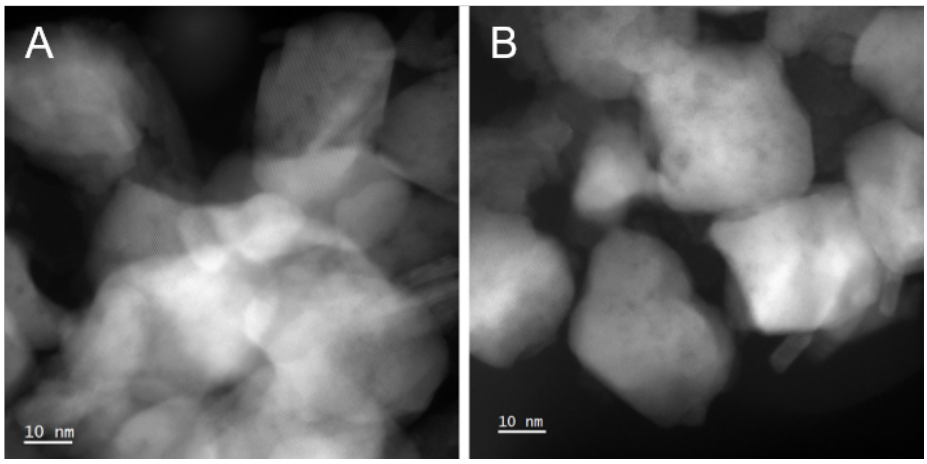

Fig. S63. STEM images of CWO–del–48 after OER. Two (A and B) high magnification HAADF-STEM images of the CWO–del–48 catalyst after 12 h of OER at 10 mA·cm^{-2}.

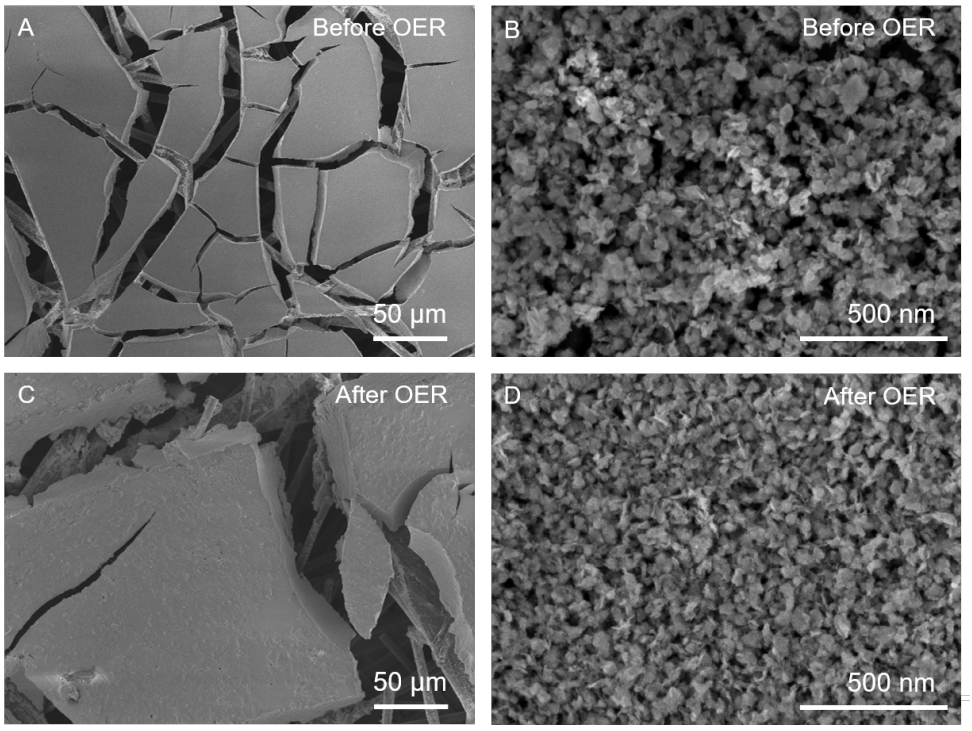

Fig. S64. Microstructure study of CWO−del−48 before and after OER. (A) 500× and (B) 100 k× magnified SEM images of CWO–del–48 spray coated on carbon paper, before reaction. (C) and (D) show the morphology of the same electrodes after 24 h of CP test at 10 mA·cm^{-2} current density. The surface of the electrodes (A *vs*. C) changes, reflecting the formation and escape of O_2 bubbles. Higher magnification images (B *vs*. D) reveal an overall similar morphology before and after reaction.

Table S19. EDS-SEM atomic % of Co, W and O before and after 24 h of chronopotentiometry at 10 mA·cm^{-2} of current density using CWO–del–48 on carbon paper electrode. The atomic % of each element is the average of 12 different sample positions.

Condition	Co (At. %)	W (At. %)	O (At. %)
Before OER	23.40 ± 4.24	12.48 ± 0.99	51.20 ± 3.52
After OER	19.60 ± 3.20	12.65 ± 1.10	58.93 ± 5.33

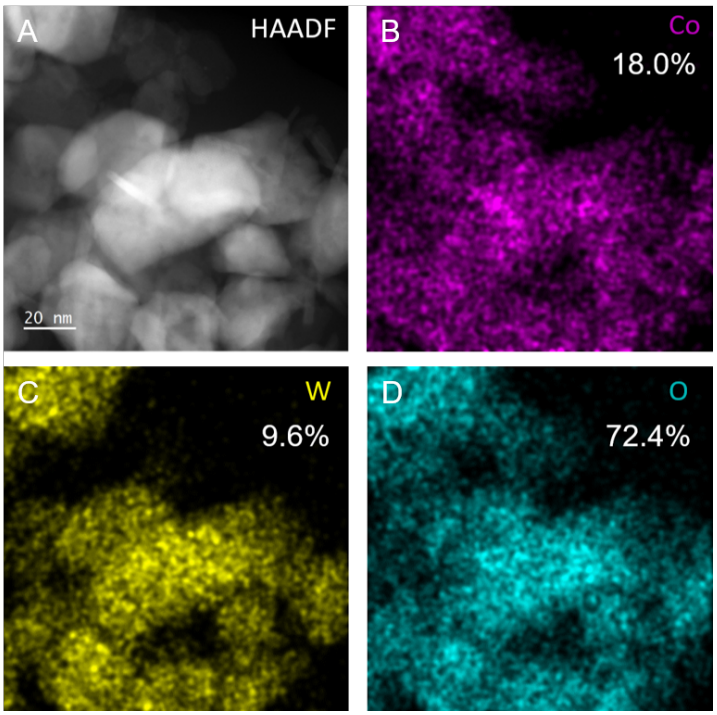

Fig. S65. HAADF-STEM of CWO–del–48 after OER. The HAADF STEM (A) and corresponding STEM-EDS experiments performed in the region revealing an approximate general composition of (B) 18 at.% of Co, (C) 9.6 at.% W and (D) 72.4 at.% of O. The results are similar to those from the CWO–del–48 pre-mortem samples (Fig. S28, D).

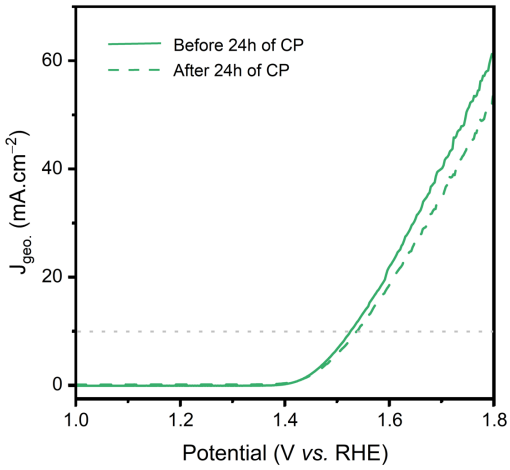

Fig. S66. Durability test through LSV. Comparison of OER polarisation curves of CWO–del–48 catalysts before and after 24 h of chronopotentiometry (CP) test. Electrolyte = 0.5 M H_2SO_4 solution and catalyst loading ~1.4 mg·cm^{-2} over carbon paper. No significant change is observed in the overpotential values at 10 mA·cm^{-2}, in the LSVs of the catalyst before and after 24 h of CP.

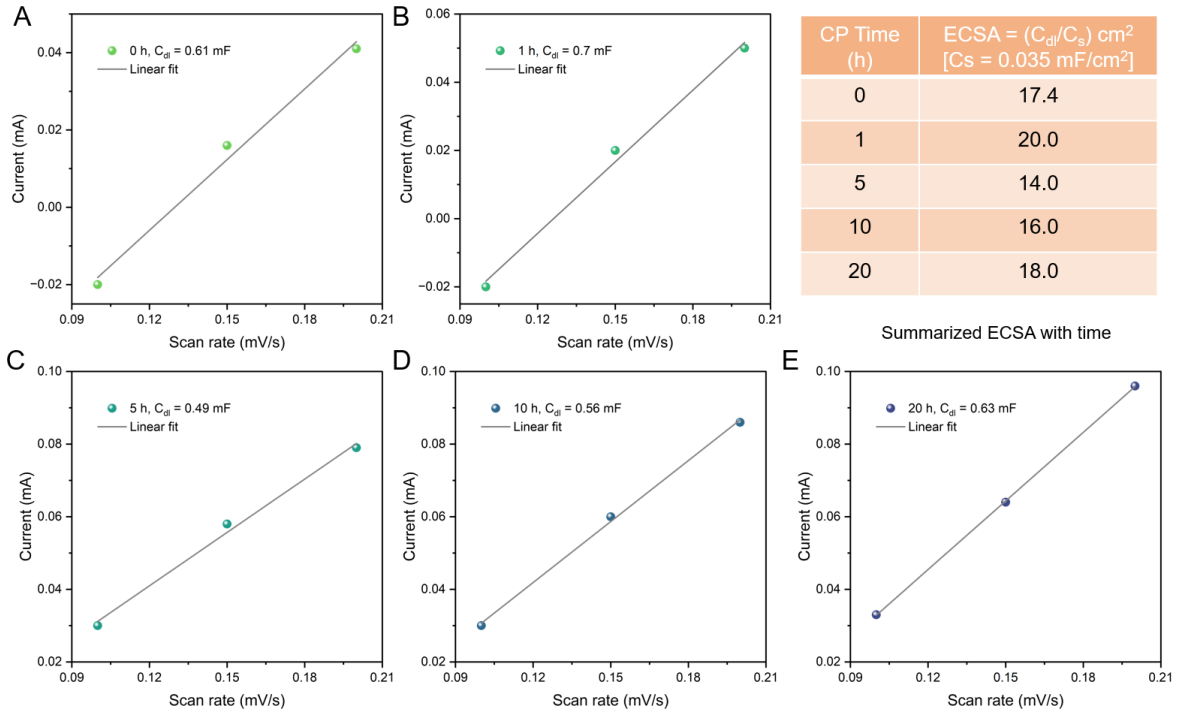

CP Time (h)	ECSA = (C_{dl}/C_s) cm^2 [Cs = 0.035 mF/cm^2]
0	17.4
1	20.0
5	14.0
10	16.0
20	18.0

Summarized ECSA with time

Fig. S67. Variation of ECSA during OER. C_{dl} of CWO–del–48 (coated on carbon paper, geometrical surface area = 1 cm^2) presented after various OER time intervals of (A) 0, (B) 1, (C) 5, (D) 10 h and (E) 20 h, during constant current density of 10 mA·cm^{-2} in a 0.5 M H_2SO_4, for different scan rates. The inset table provides the calculated ECSA (considering a specific capacitance, Cs = 0.035 mF·cm^{-2}).

The C_{dl} and ECSA (Fig. S67, A-E and inset table) of CWO–del–48 reveals minor fluctuations around the initial value of 17.43 cm^2, compatible with variations in the wetting of the active layer, bubbles *etc.* This observation suggests that the ECSA of the catalyst remains largely unchanged throughout the duration of the test.

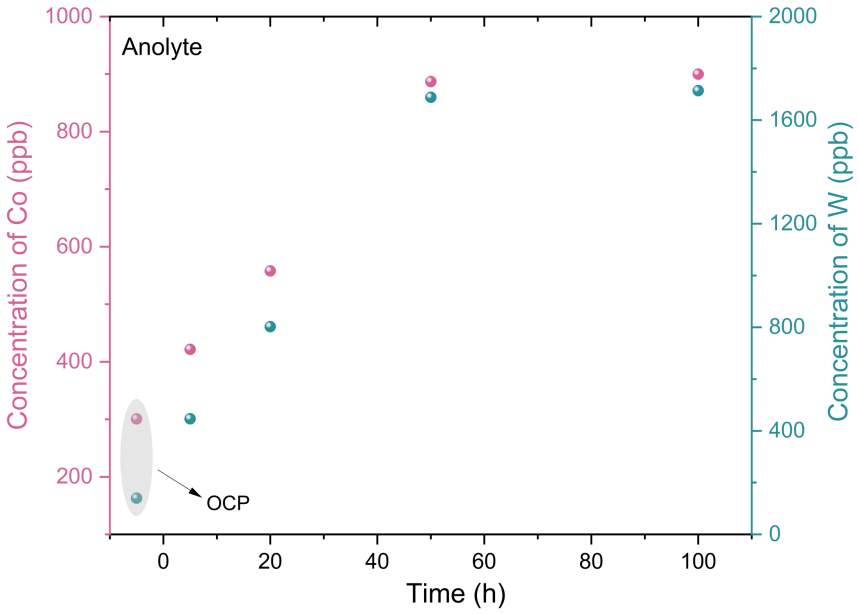

Fig. S68. Electrochemical stability. Elemental leaching assessed by ICP-MS for the anolyte of H-cell after a continuous test at 10 $mA \cdot cm^{-2}$ for 100 h before keeping the system at OCP for 5 h (anode catalyst: CWO–del–48, loading 1.5 $mg \cdot cm^{-2}$; cathode: graphite rod; membrane: Nafion 117, electrolyte volume is 40 mL).

The concentration of leached Co and W (Fig. S68) in the electrolyte follows an initial linear increase over the first 50 h, ranging from 300 to 900 ppb. Subsequently, a saturation point is reached, maintaining a stable concentration at ~900 ppb. This behaviour suggests the high stability of CWO–del–48 throughout the tested duration. After OCP (5 h) and 100 h of OER stability test, the concentration of Co in the electrolyte = 3.06 ppm = (3.06 × 0.998) mg/L = 3.05 mg/L. Thus, the amount of Co in total 40 mL of the electrolyte $\approx \left(3.05 \times \frac{40}{1000}\right)$ mg = 0.122 mg.

To assess the possibility of Co migration to the catholyte chamber through the Nafion membrane, we checked Co and W concentration in the catholyte chamber of the H-cell (Fig. S69). The concentration of Co and W in the catholyte was determined to be negligible, confirming the selectivity of the Nafion 117 membrane towards Co and W species.

Additionally, we carried out XPS analysis of the Nafion membrane (Fig. S70, Table S20) and graphite rod (counter electrode, Fig. S71) after 100 h of OER stability test at 10 mA·cm^{-2} of current density. For both the Nafion membrane and the graphite rod, no Co and W could be quantified after the OER.

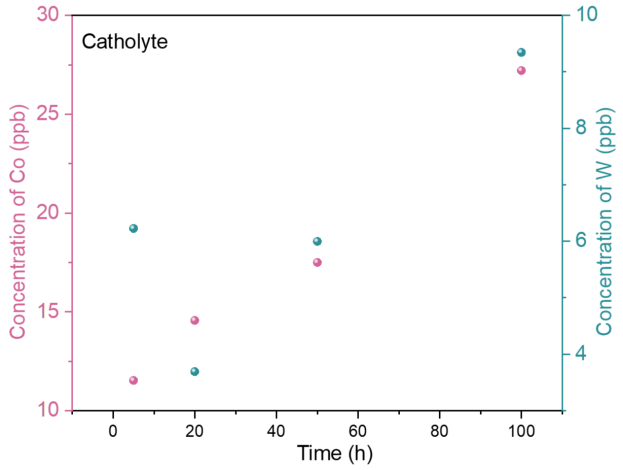

Fig. S69. Electrochemical stability. Elemental leaching assessed by ICP-MS for the catholyte of H-cell after a continuous test at 10 mA·cm^{-2} for 50 h (anode catalyst: CWO–del–48, 1.5 mg·cm^{-2}, cathode: graphite rod; membrane: Nafion 117).

Potential role of Co ions and membrane: To assess the durability of both CWO–del–48 and Nafion membrane in a H-cell, we performed XPS analysis of the Nafion 117 membrane. We did not find any traces of Co ions on the Nafion membrane (Fig. S70, Table S20), consistent with XRD studies (Fig. S62).

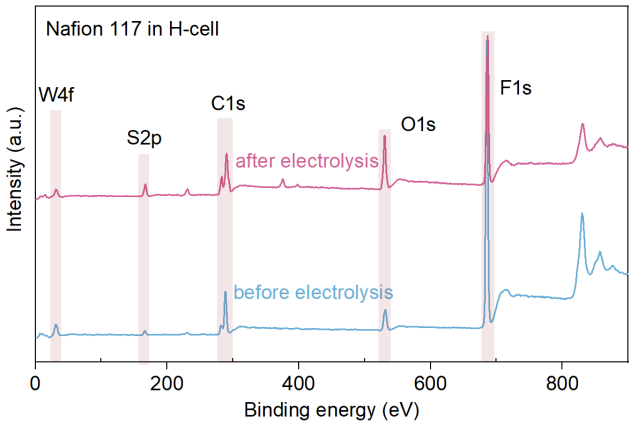

Fig. S70. XPS survey of Nafion 117 membrane used in H-cell. The membrane was collected after 100 h of stability test of CWO–del–48 in 0.5 H_2SO_4 in a H-cell at 10 mA·cm^{-2}.

Table S20. Chemical composition of Nafion 117 membrane before and after 100 h chronoamperometry at 10 mA·cm^{-2} in an H-cell (0.5 H_2SO_4 electrolyte). [n.d.: not detected]

Condition	Pt (At. %)	F (At. %)	Co (At. %)	C (At. %)	W (At. %)	S (At. %)	O (At. %)
Nafion 117 before	n.d.	68.86	n.d.	16.86	6.26	1.34	6.72
Nafion 117 after	n.d.	40.49	n.d.	26.58	5.74	4.54	22.65

Additionally, to check the possible deposition of Co or W-species on the graphite counter electrode, we carried out XPS analysis. We did not detect quantifiable traces of these elements.

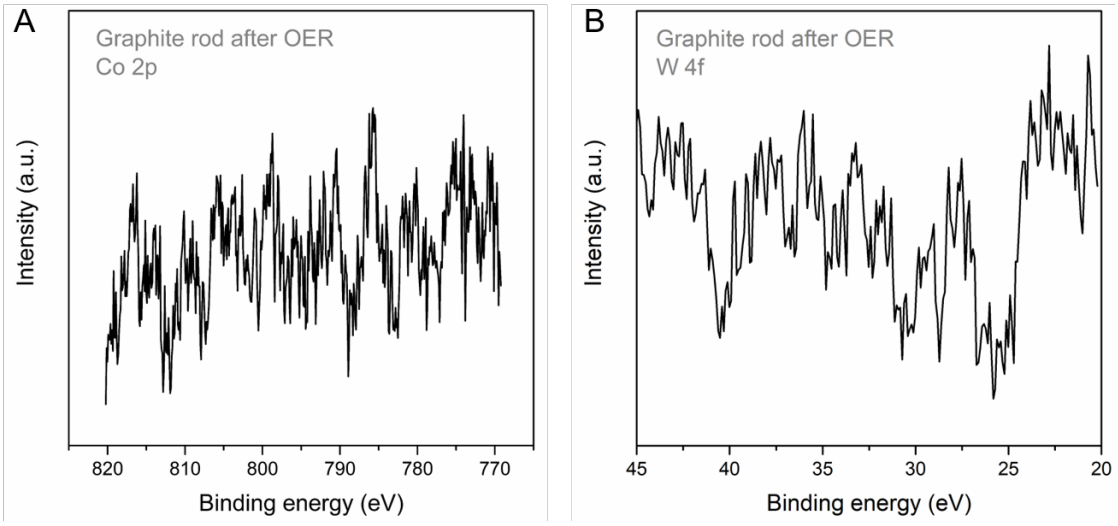

Fig. S71. XPS analysis of graphite rod in catholyte chamber after OER. The high resolution XPS of (A) Co 2p and (B) W 4f, display no detectable amount of Co and W, after the continuous chronopotentiometry for 100 h in 0.5 H_2SO_4 at 10 mA·cm^{-2} in H-cell (anode catalyst: CWO–del–48, 1.5 mg·cm^{-2} loading, cathode: graphite rod; membrane: Nafion 117).

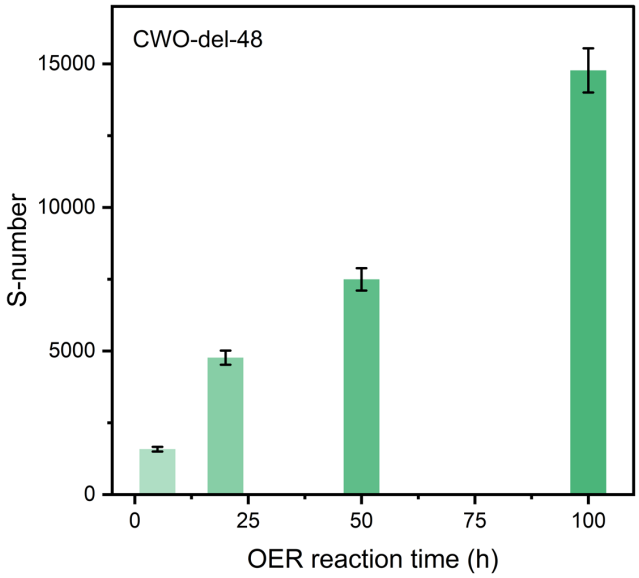

Fig. S72. S-number of CWO–del–48. The OER reaction time-dependent S-numbers were calculated. After 100 h of CP, the catalyst obtained the highest S-number. The increase in S-number over OER time demonstrates the durability of the catalyst. The values are comparable with state-of-the-art PGM-free catalysts (see **Table S22**).

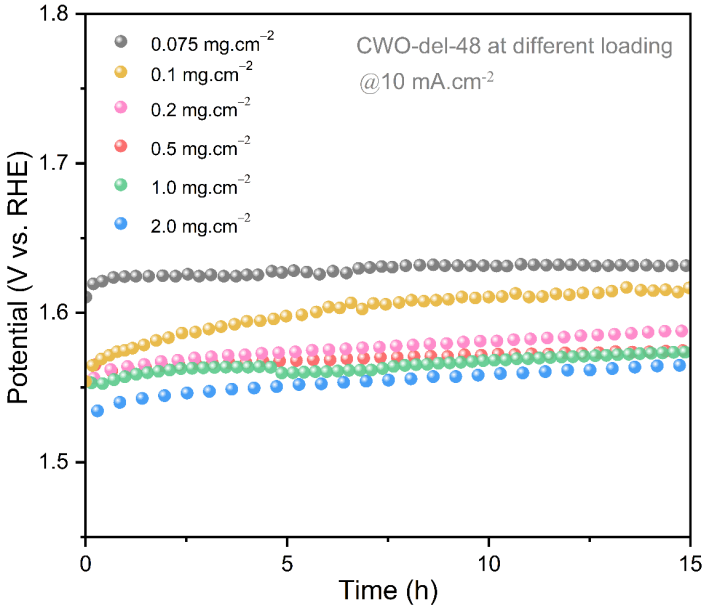

Fig. S73. OER performance of CWO–del–48 with different loadings. Chronopotentiometry tests of CWO–del–48 with different mass loading of 0.075, 0.1, 0.2, 0.5, 1.0 and, 2.0 mg·cm^{-2} at 10 mA·cm^{-2} during 15 h tests showing similar stability trends.

To assess the potential role of dissolved Co ions in the overall anode catalyst stability (*i.e.*, their role in surface reconstruction or mediating OER through homogeneous catalysis), we sought to add 2,2′-bipyridine (bpy) into the electrolyte as a Co ion scavenger. If any dissolved Co ions played an active role during electrolysis, they would be trapped by bpy forming a chelated complex $[Co(bpy)_3]^{2/3+}$ due to the strong π-acceptance nature of the ligand *(60)*; leading to a decrease the OER activity should dissolved Co ions play a significant role in terms of activity and stability.

To do so, 0.1 mM of bpy was continuously introduced to the solution at an interval of 4 h during 20 h of chronopotentiometry at a current density of 10 mA·cm^{-2}. The chronopotentiometry (Fig. S74, B) and polarization traces (Fig. S74, C) of CWO–del–48 including bpy (0.5 mM) capture do not show noticeable differences. This indicates that there is either no significant amount of dissolved Co ions, or that their presence would not result in a noticeable impact on the overall performance.

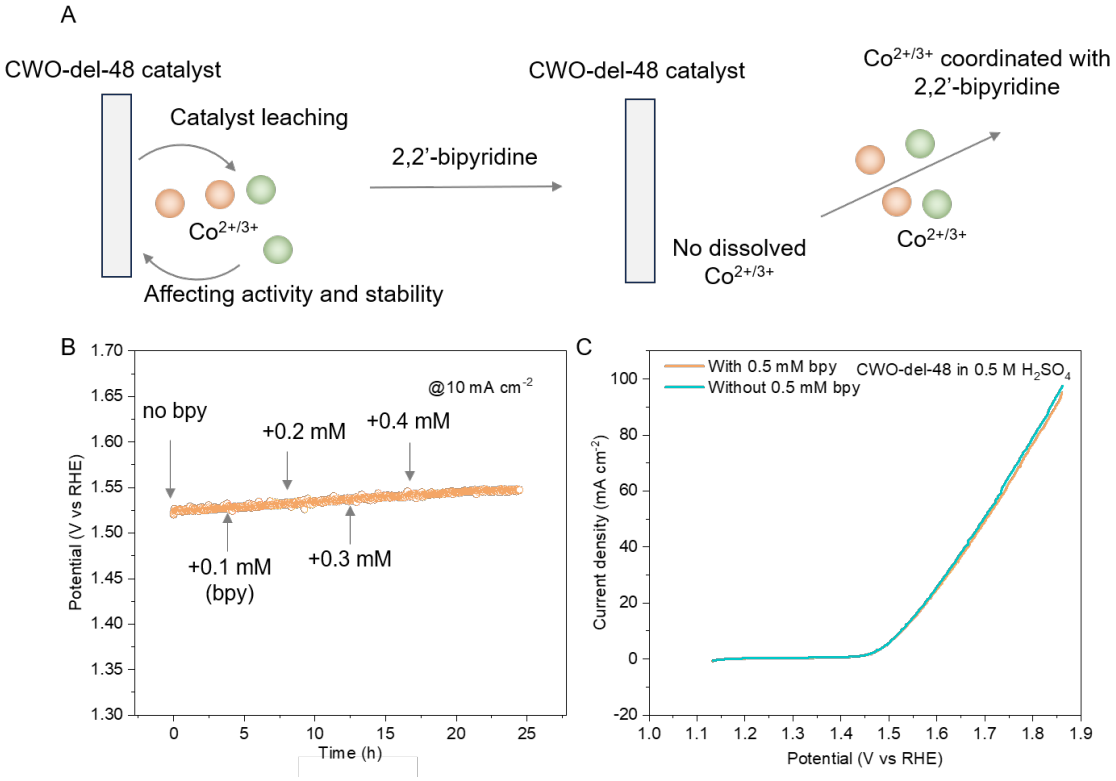

Fig. S74. Assessing the potential role of dissolved Co ions on catalyst OER performance. (A) Illustration of the strategy to remove the dissolved cobalt ions by 2,2′-bipyridine (bpy), a chelating agent to make complex with cobalt ions. (B) Chronopotentiometry experiment of CWO–del–48 carried out at 10 mA·cm^{-2} (at every 4 h interval, externally bpy was added with

different concentration). (C) LSV of CWO–del–48 before and after adding 0.5 mM bpy at the scan rate of 5 $mV \cdot s^{-1}$. The catalyst mass loading is 1.0 $mg \cdot cm^{-2}$. It is noteworthy that some amount of Co ions, in the ppb regime, could still remain un-chelated by 2,2′-bipyridine. (see next section for further ion-dissolution-related tests).

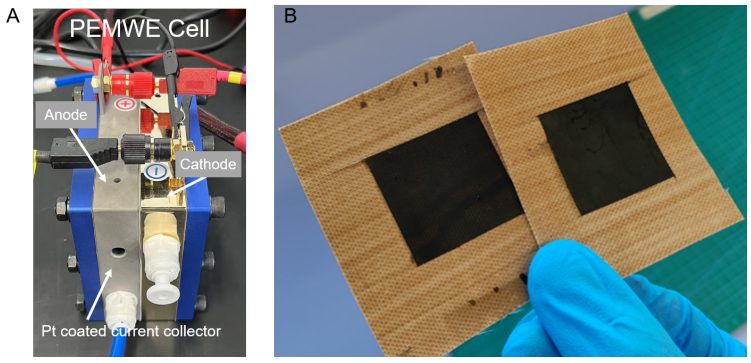

Fig. S75. PEMWE (A) A digital photograph of our PEMWE cell with Pt coating layer on anode current collector and, (B) CWO–del–48 catalyst spray-coated on PTFE (mass loading ~ 4 $mg \cdot cm^{-2}$).

Ion-leaching studies in PEMWE

Additionally, we conducted a comparison of elemental leaching for CWO–del–48 in a PEMWE operating at 1 $A \cdot cm^{-2}$ with a loading of ~4 $mg \cdot cm^{-2}$ (Fig. S76), after 12 h of conditioning at 1.7 V cell potential.

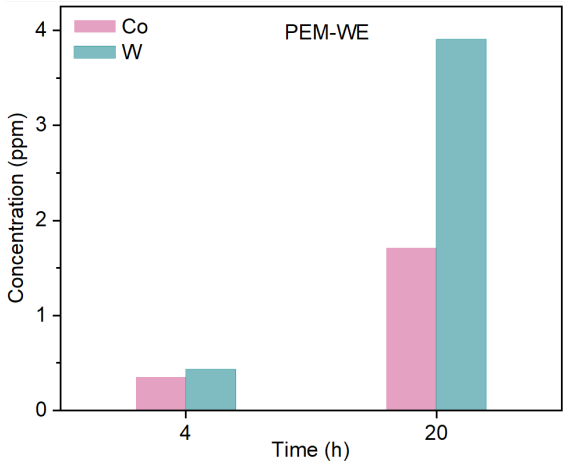

Fig. S76. ICP-OES data for PEMWE. ICP-OES studies were carried out on PEMWE over various time periods under 1 $A \cdot cm^{-2}$ operation. The concentration of Co and W leaching from the catalyst is found to be comparable to the H-cell configuration. The ICP-OES data indicates a high stability of CWO–del–48 catalysts under PEMWE operational conditions.

In the electrolyte of PEMWE, the concentrations of Co and W were ~352 ppb and ~432 ppb, respectively, after 4 h of electrolysis; which increased to ~1712 ppb and ~3906 ppb, respectively after 20 h of electrolysis.

Single pass experiment

To study the potential effect on stability of dissolved ions in the electrolyte reservoir, we assessed the electrochemical performance of CWO–del–48 under single pass electrolyte flow conditions (as opposed to standard recirculating operation) during chronopotentiometry at 0.2 $A \cdot cm^{-2}$ in PEMWE at 80°C (Fig. S77, A). The membrane electrode assemblies (MEAs) were initially conditioned by keeping the cell at a constant 0.2 $A \cdot cm^{-2}$ of current density for ~10 h, at 80°C under electrolyte (milli-Q water) recirculation. Conditioning in PEMWEs, including processes like membrane humidification, is primarily aimed to enhance the membrane's proton conductivity and operational durability. High operational temperatures influence water uptake and membrane stress, affecting hydrogen crossover rates and potentially accelerating membrane degradation *(61,62)*.

After the initial conditioning step, we refilled the reservoir tank with fresh electrolyte, thus flushing away all dissolved Co ions in the reservoir accumulated during the conditioning process. Afterwards, we started the single pass experiment in PEMWE at 0.2 $A \cdot cm^{-2}$ and 80°C under an electrolyte flow rate of 10 $mL \cdot min^{-1}$. Fresh electrolyte was continuously replenished with milli-Q water (Fig. S77).

During single-pass operation, CWO–del–48 exhibited stable performance. An initial transient voltage with an amplitude of ca. 10 mV, gradually returning to its original voltage level of 1.53 V was observed. This behaviour is similar to the one observed during electrolyte replenishment under recirculation. Fluctuations in voltage might arise due to a combination of temperature gradients during electrolyte replenishment, modifying electrolysis rates and gas dissolution, as well as catalyst ion and particulate dissolution events. Beyond the scope of this work, detailed studies of these processes and their dynamics (*e.g.*, using in-line mass spectroscopy) in different material systems could be instrumental to enable further advances in stability.

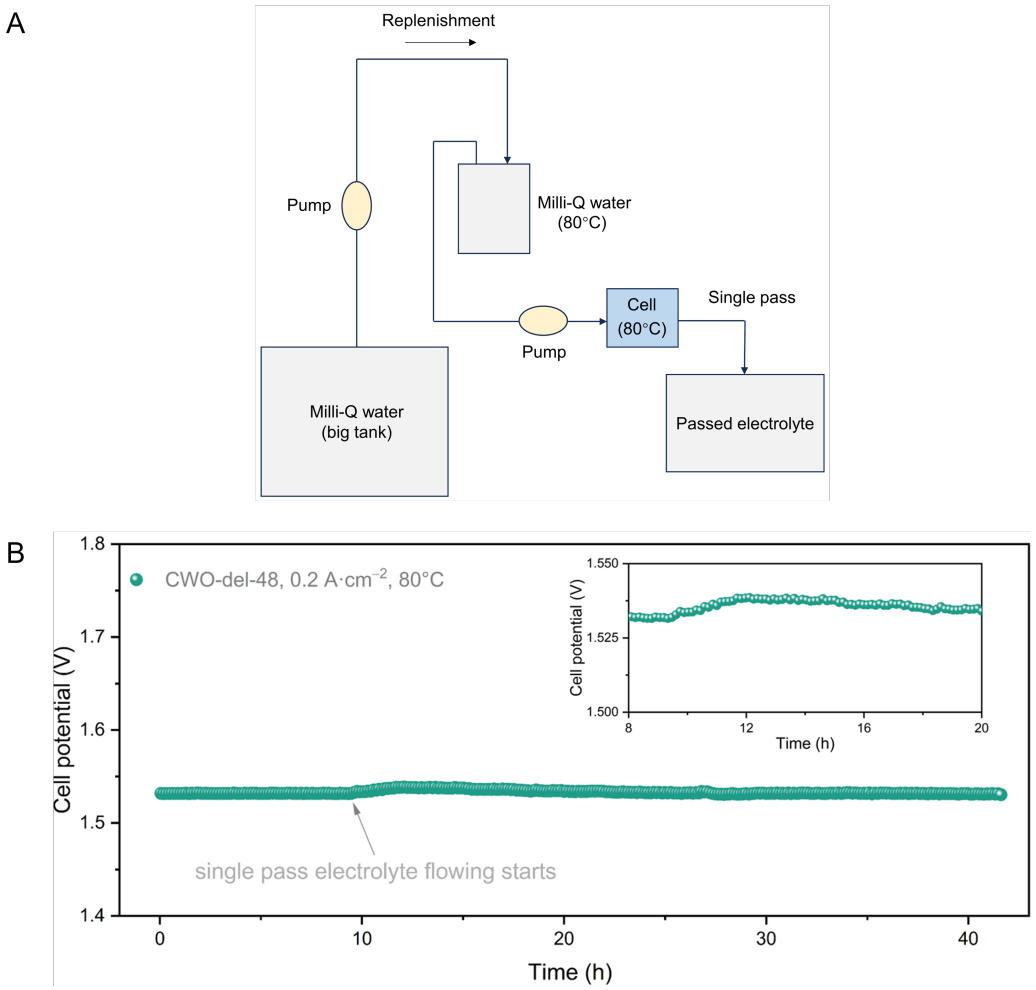

Fig. S77. CWO–del–48 PEMWE operation with single pass electrolyte flowing. (A) Schematic of the single-pass electrolyte setup during PEMWE operation. **(B)** The electrochemical performance of CWO–del–48 under single pass flowing of electrolyte (milli-Q water) at 0.2 A·cm^{-2}, 80˚C in PEMWE remains similar to standard electrolyte recirculation operation. During conditioning, other parameters were kept constant.

We flushed both sides of the CCM with milli-Q water before any post characterization. XPS analysis performed on CWO–del–48 before and after electrolysis in the PEMWE configuration reveals a negligible decrease in Co and W at. %, demonstrating the stability of CWO–del–48 (Fig. S78 and Table S21).

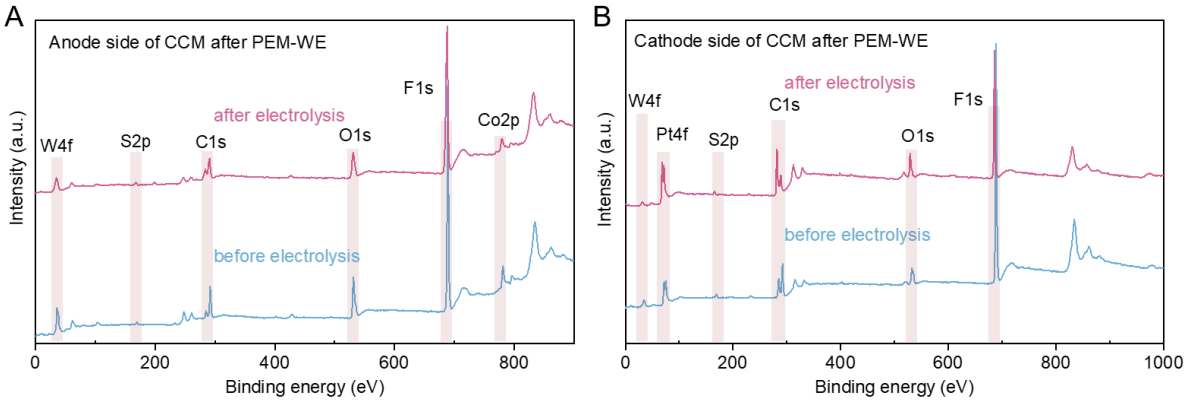

Fig. S78. XPS analysis of CCM electrode in PEMWE. To assess the stability of the CWO–del–48 and Nafion 117 membrane under PEMWE working conditions, we performed XPS analysis of both the (A) anode side (CWO–del–48) and (B) cathode side (Pt/C) of the Nafion 117 CCM electrode at 1 A·cm^{-2} for 20 h in PEMWE at 80°C. No significant change in the composition of CWO–del–48 after electrolysis in PEMWE is observed.

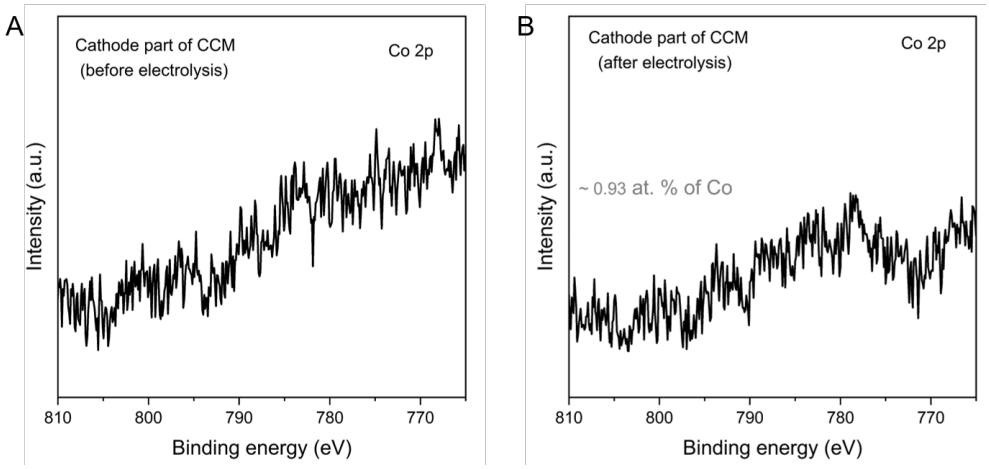

Fig. S79. High resolution XPS analysis of Co 2p. To check the Co migration through membrane to the cathode side of the CCM, we performed high-resolution Co 2p XPS at the cathode side of CCM (A) before and (B) after PEMWE operation at 1 A·cm^{-2} for 20 h. Approximately 0.93 at. % of Co (below quantification limit) was detected after PEMWE operation.

Table S21. XPS analysis for the composition of CWO–del–48 on anode side and Pt on cathode side to assess their chemical compositions before and after electrolysis at 1 A·cm^{-2} for 20 h in PEMWE (80°C) [n.d.: not detected].

Condition	Pt (At. %)	F (At. %)	Co (At. %)	C (At. %)	W (At. %)	S (At. %)	O (At. %)
Cathode (Pt/C) before	15.11	56.21	n.d.	16.57	4.56	1.41	6.06
Cathode (Pt/C) after	28.80	34.76	0.93	34.76	9.03	1.3	23.56
Anode (CWO-del-48) before	n.d.	51.53	7.95	11.12	13.52	0.66	15.23
Anode (CWO-del-48) after	n.d.	54.97	5.03	15.03	10.24	1.41	13.32

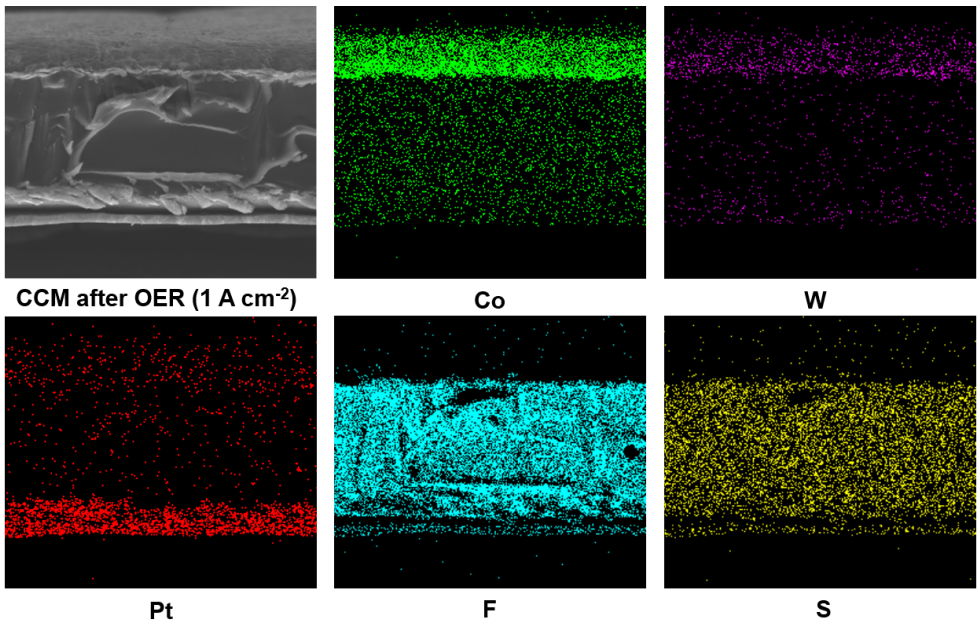

Fig. S80. SEM micrograph and EDS mapping of CWO–del–48 after PEMWE operation. Cross sectional SEM image and the corresponding EDS elemental mapping (Co, W, Pt, F, S) of CWO–del–48 after 1 A·cm^{-2} for 20 h.

SEM cross-sectional view of the CCM electrode after reaction reveals distinct features, prominently displaying the surface catalyst and the different layers of the CCM. The distribution of Co and W on the anode, Pt on the cathode, and F and S in the film, appears uniformly consistent.

Both XPS (Fig. S79, Table S21) and cross-sectional SEM-EDS (Fig. S80, S81) reveal a negligible amount of Co migration from anode to cathode side through the Nafion 117 membrane of the CCM. The detected Co migration in XPS is ~0.93 at. %, which is consistent with the SEM-EDS energy spectrum (~0.79 at. %, Fig. S81).

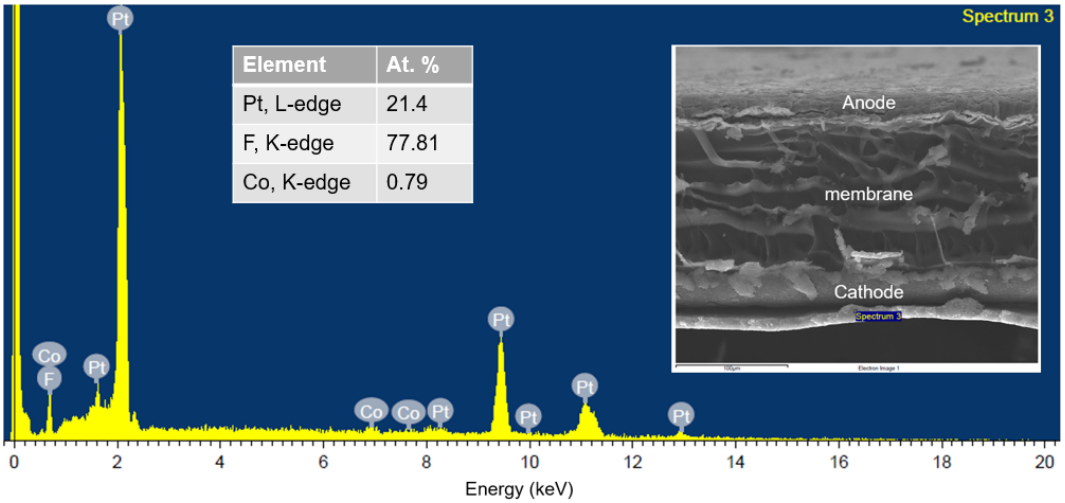

Fig. S81. SEM-EDS energy spectra of the cathode side of the CWO-del-48 CCM after PEMWE electrolysis. The energy spectra displaying high counts of Pt and F, along with 0.79 at. % of Co. Inset shows the cross-sectional SEM image of the CCM. The EDS measurement was carried from the region, labelled as spectrum 3.

Movie S1. Graphical representation of the delamination process. The pristine CWO material interacts with hydroxyl and water molecules removing some of the anions from the surface. If the process continues, then some channels can grow along the material. Colour code as in previous figures.

Explanation of Movie S1. At high pH, hydroxide ions interact with the pristine CWO surface and they can activate the anions on the surface leading to the leaching of WO_4^{2-} complexes. The vacancies are then replenished by new OH^- and H_2O molecules (as simulations show most likely two hydroxyls and two water molecules). During the process, the Cobalt atoms change colour, indicative of a transition towards more metallic behaviour before starting the OER reaction. The Bader charge is traced following the process in $|e^-|$ units.

Table S22 – Comparison of OER performance of our catalyst with state-of-art Ir- and Ru-free catalysts (IrO_2 is considered as the reference) in acidic medium (NA = not available).

Catalyst	η @ 10 mA cm^{-2} (mV)	Stability @ J ($mA \cdot cm^{-2}$) in H-cell (h)	PEMWE performance	S-number	Ref.
CWO–del–48	276	> 175 @10	1.828 $A \cdot cm^{-2}$ @2.0 V, 278 h @0.2 $A \cdot cm^{-2}$ and 250 h @1.0 $A \cdot cm^{-2}$, 80°C	14771 ± 768 @10 $mA \cdot cm^{-2}$ and 4547 ± 236 @1.0 $A \cdot cm^{-2}$	This work
CWO	472	35 @10	0.235 $A \cdot cm^{-2}$ @2.0 V, 80°C	NA	This work
IrO_2	247	> 60 @10	2.7 $A \cdot cm^{-2}$ @2.0 V, 80°C	NA	This work
Co_3O_4	372	25 @10	0.472 $A \cdot cm^{-2}$ @2.0 V, 80°C	NA	This work
$Co_{3-x}Ba_xO_4$	278	> 110 @10	NA	NA	*(31)*
Co_3O_4	340	30 @10	NA	NA	*(31)*
$Mn_{7.5}O_{10}Br_3$	295	500 @10	300 h @0.1 $A \cdot cm^{-2}$, 25°C	NA	*(23)*
LMCF	353	360 @10	2 $A \cdot cm^{-2}$ @2.2 $V_{iR\text{-}corr.}$, 110 h @0.21 $A \cdot cm^{-2}$, 80 °C	~ 10^7	*(25)*
Co_3O_4/FTO	570	50 @1	NA	NA	*(29)*
Co_3O_4@C/GPO	356	43 @10	NA	25	*(63)*
CoHFe on Sb-SnO_2	820 @0.9	NA	6 $mA \cdot cm^{-2}$ @1.8 V, 21 h @50 $mA \cdot cm^{-2}$, 80°C	NA	*(34)*

Catalyst	η @ 10 mA cm^{-2} (mV)	Stability @ j ($mA \cdot cm^{-2}$) in H-cell (h)	PEMWE performance	S-number	Ref.
Ag-Co_3O_4	470	10 @10	NA	NA	*(64)*
Co_2MnO_4/FTO		1500 @200	NA	NA	*(59)*
$Ni_{0.5}Mn_{0.5}Sb_{1.5}O_y$	672	168 @10	NA	~ 6194	*(27)*
MnO_2	510	8000 @10	12 h @0.1 $A \cdot cm^{-2}$ at 25°C	NA	*(26)*
Ba[Co-POM]	361	0.3 @10	NA	NA	*(65)*
CoMoNiS-NF	228	1.3 @20	NA	NA	*(66)*
NiFeP	540	30 @10	NA	NA	*(67)*
CoFePb	620	160 @10	NA	NA	*(32)*
M 94% (modified γ-MnO_2)		> 3500 @200	1 $A \cdot cm^{-2}$ @2.0 V (Nafion 115), 1000 h @0.2 $A \cdot cm^{-2}$, 80°C	NA	*(40)*

References and Notes

1. S. Chu, A. Majumdar, Opportunities and challenges for a sustainable energy future. *Nature* **488**, 294–303 (2012). doi:10.1038/nature11475 Medline

2. I. Staffell, D. Scamman, A. Velazquez Abad, P. Balcombe, P. E. Dodds, P. Ekins, N. Shah, K. R. Ward, The role of hydrogen and fuel cells in the global energy system. *Energy Environ. Sci.* **12**, 463–491 (2019). doi:10.1039/C8EE01157E

3. Z. W. Seh, J. Kibsgaard, C. F. Dickens, I. Chorkendorff, J. K. Nørskov, T. F. Jaramillo, Combining theory and experiment in electrocatalysis: Insights into materials design. *Science* **355**, eaad4998 (2017). doi:10.1126/science.aad4998 Medline

4. M. Carmo, D. L. Fritz, J. Mergel, D. Stolten, A comprehensive review on PEM water electrolysis. *Int. J. Hydrogen Energy* **38**, 4901–4934 (2013). doi:10.1016/j.ijhydene.2013.01.151

5. C. Spöri, J. T. H. Kwan, A. Bonakdarpour, D. P. Wilkinson, P. Strasser, The Stability Challenges of Oxygen Evolving Catalysts: Towards a Common Fundamental Understanding and Mitigation of Catalyst Degradation. *Angew. Chem. Int. Ed.* **56**, 5994–6021 (2017). doi:10.1002/anie.201608601 Medline

6. L. An, C. Wei, M. Lu, H. Liu, Y. Chen, G. G. Scherer, A. C. Fisher, P. Xi, Z. J. Xu, C.-H. Yan, Recent Development of Oxygen Evolution Electrocatalysts in Acidic Environment. *Adv. Mater.* **33**, e2006328 (2021). doi:10.1002/adma.202006328 Medline

7. P. C. K. Vesborg, T. F. Jaramillo, Addressing the terawatt challenge: Scalability in the supply of chemical elements for renewable energy. *RSC Adv.* **2**, 7933–7947 (2012). doi:10.1039/c2ra20839c

8. L. Yang, G. Yu, X. Ai, W. Yan, H. Duan, W. Chen, X. Li, T. Wang, C. Zhang, X. Huang, J.-S. Chen, X. Zou, Efficient oxygen evolution electrocatalysis in acid by a perovskite with face-sharing IrO_6 octahedral dimers. *Nat. Commun.* **9**, 5236 (2018). doi:10.1038/s41467-018-07678-w Medline

9. Y. Pi, Q. Shao, P. Wang, J. Guo, X. Huang, General Formation of Monodisperse IrM (M = Ni, Co, Fe) Bimetallic Nanoclusters as Bifunctional Electrocatalysts for Acidic Overall Water Splitting. *Adv. Funct. Mater.* **27**, 1700886 (2017). doi:10.1002/adfm.201700886

10. S. Cherevko, A. R. Zeradjanin, A. A. Topalov, N. Kulyk, I. Katsounaros, K. J. J. Mayrhofer, Dissolution of Noble Metals during Oxygen Evolution in Acidic Media. *ChemCatChem* **6**, 2219–2223 (2014). doi:10.1002/cctc.201402194

11. E. A. Paoli, F. Masini, R. Frydendal, D. Deiana, C. Schlaup, M. Malizia, T. W. Hansen, S. Horch, I. E. L. Stephens, I. Chorkendorff, Oxygen evolution on well-characterized mass-selected Ru and RuO_2 nanoparticles. *Chem. Sci.* **6**, 190–196 (2015). doi:10.1039/C4SC02685C Medline

12. A. Grimaud, O. Diaz-Morales, B. Han, W. T. Hong, Y.-L. Lee, L. Giordano, K. A. Stoerzinger, M. T. M. Koper, Y. Shao-Horn, Activating lattice oxygen redox reactions in metal oxides to catalyse oxygen evolution. *Nat. Chem.* **9**, 457–465 (2017). doi:10.1038/nchem.2695 Medline

13. Z.-Y. Wu, F.-Y. Chen, B. Li, S.-W. Yu, Y. Z. Finfrock, D. M. Meira, Q.-Q. Yan, P. Zhu, M.-X. Chen, T.-W. Song, Z. Yin, H.-W. Liang, S. Zhang, G. Wang, H. Wang, Non-iridium-based electrocatalyst for durable acidic oxygen evolution reaction in proton

exchange membrane water electrolysis. *Nat. Mater.* **22**, 100–108 (2023). doi:10.1038/s41563-022-01380-5 Medline

14. L. C. Seitz, C. F. Dickens, K. Nishio, Y. Hikita, J. Montoya, A. Doyle, C. Kirk, A. Vojvodic, H. Y. Hwang, J. K. Norskov, T. F. Jaramillo, A highly active and stable IrOx/$SrIrO_3$ catalyst for the oxygen evolution reaction. *Science* **353**, 1011–1014 (2016). doi:10.1126/science.aaf5050 Medline

15. S. Hao, H. Sheng, M. Liu, J. Huang, G. Zheng, F. Zhang, X. Liu, Z. Su, J. Hu, Y. Qian, L. Zhou, Y. He, B. Song, L. Lei, X. Zhang, S. Jin, Torsion strained iridium oxide for efficient acidic water oxidation in proton exchange membrane electrolyzers. *Nat. Nanotechnol.* **16**, 1371–1377 (2021). doi:10.1038/s41565-021-00986-1 Medline

16. Y. Wang, S. Hao, X. Liu, Q. Wang, Z. Su, L. Lei, X. Zhang, Ce-Doped IrO_2 Electrocatalysts with Enhanced Performance for Water Oxidation in Acidic Media. *ACS Appl. Mater. Interfaces* **12**, 37006–37012 (2020). doi:10.1021/acsami.0c00389 Medline

17. H. Liu, Z. Zhang, J. Fang, M. Li, M. G. Sendeku, X. Wang, H. Wu, Y. Li, J. Ge, Z. Zhuang, D. Zhou, Y. Kuang, X. Sun, Eliminating over-oxidation of ruthenium oxides by niobium for highly stable electrocatalytic oxygen evolution in acidic media. *Joule* **7**, 558–573 (2023). doi:10.1016/j.joule.2023.02.012

18. M. W. Kanan, D. G. Nocera, In situ formation of an oxygen-evolving catalyst in neutral water containing phosphate and Co^{2+}. *Science* **321**, 1072–1075 (2008). doi:10.1126/science.1162018 Medline

19. J. B. Gerken, J. G. McAlpin, J. Y. C. Chen, M. L. Rigsby, W. H. Casey, R. D. Britt, S. S. Stahl, Electrochemical water oxidation with cobalt-based electrocatalysts from pH 0–14: The thermodynamic basis for catalyst structure, stability, and activity. *J. Am. Chem. Soc.* **133**, 14431–14442 (2011). doi:10.1021/ja205647m Medline

20. Z.-F. Huang, J. Song, Y. Du, S. Xi, S. Dou, J. M. V. Nsanzimana, C. Wang, Z. J. Xu, X. Wang, Chemical and structural origin of lattice oxygen oxidation in Co–Zn oxyhydroxide oxygen evolution electrocatalysts. *Nat. Energy* **4**, 329–338 (2019). doi:10.1038/s41560-019-0355-9

21. B. Zhang, L. Wang, Z. Cao, S. M. Kozlov, F. P. García de Arquer, C. T. Dinh, J. Li, Z. Wang, X. Zheng, L. Zhang, Y. Wen, O. Voznyy, R. Comin, P. De Luna, T. Regier, W. Bi, E. E. Alp, C.-W. Pao, L. Zheng, Y. Hu, Y. Ji, Y. Li, Y. Zhang, L. Cavallo, H. Peng, E. H. Sargent, High-valence metals improve oxygen evolution reaction performance by modulating 3*d* metal oxidation cycle energetics. *Nat. Catal.* **3**, 985–992 (2020). doi:10.1038/s41929-020-00525-6

22. B. Zhang, X. Zheng, O. Voznyy, R. Comin, M. Bajdich, M. García-Melchor, L. Han, J. Xu, M. Liu, L. Zheng, F. P. García de Arquer, C. T. Dinh, F. Fan, M. Yuan, E. Yassitepe, N. Chen, T. Regier, P. Liu, Y. Li, P. De Luna, A. Janmohamed, H. L. Xin, H. Yang, A. Vojvodic, E. H. Sargent, Homogeneously dispersed multimetal oxygen-evolving catalysts. *Science* **352**, 333–337 (2016). doi:10.1126/science.aaf1525 Medline

23. S. Pan, H. Li, D. Liu, R. Huang, X. Pan, D. Ren, J. Li, M. Shakouri, Q. Zhang, M. Wang, C. Wei, L. Mai, B. Zhang, Y. Zhao, Z. Wang, M. Graetzel, X. Zhang, Efficient and stable noble-metal-free catalyst for acidic water oxidation. *Nat. Commun.* **13**, 2294 (2022). doi:10.1038/s41467-022-30064-6 Medline

24. J. Huang, H. Sheng, R. D. Ross, J. Han, X. Wang, B. Song, S. Jin, Modifying redox properties and local bonding of Co_3O_4 by CeO_2 enhances oxygen evolution catalysis in acid. *Nat. Commun.* **12**, 3036 (2021). doi:10.1038/s41467-021-23390-8 Medline

25. L. Chong, G. Gao, J. Wen, H. Li, H. Xu, Z. Green, J. D. Sugar, A. J. Kropf, W. Xu, X.-M. Lin, H. Xu, L.-W. Wang, D.-J. Liu, La- and Mn-doped cobalt spinel oxygen evolution catalyst for proton exchange membrane electrolysis. *Science* **380**, 609–616 (2023). doi:10.1126/science.ade1499 Medline

26. A. Li, H. Ooka, N. Bonnet, T. Hayashi, Y. Sun, Q. Jiang, C. Li, H. Han, R. Nakamura, Stable Potential Windows for Long-Term Electrocatalysis by Manganese Oxides Under Acidic Conditions. *Angew. Chem. Int. Ed.* **58**, 5054–5058 (2019). doi:10.1002/anie.201813361 Medline

27. I. A. Moreno-Hernandez, C. A. MacFarland, C. G. Read, K. M. Papadantonakis, B. S. Brunschwig, N. S. Lewis, Crystalline nickel manganese antimonate as a stable water-oxidation catalyst in aqueous 1.0 M H_2SO_4. *Energy Environ. Sci.* **10**, 2103–2108 (2017). doi:10.1039/C7EE01486D

28. I. C. Man, H.-Y. Su, F. Calle-Vallejo, H. A. Hansen, J. I. Martínez, N. G. Inoglu, J. Kitchin, T. F. Jaramillo, J. K. Nørskov, J. Rossmeisl, Universality in Oxygen Evolution Electrocatalysis on Oxide Surfaces. *ChemCatChem* **3**, 1159–1165 (2011). doi:10.1002/cctc.201000397

29. J. S. Mondschein, J. F. Callejas, C. G. Read, J. Y. C. Chen, C. F. Holder, C. K. Badding, R. E. Schaak, Crystalline Cobalt Oxide Films for Sustained Electrocatalytic Oxygen Evolution under Strongly Acidic Conditions. *Chem. Mater.* **29**, 950–957 (2017). doi:10.1021/acs.chemmater.6b02879

30. M. Etzi Coller Pascuzzi, M. van Velzen, J. P. Hofmann, E. J. M. Hensen, On the Stability of Co_3O_4 Oxygen Evolution Electrocatalysts in Acid. *ChemCatChem* **13**, 459–467 (2021). doi:10.1002/cctc.202001428

31. N. Wang, P. Ou, R. K. Miao, Y. Chang, Z. Wang, S.-F. Hung, J. Abed, A. Ozden, H.-Y. Chen, H.-L. Wu, J. E. Huang, D. Zhou, W. Ni, L. Fan, Y. Yan, T. Peng, D. Sinton, Y. Liu, H. Liang, E. H. Sargent, Doping Shortens the Metal/Metal Distance and Promotes OH Coverage in Non-Noble Acidic Oxygen Evolution Reaction Catalysts. *J. Am. Chem. Soc.* **145**, 7829–7836 (2023). doi:10.1021/jacs.2c12431 Medline

32. M. Chatti, J. L. Gardiner, M. Fournier, B. Johannessen, T. Williams, T. R. Gengenbach, N. Pai, C. Nguyen, D. R. MacFarlane, R. K. Hocking, A. N. Simonov, Intrinsically stable in situ generated electrocatalyst for long-term oxidation of acidic water at up to 80 °C. *Nat. Catal.* **2**, 457–465 (2019). doi:10.1038/s41929-019-0277-8

33. P.-Y. Cheng, Y.-C. Ting, C.-C. Cheng, D. Senthil Raja, S.-H. Lin, Y.-X. Yeh, J.-T. Su, S.-Y. Lu, Nitrogen-doped carbon armored Cobalt oxide hollow nanocubes electrochemically anchored on fluorine-doped tin oxide substrate for acidic oxygen evolution reaction. *J. Colloid Interface Sci.* **623**, 327–336 (2022). doi:10.1016/j.jcis.2022.05.036 Medline

34. B. Rodríguez-García, Á. Reyes-Carmona, I. Jiménez-Morales, M. Blasco-Ahicart, S. Cavaliere, M. Dupont, D. Jones, J. Rozière, J. R. Galán-Mascarós, F. Jaouen, Cobalt hexacyanoferrate supported on Sb-doped SnO_2 as a non-noble catalyst for oxygen evolution in acidic medium. *Sustain. Energy Fuels* **2**, 589–597 (2018). doi:10.1039/C7SE00512A

35. Y. Wen, C. Liu, R. Huang, H. Zhang, X. Li, F. P. García de Arquer, Z. Liu, Y. Li, B. Zhang, Introducing Brønsted acid sites to accelerate the bridging-oxygen-assisted deprotonation in acidic water oxidation. *Nat. Commun.* **13**, 4871 (2022). doi:10.1038/s41467-022-32581-w Medline

36. J. Rossmeisl, Z.-W. Qu, H. Zhu, G.-J. Kroes, J. K. Nørskov, Electrolysis of water on oxide surfaces. *J. Electroanal. Chem.* **607**, 83–89 (2007). doi:10.1016/j.jelechem.2006.11.008

37. Y. Ping, R. J. Nielsen, W. A. I. I. I. Goddard 3rd, The Reaction Mechanism with Free Energy Barriers at Constant Potentials for the Oxygen Evolution Reaction at the IrO_2 (110) Surface. *J. Am. Chem. Soc.* **139**, 149–155 (2017). doi:10.1021/jacs.6b07557 Medline

38. L. F. Shen, B. A. Lu, Y. Y. Li, J. Liu, Z. C. Huang-Fu, H. Peng, J. Y. Ye, X. M. Qu, J. M. Zhang, G. Li, W. B. Cai, Y. X. Jiang, S. G. Sun, Interfacial Structure of Water as a New Descriptor of the Hydrogen Evolution Reaction. *Angew. Chem. Int. Ed.* **59**, 22397–22402 (2020). doi:10.1002/anie.202007567 Medline

39. Y.-H. Wang, S. Zheng, W.-M. Yang, R.-Y. Zhou, Q.-F. He, P. Radjenovic, J.-C. Dong, S. Li, J. Zheng, Z.-L. Yang, G. Attard, F. Pan, Z.-Q. Tian, J.-F. Li, In situ Raman spectroscopy reveals the structure and dissociation of interfacial water. *Nature* **600**, 81–85 (2021). doi:10.1038/s41586-021-04068-z Medline

40. S. Kong, A. Li, J. Long, K. Adachi, D. Hashizume, Q. Jiang, K. Fushimi, H. Ooka, J. Xiao, R. Nakamura, Acid-stable manganese oxides for proton exchange membrane water electrolysis. *Nat. Catal.* **7**, 252–261 (2024). doi:10.1038/s41929-023-01091-3

41. L. Gao, C. Li, W. Huang, S. Mei, H. Lin, Q. Ou, Y. Zhang, J. Guo, F. Zhang, S. Xu, H. Zhang, Mxene/Polymer Membranes: Synthesis, Properties, and Emerging Applications. *Chem. Mater.* **32**, 1703–1747 (2020). doi:10.1021/acs.chemmater.9b04408

42. S. E. Kelch, R. E. Youngman, E. Ferrage, J. J. Basinski, J. Wang, L. Aristilde, Quantitative Spectroscopic Analysis of Water Populations in the Hydrated Nanopore Environments of a Natural Montmorillonite. *J. Phys. Chem. C* **125**, 26552–26565 (2021). doi:10.1021/acs.jpcc.1c05462

43. K. Oka, T. Shibue, N. Sugimura, Y. Watabe, B. Winther-Jensen, H. Nishide, Long-lived water clusters in hydrophobic solvents investigated by standard NMR techniques. *Sci. Rep.* **9**, 223 (2019). doi:10.1038/s41598-018-36787-1 Medline

44. Q. Hu, H. Zhao, S. Ouyang, Understanding water structure from Raman spectra of isotopic substitution H_2O/D_2O up to 573 K. *Phys. Chem. Chem. Phys.* **19**, 21540–21547 (2017). doi:10.1039/C7CP02065A Medline

45. C.-Q. Li, S.-S. Yi, D. Chen, Y. Liu, Y.-J. Li, S.-Y. Lu, X.-Z. Yue, Z.-Y. Liu, Oxygen vacancy engineered $SrTiO_3$ nanofibers for enhanced photocatalytic H_2 production. *J. Mater. Chem. A* **7**, 17974–17980 (2019). doi:10.1039/C9TA03701B

46. A. Moysiadou, S. Lee, C.-S. Hsu, H. M. Chen, X. Hu, Mechanism of Oxygen Evolution Catalyzed by Cobalt Oxyhydroxide: Cobalt Superoxide Species as a Key Intermediate and Dioxygen Release as a Rate-Determining Step. *J. Am. Chem. Soc.* **142**, 11901–11914 (2020). doi:10.1021/jacs.0c04867 Medline

47. C. Jing, T. Yuan, L. Li, J. Li, Z. Qian, J. Zhou, Y. Wang, S. Xi, N. Zhang, H.-J. Lin, C.-T. Chen, Z. Hu, D.-W. Li, L. Zhang, J.-Q. Wang, Electrocatalyst with Dynamic

Formation of the Dual-Active Site from the Dual Pathway Observed by *In Situ* Raman Spectroscopy. *ACS Catal.* **12**, 10276–10284 (2022). doi:10.1021/acscatal.2c01038

48. M. Zhang, M. de Respinis, H. Frei, Time-resolved observations of water oxidation intermediates on a cobalt oxide nanoparticle catalyst. *Nat. Chem.* **6**, 362–367 (2014). doi:10.1038/nchem.1874 Medline

49. H. Liu, C. Li, D. Chen, P. Cui, F. Ye, J. Yang, Uniformly dispersed platinum-cobalt alloy nanoparticles with stable compositions on carbon substrates for methanol oxidation reaction. *Sci. Rep.* **7**, 11421 (2017). doi:10.1038/s41598-017-10223-2 Medline

50. S. Geiger, O. Kasian, M. Ledendecker, E. Pizzutilo, A. M. Mingers, W. T. Fu, O. Diaz-Morales, Z. Li, T. Oellers, L. Fruchter, A. Ludwig, K. J. J. Mayrhofer, M. T. M. Koper, S. Cherevko, The stability number as a metric for electrocatalyst stability benchmarking. *Nat. Catal.* **1**, 508–515 (2018). doi:10.1038/s41929-018-0085-6

51. C. Wei, Z. Wang, K. Otani, D. Hochfilzer, K. Zhang, R. Nielsen, I. Chorkendorff, J. Kibsgaard, Benchmarking Electrocatalyst Stability for Acidic Oxygen Evolution Reaction: The Crucial Role of Dissolved Ion Concentration. *ACS Catal.* **13**, 14058–14069 (2023). doi:10.1021/acscatal.3c03257

52. M. Milosevic, T. Böhm, A. Körner, M. Bierling, L. Winkelmann, K. Ehelebe, A. Hutzler, M. Suermann, S. Thiele, S. Cherevko, In Search of Lost Iridium: Quantification of Anode Catalyst Layer Dissolution in Proton Exchange Membrane Water Electrolyzers. *ACS Energy Lett.* **8**, 2682–2688 (2023). doi:10.1021/acsenergylett.3c00193

53. H. Benzidi, Co-del_OER, ioChem-BD (2024); https://doi.org/10.19061/iochem-bd-1-320.

54. R. Ram, F. P. García de Arquer, STEM and XRD files of Water and Hydroxide Trapping in Cobalt Tungstate for Proton Exchange Membrane Water Electrolysis, Data set, Zenodo (2024); https://doi.org/10.5281/zenodo.11161891.

55. G. Kresse, J. Hafner, *Ab initio* molecular dynamics for open-shell transition metals. *Phys. Rev. B* **48**, 13115–13118 (1993). doi:10.1103/PhysRevB.48.13115 Medline

56. A. Togo, L. Chaput, T. Tadano, I. Tanaka, Implementation strategies in phonopy and phono3py. *J. Phys. Condens. Matter* **35**, 353001 (2023). doi:10.1088/1361-648X/acd831 Medline

57. M. Garcia-Ratés, N. López, Multigrid-Based Methodology for Implicit Solvation Models in Periodic DFT. *J. Chem. Theory Comput.* **12**, 1331–1341 (2016). doi:10.1021/acs.jctc.5b00949 Medline

58. J. K. Nørskov, J. Rossmeisl, A. Logadottir, L. Lindqvist, J. R. Kitchin, T. Bligaard, H. Jónsson, Origin of the Overpotential for Oxygen Reduction at a Fuel-Cell Cathode. *J. Phys. Chem. B* **108**, 17886–17892 (2004). doi:10.1021/jp047349j

59. A. Li, S. Kong, C. Guo, H. Ooka, K. Adachi, D. Hashizume, Q. Jiang, H. Han, J. Xiao, R. Nakamura, Enhancing the stability of cobalt spinel oxide towards sustainable oxygen evolution in acid. *Nat. Catal.* **5**, 109–118 (2022). doi:10.1038/s41929-021-00732-9

60. Q. Yin, J. M. Tan, C. Besson, Y. V. Geletii, D. G. Musaev, A. E. Kuznetsov, Z. Luo, K. I. Hardcastle, C. L. Hill, A fast soluble carbon-free molecular water oxidation catalyst based on abundant metals. *Science* **328**, 342–345 (2010). doi:10.1126/science.1185372 Medline

61. Z. Kang, T. Schuler, Y. Chen, M. Wang, F.-Y. Zhang, G. Bender, Effects of interfacial contact under different operating conditions in proton exchange membrane water

electrolysis. *Electrochim. Acta* **429**, 140942 (2022). doi:10.1016/j.electacta.2022.140942

62. M. J. Burch, K. A. Lewinski, M. I. Buckett, S. Luopa, F. Sun, E. J. Olson, A. J. Steinbach, A novel work-flow to study Ir electrode thinning and dissolution in proton exchange membrane water electrolyzers. *J. Power Sources* **500**, 229978 (2021). doi:10.1016/j.jpowsour.2021.229978

63. J. Yu, F. A. Garcés-Pineda, J. González-Cobos, M. Peña-Díaz, C. Rogero, S. Giménez, M. C. Spadaro, J. Arbiol, S. Barja, J. R. Galán-Mascarós, Sustainable oxygen evolution electrocatalysis in aqueous 1 M H_2SO_4 with earth abundant nanostructured Co_3O_4. *Nat. Commun.* **13**, 4341 (2022). doi:10.1038/s41467-022-32024-6 Medline

64. K.-L. Yan, J.-F. Qin, J.-H. Lin, B. Dong, J.-Q. Chi, Z.-Z. Liu, F.-N. Dai, Y.-M. Chai, C.-G. Liu, Probing the active sites of Co_3O_4 for the acidic oxygen evolution reaction by modulating the Co^{2+}/Co^{3+} ratio. *J. Mater. Chem. A* **6**, 5678–5686 (2018). doi:10.1039/C8TA00070K

65. M. Blasco-Ahicart, J. Soriano-López, J. J. Carbó, J. M. Poblet, J. R. Galan-Mascaros, Polyoxometalate electrocatalysts based on earth-abundant metals for efficient water oxidation in acidic media. *Nat. Chem.* **10**, 24–30 (2018). doi:10.1038/nchem.2874 Medline

66. Y. Yang, H. Yao, Z. Yu, S. M. Islam, H. He, M. Yuan, Y. Yue, K. Xu, W. Hao, G. Sun, H. Li, S. Ma, P. Zapol, M. G. Kanatzidis, Hierarchical Nanoassembly of $MoS_2/Co_9S_8/Ni_3S_2$/Ni as a Highly Efficient Electrocatalyst for Overall Water Splitting in a Wide pH Range. *J. Am. Chem. Soc.* **141**, 10417–10430 (2019). doi:10.1021/jacs.9b04492 Medline

67. F. Hu, S. Zhu, S. Chen, Y. Li, L. Ma, T. Wu, Y. Zhang, C. Wang, C. Liu, X. Yang, L. Song, X. Yang, Y. Xiong, Amorphous Metallic NiFeP: A Conductive Bulk Material Achieving High Activity for Oxygen Evolution Reaction in Both Alkaline and Acidic Media. *Adv. Mater.* **29**, 1606570 (2017). doi:10.1002/adma.201606570 Medline